

Mass Streaming via Acoustic Radiation Pressure Combined with a Venturi

by

Osman ULUOCAK, EIT
B.Eng. Univeristy of Victoria, 2015

A Thesis Submitted in Partial Fulfillment of the
Requirements for the Degree of

MASTER OF APPLIED SCIENCE

in the Department of Mechanical Engineering

© Osman ULUOCAK, 2020
University of Victoria

All rights reserved. This thesis may not be reproduced in whole or in part, by
photocopying or other means, without the permission of the author.

Mass Streaming via Acoustic Radiation Pressure Combined with a Venturi

by

Osman ULUOCAK, EIT
B.Eng. Univeristy of Victoria, 2015

Supervisory Committee

Dr. Andrew Rowe, Supervisor(Department of Mechanical Engineer)

Dr. Peter Oshkai, Departmental Member(Department of Mechanical Engineer)

Dr. Aaron Gulliver, Departmental Member(Department of Electrical & Computer Engineering)

ABSTRACT

Thermoacoustic (TA) engines and generators are one of the latest derivations of the two century-old energy conversion devices that are based on the Stirling cycle. Unlike the traditional Stirling devices, the TA devices use the pressure wavefront of a standing wave created in the working gas, eliminating the power and displacement pistons. The lack of moving parts and the lubrication make these devices practically maintenance-free, making them ideal candidates for space and marine applications. The traditional method for delivering thermal energy to the working fluid (standing wave) would require a heat exchanger, absorbing energy from an external source, and a pump to deliver this energy to the working fluid, however, these components inherently have high losses as well as high cost, hindering overall efficiency. In thermoacoustic systems, the oscillating nature of the working fluid makes it possible to eliminate these components, with most widely applied method being the placement of an asymmetrical gas-diode in a heat carrying loop which is attached to the resonator. Such methods of creating a time-averaged nonzero flow-rate in a preferred direction is called Acoustic Mass Streaming. An alternative to the gas-diode technique to create such pump-less flows is to take advantage of the Acoustic Radiation Pressure (ARP) phenomenon, which is a time-averaged spatially varying pressure of second order amplitude, observed in standing wave resonators. Connecting a loop in two different locations to the resonator creates a pressure differential due to the spatial variance which can be further amplified with a converging-diverging nozzle, namely a Venturi. This thesis investigates the fundamentals of this novel acoustic mass streaming method, where the Acoustic Radiation Pressure is combined with a Venturi for increased efficiency. Using the thermoacoustic software DELTAEC, the effects of placing a Venturi with different dimensional parameters into the resonator is studied and the changes on the ARP is examined. Considering various types of acoustic losses, the maximum amount of fluid that can be circulated in the pump-less loop is investigated. Time-averaged minor-loss coefficients for converging and diverging acoustic flows at a T-Junction are also presented.

Contents

Supervisory Committee	ii
Abstract	iii
Table of Contents	iv
List of Figures	vi
List of Tables	xi
List of Symbols	xii
1 Introduction	1
1.1 Background	1
1.1.1 History of Thermoacoustics	1
1.1.2 Thermoacoustic Engines and Refrigerators	4
1.1.3 Mathematical Models and Available Simulation Tools	7
1.2 Research Problem	8
1.3 Objectives	10
1.4 Structure	11
2 Acoustic Radiation Pressure	12
2.1 Background	12
2.2 Acoustic Variables and Complex Notation	13
2.3 Second Order Pressure in 1-D Inviscid Flows	15
2.4 Second-Order Time-Averaged Pressure	17
2.5 ARP with Non-zero Mean Temperature Gradient	18
3 Acoustic Mass Streaming with Acoustic Radiation Pressure and a Venturi	21

3.1	Acoustic Mass Streaming	21
3.2	Mass Streaming via Acoustic Radiation Pressure Differential	25
3.3	Effects of a Venturi on the Acoustic Radiation Pressure	26
4	Minor Losses for a Venturi-SCL Assembly	30
4.1	Minor Losses in Oscillating Flows	31
4.2	Converging and Diverging T-Junction Flow Minor Losses	34
5	DeltaEC Simulations	40
5.1	ARP in a Resonator with Varying Venturi Geometry	41
5.2	Time-Averaged Converging and Diverging T-Junction Flow Minor Losses	47
5.3	SCL - Nonzero Mean Flow Simulations	51
6	Discussion	57
6.1	Uncertainties in Simulation Results	57
6.2	Discussion of Results	61
7	Conclusion and Recommendations	63
7.1	Future Work and Improvements	65
A	Second-Order Time-Averaged Pressure	67
B	Irreversibilities in Acoustic Flows	72
B.1	Viscous Resistance Losses	72
B.2	Thermal Relaxation Losses	76
B.3	Turbulence and Iguchi's Quasi-Steady State Assumption	79
C	Time-Averaged Minos Loss Coefficient for Converging-Diverging Pipe Flow	85
D	DELTAEC Codes	87
	Bibliography	90

List of Figures

Figure 1.1	A glass tube with air trapped inside heated at one end [4]. . . .	2
Figure 1.2	a) Higgins' Singing Flame fed by a continuous flow of hydrogen as fuel. b) Rijke Tube using a heated wire mesh to deliver heat to air c) Soundhauss Tube.	3
Figure 1.3	Two possible functions of a thermoacoustic device based on the relative temperatures of the stack's ends and the oscillating gas parcel, working as a refrigerator in one instance and as a heat pump in the other. (a) Compressed gas parcel delivering heat to the hot side of the stack. (b) Expanded gas parcel is moved to the cold side of the stack where it is cooler than the portion of the stack it interacts with, absorbing heat. (c) Gas parcel absorbing heat from the warmer stack surface. (d) Expanded gas parcel dumps heat to the cold end of the stack [4].	5
Figure 1.4	Thermoacoustic Stirling engine designed at Los Alamos National Laboratory [4].	6
Figure 1.5	Schematic of waste heat recovery system with the Venturi placed at the pressure node delivering heat to the hot side of the regenerator (Thermal Module) where the pressure oscillation is amplified [12]	9
Figure 2.1	Flow profile in a viscous internal flow as a function of distance (y) from the wall shown as the parabolic curve in black. Volumetric flow rate divided by the cross-sectional area gives the average velocity in the channel used in the boundary-layer approximation, shown in red.	13
Figure 2.2	Time-averaged nonzero (green) and oscillating (red) flows in the SCL created by the pressure differential of $p_{2,0}$ and the Venturi.	20

Figure 3.1 Reid's Refrigerator - Steady flow injected at the upper pressure node at ambient temperature and flowed out at the lower pressure node at a colder temperature [20].	22
Figure 3.2 Gedeon Streaming caused by flow path asymmetries [14].	22
Figure 3.3 (a) Scale drawing of the Thermoacoustic engine. (b) Scale drawing of the torus section [8].	23
Figure 3.4 Diagram of the jet pump. The two flow patterns represent the first-order acoustic velocities during the two halves of the acoustic cycle. Subscripts s and b refer to the small and big openings respectively [8].	23
Figure 3.5 A portion of a Thermoacoustic machine where the heat exchanger is replaced by a pipe one wavelength long. Gas diodes at the velocity antinodes induce mean flow [24].	24
Figure 3.6 Use of a gas diode to create a self-circulating loop [19, pp.109].	25
Figure 3.7 (a) Measured distribution of $p_1(x)$ for 9 different amplitudes in a resonator (slightly longer than a half-wavelength) shown as symbols, the lines are drawn using Equation 2.5 with a P adjusted to fit the data [15]. (b) Symbols represent measured $p_{2,0}$, lines are drawn using Equation 3.4 with P used in (a) with $constant'=0$ [15].	27
Figure 3.8 (a) Schematic of $\Delta p_{2,0}$ between two locations along the resonator. (b) Increased $\Delta p_{2,0}$ with a Venturi, in a lossless scenario.	29
Figure 4.1 Vortices created in a 90°elbow, causing minor losses [26].	31
Figure 4.2 Vortices caused by sudden expansion in a flow path [26].	31
Figure 4.3 Oscillating and steady flows in the Venturi SCL represented with red and green arrows respectively. The SCL loop might include features such as compliance volumes or inertance tubes to adjust the phase of the acoustic flow in the SCL. This figure depicts a simplified loop.	33
Figure 4.4 a) Flow in a converging T-Junction. b) Flow in a diverging T-Junction. c) and d) Locations of pressure readings for respective minor loss coefficients. The labeled K variables represent the pressure differential, Δp , between the points they indicate.	35

Figure 4.5 (a) K_B values for a converging T-Junction flow. Curves represent branch to trunk area ratios. The horizontal axis is the branch to trunk volumetric flow ratio. (b) Solid lines represent the K_B values for a diverging T-Junction flow with various area ratios. The dashed curve represents the trunk loss coefficient, K_T , for the diverging flow case. The horizontal axis for K_T is the ratio of trunk inlet to trunk outlet volumetric flow rates. Adapted from [26].	36
Figure 5.1 DeltaEC diagram of a half-wavelength resonator with a Venturi at the pressure node.	41
Figure 5.2 A_c , $E_{2,0}$, $ U_1 $, $ p_1 $ values for a 1 meter-long half-wavelength resonator with varying Venturi sizes and constant piston displacement amplitude.	42
Figure 5.3 Comparison of average flow velocity, $ u_1 $, profiles with varying Venturi sizes (DeltaEC simulated vs. Lossless Equation 3.5). . .	43
Figure 5.4 $ u_1 $ comparison of DeltaEC simulations and Equation 3.5. . . .	44
Figure 5.5 Comparison of $p_{2,0}$ values obtained from DeltaEC and Equation 3.7 for varying Venturi sizes.	45
Figure 5.6 $p_{2,0}$ comparison of DeltaEC simulations and Equation 3.7. . . .	46
Figure 5.7 Acoustic power loss experienced at the piston face with varying Venturi sizes.	46
Figure 5.8 Schematic of Venturi-SCL simulation used for obtaining effective K values at a T-Junction.	47
Figure 5.9 Simulated instantaneous branch and trunk flow rates at the T-Junction located at the pressure node with a Venturi area ratio of 0.7.	48
Figure 5.10 Instantaneous and time-averaged K_B at T-Junction #1 with 0.7 area ratio using the volumetric flow rates from Figure 5.9 and Equations 4.9 and 4.14 with respective branch flow direction. . .	49
Figure 5.11 Instantaneous and time-averaged K_T at T-Junction #1 with 0.7 area ratio using the volumetric flow rates from Figure 5.9 and Equations 4.13 and 4.16 with respective branch flow direction. . .	50
Figure 5.12 DeltaEC diagram of a half-wavelength Venturi-SCL resonator. . .	51

Figure 5.13 Comparison of pressure and volumetric flow rate amplitudes distributions for Venturi-SCL and a straight resonator.	52
Figure 5.14 Time-averaged minor loss coefficients for 2 T-Junctions.	53
Figure 5.15 Steady and alternating flow rate amplitudes with varying Venturi sizes.	54
Figure 5.16 Acoustic power experienced at the piston face with varying Venturi sizes.	55
Figure 6.1 Volumetric flow rate phase angles between T-Junction #1 and T-Junction #2.	59
Figure A.1 Close-fitted Cylinder in Equilibrium	67
Figure A.2 Volumetric Asymmetry in a Close-Fitted Piston Assembly. a) Piston at rest at x_0 with p_m inside the cylinder is equal to the ambient pressure. b) Piston at bottom dead center at $t = \pi/4$. Red dotted line showing the average volume of the gas while the volume is less than V_o . c) Piston at top dead center, red dotted line showing the average volume experienced by the gas for times when the gas is expanded over V_o	70
Figure B.1 (a) Depiction of the oscillating flow direction in a very large channel (b) The real and imaginary components of the particle displacements [14].	74
Figure B.2 $F = 1 - f_v$ values for various geometries. The x-axis λ is a dimensionless variable indicating the distance measured from the solid surface [29].	75
Figure B.3 Friction factor f_M as a function of Re and $\frac{\epsilon}{d}$. Adapted from [31].	80
Figure B.4 Comparison of Rott's approximation for laminar flows and the experimental results for high power, thermoacoustic applications. The lines represent DELTAEC simulations for laminar flow. Circles represent experimental measurements [14].	81
Figure B.5 Regimes of oscillating flow for pipe roughness ratio of $\epsilon = 0$ as a function of peak Reynolds number, $ Re_1 $. Adapted from [14]. .	82
Figure C.1 Frequency dependence of the time averaged abrupt area change minor loss coefficient [28].	85

Figure C.2 Time-averaged minor loss coefficient for tapered area change in an oscillating pipe flow [28].	86
Figure C.3 Schematic for tapered area change and the definition of taper angle θ	86
Figure D.1 DELTAEC code used for simulations in Section 5.1. Variable 4a (line 38) is varied for changing Venturi sizes.	87
Figure D.2 DELTAEC code used for simulations in Section 5.3, 1/3.	88
Figure D.3 DELTAEC code used for simulations in Section 5.3, 2/3.	88
Figure D.4 DELTAEC code used for simulations in Section 5.3, 3/3.	89

List of Tables

Table 5.1 Assumed Parameters for properties of a half-wavelength resonator with a Venturi.	41
Table 5.2 Assumed Parameters for Time-Averaged K Simulations.	48
Table 5.3 Simulation Parameters for Venturi-SCL Simulations with varying Venturi sizes.	52

List of Symbols

The next list describes several symbols that will be later used within the body of the document

δ_k	Thermal penetration depth
δ_v	Viscous penetration depth
$\dot{E}_{2,0}$	Acoustic power
\dot{M}	Steady volumetric flow rate
\dot{N}	Steady molar flow rate
ϵ	Surface roughness
γ	Ratio of specific heats
κ	Thermal diffusivity
$\text{Im}[\]$	Imaginary part of an imaginary number
$\text{Re}[\]$	Real part of an imaginary number
μ	Dynamic viscosity
ν	Kinematic viscosity
ω	Angular frequency
Φ	Velocity potential
ϕ	Phase difference
ψ	Ratio of steady to oscillating flow rate

ρ	Density
ρ_m	Mean density
A_B	Branch cross-sectional area
A_P	Piston surface area
A_T	Trunk cross-sectional area
c	Compliance per unit length
c_o	Speed of light in a vacuum inertial frame
d	Diameter
d_h	Hydraulic diameter
D_o	Resonator diameter
e	Internal energy
f	Frequency
f_κ	Spatial average of $h - k$
f_M	Steady flow resistance factor
f_v	Spatial average of h_v
g	Acoustic source term
h	Enthalpy
h_0	Enthalpy at a reference temperature, T_0
h_κ	Thermal relaxation conductance complex geometry variable
h_v	Viscous resistance complex geometry variable
K	Minor loss coefficient
k	Wave number
K_+	Minor loss coefficient in positive \hat{x} -dir

K_-	Minor loss coefficient in negative \hat{x} -dir
K_B	Branch minor loss coefficient
K_T	Trunk minor loss coefficient
k_{th}	Thermal conductivity
L	Cylinder housing length
l	Inertance per unit length
p	Pressure
p_m	Mean pressure
$p_{2,0}$	Time-averaged second-order pressure
Pr	Prandtl number
r	Radius
r_h	Hydraulic radius
r_v	Laminar viscous resistance per unit length
$r_{v,turb}$	Turbulent viscous resistance per unit length
s	Entropy
T	Temperature
T_m	Mean Temperature
U	Volume flow rate
u	Flow velocity in \hat{x}
U_B	Branch volumetric flow rate
U_T	Trunk volumetric flow rate
V	Total volume in a cylinder
v	Specific volume
V_o	Resting volume of a cylinder

Chapter 1

Introduction

1.1 Background

1.1.1 History of Thermoacoustics

Thermoacoustics is a field of science concerning the interactions between heat (thermo) and pressure oscillations in gases (acoustics). The first written record in literature that investigates the phenomena is dated to early 19th century, attributed to Byron Higgins [1]. Higgins' work described a tube with open ends fed with hydrogen gas. A flame placed inside the tube created acoustic oscillations what is called a *singing flame*. However, in a workshop held in 2014, Ueda noted that a diary of a Japanese Buddhist monk from mid-14th century described a thermoacoustic device called *Kibitsunokama* which was used for fortune telling. The description included an open ended barrel with a mesh screen covered in rice placed inside. The screen was heated from below with a bowl of steaming water and the emitted sound resembled the lowing of cattle [2].

Examples of aerial vibrations created by heat was also observed by glassblowers and this phenomenon was investigated by Sondhauss in the late 19th century [3]. The sound was generated by temperature gradient experienced by the air column in a glass tube as it was being shaped. Figure 1.1 shows an example of a glass tube with air trapped inside heated on one end that was noticed to generate a sound by glassblowers.



Figure 1.1: A glass tube with air trapped inside heated at one end [4].

Since the apparatus used by Sondhauss did not have a continuous mass flow because the glass tube was closed on one end, the oscillations were not maintained and the sound dissipated after a few seconds.

Maintained oscillations were achieved by Rijke as he used a tube open at both ends and placed a heated gauze about one quarter way from the bottom half of a vertical tube [5]. Having both ends open allowed for continuous mass flow and heat until the heated gauze exhausted its energy, therefore, the sound created was maintained for this duration. Rijke's investigations concluded that the glass or the pipe itself played no essential part of the phenomenon, however, no explanation for the production of sound was presented. One important outcome of the study was the connection between the pipe's dimensions and the pitch of the sound. The explanation to how the sound is generated and sustained with a heat source came from Lord Rayleigh's article named "The Explanation of Certain Acoustical Phenomena" [6]. Figure 1.2 presents a diagram of the 3 different types of resonators studied by these scientists.

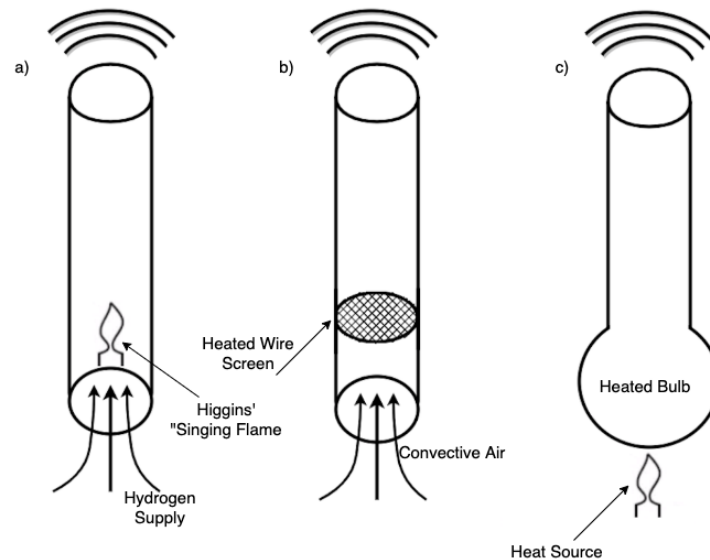


Figure 1.2: a) Higgins' Singing Flame fed by a continuous flow of hydrogen as fuel. b) Rijke Tube using a heated wire mesh to deliver heat to air c) Soundhauss Tube.

Rayleigh used the example of a simple pendulum in order to explain the relationship between the oscillations and the heat source. Categorizing the heat provided as the energy source and the air as the vibrating body, he was able to describe the impulse given to a simple pendulum as the energy source and the mass of the pendulum as the vibrating body. He splits the types of forces that can be applied to the pendulum as it swings into two: one that affects the periodic time, and the other that encourages or discourages the oscillation. In the case of a pendulum, if the impulse is applied when the pendulum passes through its lowest position (maximum speed), the force belongs to the second group, which leaves the period unaltered, and depending on the direction, it either encourages or discourages the oscillation. On the other hand, if the impulse is applied when the pendulum is at one or other of the limits of its swing, the effect is solely on the periodic time and the vibration is neither encouraged nor discouraged. Replacing the impulse with the heated source and the swinging mass with air, Rayleigh states the following; *"If heat be given to the air at the moment of greatest condensation or taken from it at the moment of greatest rarefaction, the vibration is encouraged."* Understanding the fundamentals regarding how a heat source can be used to convert the heat into vibrations in a gas allowed for mechanical work to be extracted which then can be converted into electrical power. Reversing the cycle where the electrical power is converted into mechanical vibrations and then into acoustic power via a piston makes it possible for providing refrigeration or heating with the right apparatus.

1.1.2 Thermoacoustic Engines and Refrigerators

The majority of early research related to thermoacoustic oscillations are solely based on the combustion instabilities caused by these vibrations. In certain cases, premature failures of combustion systems and exhaust systems are attributed to increased vibration experienced by the system due to thermoacoustic oscillations caused by combustion. In early 1980s however, at the Los Alamos National Laboratory (LANL), a thermoacoustic Stirling engine was designed [4]. This engine weighed 200 kilograms and measured 3.5 meters long. Along with this engine, thermoacoustic refrigerators and heat pumps were also designed and tested by the same group of scientists [7]. Figure 1.3 shows how a simple thermoacoustic device can be used as either a refrigerator or as an engine. The diagram zooms into the most important component of a thermoacoustic device, the stack.

The stack is a porous solid with a number of open channels in which the thermal penetration depth, δk , is comparable to the size of the channels. This allows high heat transfer rates between the solid surface and the oscillating gas. On both ends of the stack, two heat exchangers are placed where the heat transfer with the surroundings takes place. In order to provide cooling, the temperature gradient that the stack experiences between the heat exchangers has to be less than the gas experiences as it gets compressed and expanded with the pressure oscillations. In the case shown in Figure 1.3, the mechanical energy is given to the gas via a vibrating surface i.e. a loud speaker. The oscillations created by the loudspeaker compress the gas parcel where it heats up, getting warmer than the hot end of the stack, hence, dumping heat. The same gas parcel is expanded and moved towards the other end of the stack during the other half of the period where it expands and cools enough to absorb heat from the cold end of the stack, providing refrigeration.

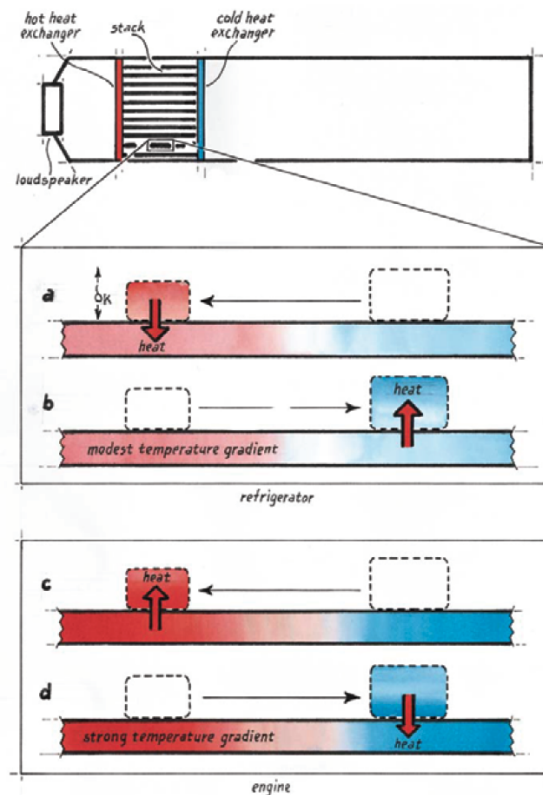


Figure 1.3: Two possible functions of a thermoacoustic device based on the relative temperatures of the stack's ends and the oscillating gas parcel, working as a refrigerator in one instance and as a heat pump in the other. (a) Compressed gas parcel delivering heat to the hot side of the stack. (b) Expanded gas parcel is moved to the cold side of the stack where it is cooler than the portion of the stack it interacts with, absorbing heat. (c) Gas parcel absorbing heat from the warmer stack surface. (d) Expanded gas parcel dumps heat to the cold end of the stack [4].

If the temperature gradient of the stack is increased, the heat transfer during compression and expansion is reversed, as seen in Figure 1.3 (c) and (d). In this case, the heat transfer encourages expansion during one half of the period while it further contracts the gas parcel during the other half, providing further momentum to the oscillations. Once an instability in the resonator initiates oscillations, the amplitudes increase until a balance between the losses and the heat transfer to the gas is achieved. At this steady state, the oscillations can be extracted by the loud speaker and turned into other forms of energy. Note that in this case, the loud speaker is not the driver but is driven by the gas. Ultimately, the functionality of the thermoacoustic device depends on the relative temperature difference between the gas and the stack and the direction of the heat transfer.

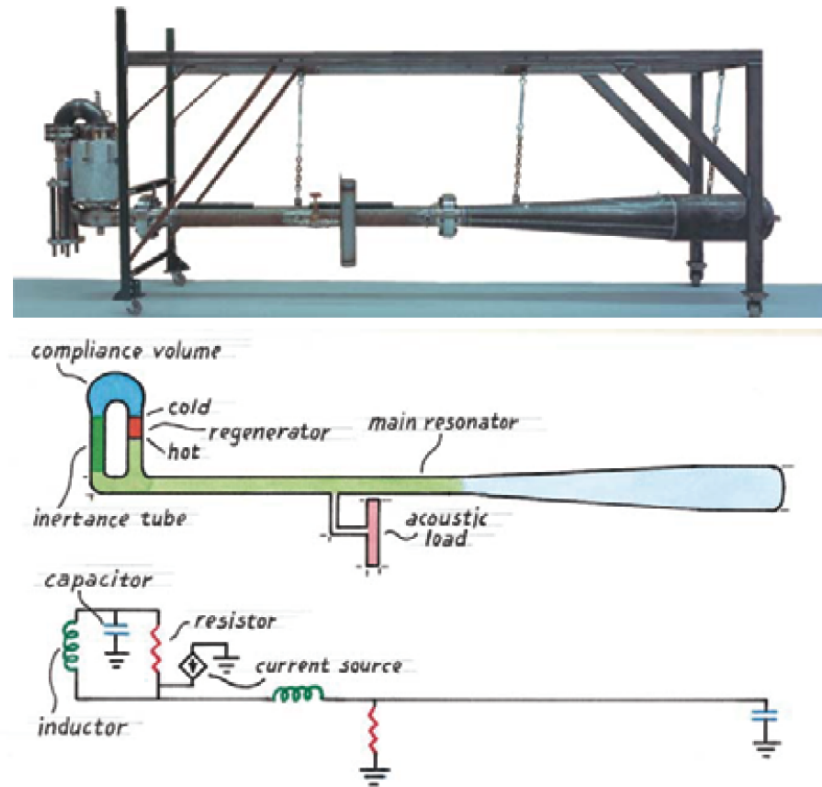


Figure 1.4: Thermoacoustic Stirling engine designed at Los Alamos National Laboratory [4].

One significant advantage of the thermoacoustic engines is that they do not contain any moving components (other than the interface used to transfer acoustic power). In contrast to modern internal combustion engines, there are no pistons, no crankshafts or oil used for lubrication. This unique property makes these engines almost maintenance free and a good candidate for remote applications where mainte-

nance possibilities are limited such as space missions or navy ships and submarines.

In order to compete with vapor-compression refrigeration systems, the efficiency of thermoacoustic refrigerators must be improved. Fundamentally, any thermal resistance between the external thermal reservoirs and the heat exchangers in a thermoacoustic device will reduce potential efficiency. One improvement proposed by the scientists from LANL is the use of self-circulating loops (SCL) to carry heat via thermoacoustic oscillations and the use of gas diodes that favour the flow in one direction more than the other [8]. This would not only allow for transferring heat without the use of a pump but also eliminate the external heat exchangers which would induce thermal resistance. The details of how the gas diodes are used to create a self-circulating loop is presented in Chapter 3.

There is, however, a cost to using a self-circulating loop in terms of energy as the steady flow must be driven by the acoustic oscillations. The local or minor losses associated with these diodes are considerably more than the energy needed to drive the steady flow. In addition, there are thermal-relaxation losses associated with the alternating flow and viscous losses associated with both the alternating and steady flow. Nevertheless, depending on the design, the summed losses of a diode driven self-circulating loop can be similar to the losses that would be incurred in a design where a hot heat exchanger and a pump is used.

1.1.3 Mathematical Models and Available Simulation Tools

The very first attempts for creating a mathematical model that can describe thermoacoustic systems to a degree came from the works of Rott [9]. Rott's approximations assumed that the channels where the oscillations take place were wide enough to ignore the boundary layer effects. This meant both the viscous penetration and thermal penetration depths were much smaller than the size of the channel. This approach allowed for providing a mathematical expression in one dimension where the properties orthogonal to the oscillation direction were constant and the thermoacoustic device could be regarded as a series of short channels. For an arbitrarily chosen short length of the apparatus, thermoacoustic properties are expressed in five different impedance quantities: series inertance, series viscous resistance, parallel compliance, parallel thermal-relaxation resistance, and a parallel current source that only appears if there is a mean temperature gradient.

Rott used the momentum and the continuity equations along with the first law

of thermodynamics to create approximations which allowed for analytical modeling based on linear mathematics [10]. Real life applications however, diverged from these models due to nonlinearities such as turbulence, which still is not understood with great certainty by the thermoacoustic community.

The works of Swfit et al. managed to append approximate solutions to some of the nonlinearities and designed the widely used '*Design Environment for Low-Amplitude Thermoacoustic Energy Conversion*', DeltaEC software [11]. This simulation tool allows solutions for a sequence of segments where primary variables such as pressure, velocity and acoustic power are passed on to the following segment. The segments are divided into cells with arbitrarily defined lengths. The algorithm employs a 'shooting method' along with the Runge-Kutta numeric analysis tool where iterative solutions for all variables are calculated repeatedly until the some given initial conditions are met which can be defined at any given segment.

1.2 Research Problem

There are multiple, well-described mechanisms that can cause a steady flow superposed onto an oscillating flow in thermoacoustic machines. Many are based on flow path asymmetries. These mechanisms and the effects they create are usually undesired since they cause inefficiencies via decreasing the oscillation amplitude. However, for certain applications, deliberate superposition of steady flows can increase the efficiency of the overall system by eliminating pumps and even heat exchangers which would be required otherwise.

Heat exchangers are one of the significant sources of irreversibilities in thermofluid systems. They are heavy, expensive and contribute to the overall system inefficiency via temperature differences and viscous effects in the working fluid. The historic decline of systems where Stirling and steam engines were employed can be attributed to the fact that the internal-combustion engines do not need heat exchangers operating at the combustion temperature, additionally, these engines reject the waste energy in the form of exhaust gas rather than through heat exchangers as in Stirling machines.

As previously mentioned, it is possible to use certain properties of an acoustic flow to create a self-circulating loop which utilizes the working gas itself to extract heat from an external source and deliver it to the Thermoacoustic Stirling machine. These methods also avoid the need for a high temperature fluid pump since the acoustic

process is able to provide the pumping pressure. Another benefit of utilizing these techniques is the lack of a temperature constraint for the heat transfer fluid. Using a traditional heat exchanger would require fluids where some maximum operating temperature hinders the efficiency.

Employing a passive component, such as a gas-diode is the most common design element that acousticians have been using to create pump-less steady flows. A recent, novel method of combining a Venturi with the non-zero time-averaged pressure gradient in a resonator have been employed by engineers at Etalim Inc. and promised superior performance [12]. The initial application of the technique is proven to provide the steady flow desired in a secondary loop where the heat was carried to the resonator without a pump. The schematic of the waste heat recovery system is shown in Figure 1.5.

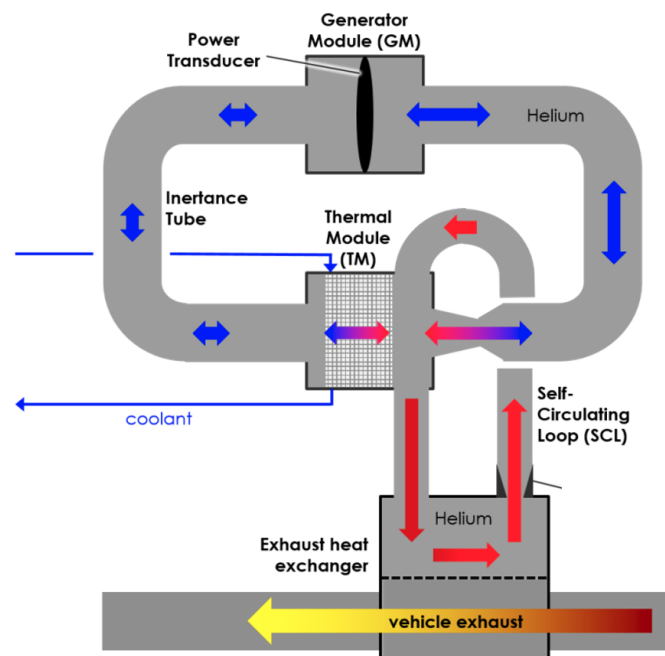


Figure 1.5: Schematic of waste heat recovery system with the Venturi placed at the pressure node delivering heat to the hot side of the regenerator (Thermal Module) where the pressure oscillation is amplified [12]

Figure 1.5 shows a thermoacoustic generator driven using waste-heat from a vehicle exhaust system. The acoustic power flowing to the left of the diaphragm (Power Transducer in Figure 1.5) enters the regenerator on its cold side where the temperature is maintained with a coolant loop that exchanges heat with the ambient.

The oscillating flow gains amplitude due to heat it receives as it travels towards the hot side of the regenerator. The hot side of the regenerator is heated with the steady flow of helium in the SCL, extracting heat from the vehicle exhaust gas stream via the exhaust heat exchanger. The half-wavelength resonator has pressure antinodes on either side of the diaphragm and a velocity antinode where the Venturi is located. This configuration allows the diaphragm to experience positive pressure on one side and negative pressure on the other in an oscillating manner while ensuring the large velocity amplitudes are experienced at the Venturi where the diameter change provide a pressure differential. The mechanical vibration experienced by the diaphragm is converted into electricity at the generator module.

The SCL is connected to the resonator in two locations: at the neck of the Venturi with smaller diameter and at a location with larger diameter, hence, the pressure difference that drives the SCL is partially provided by the Venturi. Another mechanism contributing to the driving pressure difference is the second-order time-averaged pressure gradient that is distributed sinusoidally in space, reaching a minimum at the velocity antinode. The SCL being attached to this sinusoidal gradient in two locations provide additional pressure differential. Chapters 2 and 3 explain these mechanism and their combined effects in detail.

Venturi SCL is a promising alternative to the currently used gas-diode method where an asymmetrical flow restriction is created by the nonlinearity of the device. A better understanding of the Venturi driven flow might provide an efficiency improvement for such systems where a pumpless flow is desired.

1.3 Objectives

The objectives of the work presented in this thesis are:

- Quantify the impacts of venturi design and operating conditions on a self circulating loop in oscillating flows.
- Create an analytic framework describing the effects of a converging-diverging nozzle on the time-averaged second order pressure.
- Determine the time-averaged minor loss coefficients experienced by oscillating flows at T-junctions between a loop and the resonator.

1.4 Structure

The following chapters describe the theory and governing equations for thermoacoustic devices, the concept of acoustic radiation pressure, mean flow, and time-averaged minor losses. Simulations using DeltaEC are presented showing the impact of design on mean flow. The document concludes with a summary of main results and recommendation for future work. The contents of each chapter are as follows:

Chapter 1 Presents a general background on various methods of Acoustic Mass Streaming. Motivation and the objective of the thesis is also defined in this chapter.

Chapter 2 Describes the thermodynamic fundamentals of the Acoustic Radiation Pressure.

Chapter 3 Presents the acoustic radiation pressure as a means for acoustic mass streaming and investigates the effects of adding a Venturi tube to the resonator.

Chapter 4 Describes the irreversibilities in oscillating flows and provides semi empirical expressions for steady flow minor losses at a T-Junction.

Chapter 5 Presents the DeltaEC simulations describing both the effects of Venturi on the acoustic radiation pressure, and the performance various sizes of Venturi in terms of the amount of steady flow in the SCL. Simulated time-averaged minor loss coefficients are also presented in this chapter

Chapter 6 Presents detailed discussion of the simulation results. Investigates the potential sources of error compared to potential experimental results.

Chapter 7 Contains a restatement of the whole work and results of the simulations. It also lists the avenues of future work for understanding the fundamentals of the technique as well as validating the created model.

Chapter 2

Acoustic Radiation Pressure

2.1 Background

Acoustic radiation pressure (ARP) is described as the time-averaged pressure acting on an object in a sound field. The presence of a time averaged excess pressure in oscillating gases was first studied by Lord Rayleigh more than a century ago [6][13]. This phenomenon fueled much debate amongst the scientific community since there were disagreeing results presented by different researchers.

ARP is one of the mechanisms that makes mass streaming possible in a Venturi SCL assembly. The mean pressure measured along a standing wave resonator is different before and after acoustic oscillations begin. Without any oscillations present, the mean pressure is constant and uniform; with acoustic oscillations, the mean pressure varies sinusoidally in space. In a resonator, this spatially varying pressure can be used to drive a nonzero flow due to the pressure difference created between two points.

This chapter starts by introducing the notation used in the rest of the document. In Section 2.3, an expression for ARP from fundamental thermodynamic equations is presented. Finally, the effects of a mean temperature gradient on ARP's spatial distribution is presented.

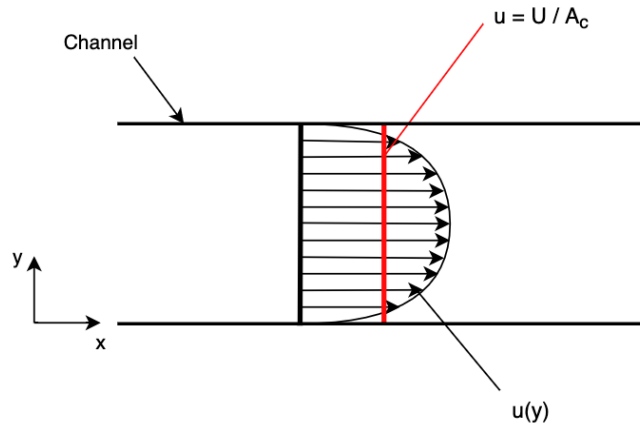


Figure 2.1: Flow profile in a viscous internal flow as a function of distance (y) from the wall shown as the parabolic curve in black. Volumetric flow rate divided by the cross-sectional area gives the average velocity in the channel used in the boundary-layer approximation, shown in red.

Before delving into the mathematics of thermoacoustics, it is convenient to define the customary way of expressing the velocity variable for internal flows which forms the basis of Rott's boundary layer approximation [14, pp. 65-66]. For an oscillating internal flow, the velocity u represents the average one-dimensional velocity in the channel which is the ratio of volumetric flow rate to the cross-sectional area, U/A_c . It should be noted that with sinusoidal displacements in \hat{x} direction, the velocity gradient in the \hat{y} direction is not zero due to no-slip condition at the boundary, hence u is a function of y in reality. However, the boundary layer approximation where $u = U/A_c$ allows for much simpler calculations for cases where the viscous penetration depths are insignificant compared to the width of the channel. Figure 2.1 shows the difference between $u(y)$ and the spatially averaged u as described in boundary layer approximation.

2.2 Acoustic Variables and Complex Notation

For the purposes of this discussion, the oscillating properties are described using the complex notation. Assuming time dependence is purely sinusoidal with angular frequency $\omega = 2\pi f$, variables such as pressure $p(t)$ can be written as;

$$p(t) = P \cos(\omega t + \phi) = P \operatorname{Re} [e^{i(\omega t + \phi)}] = P \operatorname{Re} [e^{i\omega t} e^{i\phi}] \quad (2.1)$$

The phase and amplitude can be grouped as $p_1 = P e^{i\phi}$, so;

$$p(t) = \text{Re}[p_1 e^{i\omega t}] \quad (2.2)$$

And,

$$|p_1| = P \quad (2.3)$$

$$\text{phase}(p_1) = \phi \quad (2.4)$$

Any variable with the subscript 1 indicates an oscillating property with a first order amplitude at a point in space. For a standing wave with spatial pressure magnitude distribution taken into account, the complete temporal and one dimensional expression would be:

$$p(x, t) = P \cos(\omega t + \phi) \cos(kx) = p_1 \cos(kx) \quad (2.5)$$

where $k = \frac{2\pi}{\lambda}$ is the wavenumber. This simplified approach in notation is widely used by acousticians and physicians in the literature [14, pp. 60-62]. Here the term p_1 contains information about the phase and the magnitude of the oscillating amplitude. Assuming that a first order standing acoustic wave can be described as a single sinusoid in time, the pressure experienced at any point along the wave sums up to zero when integrated over a period.

$$p_{1,0} = \frac{1}{T} \int_0^T p(t) dt = 0 \quad (2.6)$$

In this notation, the first subscript denotes the order of magnitude, as mentioned earlier, the newly added second subscript indicates the temporal frequency that the magnitude accompanies. For instance, $p_{2,2}$ means that the amplitude of this pressure term is of second order in magnitude, oscillating with twice the frequency. Therefore $p_{1,0}$ would mean first-order time-averaged pressure, and $p_{2,0}$, second-order time-averaged pressure.

A nonlinear periodic pressure in Eulerian form can then be described as:

$$p(x, y, z, t) = p_m + p_1(x, y, z) + p_{2,0}(x, y, z) + p_{2,2}(x, y, z) + \dots \quad (2.7)$$

The Eulerian pressure p is the pressure at a given location x, y, z as a function of time

t. The first term, the mean pressure p_m , describes the steady pressure in any point in space if there are no oscillations present in the system. It is usually independent of x, y, z , since gravity is ignored. The second term includes the fundamental acoustic oscillation at angular frequency $\omega = 2\pi f$ in the form of complex oscillating pressure and phase, p_1 , which varies in space. If no nonlinear effects are present, these two terms, p_m and p_1 would be sufficient to describe an acoustic oscillation. Nonlinear effects however, do exist when oscillating terms, such as velocity or pressure, are squared. These squared terms generate the second order terms such as $p_{2,2}$ and $p_{2,0}$ in Equation 2.7. It should be noted that measuring $p_{2,0}$ is a challenging task since its magnitude is much smaller than both p_m and p_1 . For this reason, its existence was a part of a debate for many years. The majority of the early research targeted explaining acoustic levitation which is caused by radiation pressure [15].

2.3 Second Order Pressure in 1-D Inviscid Flows

In order to show how acoustic radiation pressure arises with simple harmonic oscillations, it is convenient to start with the one dimensional linear momentum equation for an inviscid flow. The Euler Equation describing this flow is given in Equation 2.8.

$$\frac{\partial u}{\partial t} + u \frac{\partial u}{\partial x} = -\frac{1}{\rho_m} \frac{\partial p}{\partial x} \quad (2.8)$$

In order to obtain an expression for the ARP, Equation 2.8 should be fully expressed in terms of gradients of scalars so that it is independent of location. Starting with the right hand side, it is possible to express the pressure gradient term in terms of enthalpy.

$$h = e + pv \quad (2.9)$$

$$dh = de + pdv + vdp \quad (2.10)$$

With $de = Tds - pdv$, Equation 2.10 for an adiabatic and reversible process becomes:

$$dh = vdp = \frac{1}{\rho_m} dp \quad (2.11)$$

The right hand-side of Equation 2.8 then becomes:

$$\frac{\partial u}{\partial t} + u \frac{\partial u}{\partial x} = -\frac{\partial h}{\partial x} \quad (2.12)$$

For the left hand-side, the fact that the velocity is the gradient of a scalar field such

that $\vec{u} = \vec{\nabla}\Phi$, that is $\frac{\partial\Phi}{\partial x} = u$ in 1-D is used to obtain:

$$\frac{\partial(\frac{\partial\Phi}{\partial x})}{\partial t} + u \frac{\partial u}{\partial x} = -\frac{\partial h}{\partial x} \quad (2.13)$$

Rearranging Equation 2.13 gives:

$$\frac{\partial}{\partial x} \left(\frac{\partial\Phi}{\partial t} + \frac{u^2}{2} + h \right) = 0 \quad (2.14)$$

$$\frac{\partial\Phi}{\partial t} + \frac{u^2}{2} + h = \text{constant} \quad (2.15)$$

The enthalpy term can be expanded using Taylor series expansion to second-order:

$$h = h_o + \left(\frac{\partial h}{\partial p} \right)_s (p_1 + p_2) + \left(\frac{\partial^2 h}{\partial p^2} \right)_s \frac{p_1^2}{2} \quad (2.16)$$

Note that the pressure variation is assumed to be comprised of first-order and second-order amplitude components: p_1 and p_2 . Since in the third term, squared second order term would be insignificant, any term that is multiplied by p_2 is omitted. Substituting Equation 2.16 into Equation 2.15 gives:

$$\frac{\partial\Phi}{\partial t} + \frac{u^2}{2} + h_o + \left(\frac{\partial h}{\partial p} \right)_s (p_1 + p_2) + \left(\frac{\partial^2 h}{\partial p^2} \right)_s \frac{p_1^2}{2} = \text{constant} \quad (2.17)$$

For an irreversible process, the isentropic partial derivative terms in Equation 2.17 are constants. Using Equation 2.11:

$$\left(\frac{\partial h}{\partial p} \right)_s = \frac{1}{\rho_m} \quad (2.18)$$

using the elementary relation [16]:

$$\left(\frac{\partial p}{\partial \rho}\right)_s = c_o^2 \quad (2.19)$$

and using the chain rule, Equation 2.20 provides:

$$\left(\frac{\partial^2 h}{\partial p^2}\right)_s = \frac{\partial}{\partial p} \left(\frac{1}{\rho_m}\right)_s = -\frac{1}{\rho_m^2 c_o^2} \quad (2.20)$$

Equation 2.17 then can be written as:

$$\frac{\partial \Phi}{\partial t} + \frac{u^2}{2} + h_o + \frac{(p_1 + p_2)}{\rho_m} - \frac{1}{2} \frac{p_1^2}{\rho_m^2 c_o^2} = \text{constant} \quad (2.21)$$

2.4 Second-Order Time-Averaged Pressure

An acoustic variable with second-order amplitude is described as the product of two first order amplitude variables. Time-averaged acoustic power, $\dot{E}_{2,0}$, a second-order acoustic variable describes the acoustic intensity across the cross-sectional area of the channel.

$$\text{Dot}E_{2,0} = \frac{1}{2} |p_1| |U_1| \cos \phi_{pU} \quad (2.22)$$

where ϕ_{pU} is the phase angle between $|p_1|$ and $|U_1|$. Equation 2.22 describes the acoustic power flowing in the \hat{x} direction in a resonator. The subscript 2 shows that it is of second order amplitude, product of two first-order quantities. Note that $\dot{E}_{2,0}$ does not describe the instantaneous power delivered along \hat{x} but the power averaged over an number of cycles of the wave [14, pp.117-118].

Similar to acoustic power, time-averaged excess pressure is another useful acoustic quantity that is of second-order. Section 2.2 introduced the general form of acoustic variables. Then, section 2.3 derived an expression of flow energy balance using the 1-D, inviscid Euler equation that is independent of location and includes a pressure term with the second-order amplitude. Using the complex notation and Equation 2.21, it is possible to come up with an expression for the second-order time-averaged pressure for a 1-D oscillating inviscid flow.

Note that in Equation 2.21, p_1 denotes $Re[p_1 e^{i\omega t}]$. Therefore, time averaging $p_1^2 \cos^2 \omega t$ gives $\frac{1}{2} |p_1|^2$. This form of the Euler Equation makes it clear that only the squared velocity and pressure terms will produce nonzero values. Solving Equation

2.21 for p_2 and time averaging yields:

$$p_{2,0} = \frac{1}{4} \frac{|p_1|^2}{\rho_m c_o^2} - \frac{1}{4} \rho_m |u_1|^2 + \text{constant} \quad (2.23)$$

The term $p_{2,0}$ is called the acoustic radiation pressure, ARP, and shows that the second-order time-averaged pressure is the difference between the potential and kinetic energy densities for an acoustic flow at any spatial location along the oscillation direction. Note that since Equation 2.23 is derived assuming inviscid flow, $p_{2,0}$ here represents the reversible part of the ARP. The constant in Equation 2.23 is independent of space and time. The value of the constant depends on external constraints rather than the properties of the wave itself, for instance, whether the resonator is vented to atmospheric pressure p_m at a defined location or sealed with p_m that is confined in the resonator prior to initiation of oscillations. The confusion can be avoided if the difference between the acoustic radiation pressure values between two locations is considered, this would deem the constant irrelevant. An alternative approach to understanding the causes of this phenomena where a mean-excess pressure exists in an oscillating gas column can be found in detail in Appendix A with an example of a piston and a close-fitted cylinder assembly.

2.5 ARP with Non-zero Mean Temperature Gradient

Equation 2.23 is derived for an ideal gas with constant mean density, therefore, the spatial distribution is only dependant on the velocity and pressure oscillations. Efforts to mathematically express the effects of varying mean properties such as temperature, density, speed of sound etc. on the time-averaged pressure show that there has to be an additional term in Equation 2.23 which takes the mean density gradient either caused by inhomogeneities or by non-zero temperature gradients into account [17].

In a heat carrying SCL, the flow in both the SCL and the resonator would experience varying mean temperature and density. Analytical models would provide more accurate $p_{2,0}$ values if the effects of the mean temperature gradient is taken into account. With the addition of this term, the spatial distribution for $p_{2,0,total}$ for an inviscid flow in a single dimension becomes:

$$p_{2,0,total} = p_{2,0} + p_{2,0,\nabla\rho} \quad (2.24)$$

The total derivative for the time-averaged second-order pressure then becomes:

$$\frac{dp_{2,0,total}}{dx} = \frac{dp_{2,0}}{dx} + \frac{dp_{2,0,\nabla\rho}}{dx} \quad (2.25)$$

With the density gradient term, Equation 2.25 is called the acoustic force density and an expanded expression is given by Equation 2.26 [17][18].

$$\frac{dp_{2,0,total}}{dx} = \frac{1}{4\rho_m c_o^2} \frac{d|p_1|^2}{dx} - \frac{\rho_m}{4} \frac{d|u_1|^2}{dx} - \frac{d\rho_m}{dx} \frac{|u_1|^2}{2} \quad (2.26)$$

Taking the derivative of Equation 2.23, considering the fact that p_1 , u_1 and ρ_m are all functions of x , and subtracting this derivative from Equation 2.26 allows for an expression for the density gradient related term from Equation 2.25 term to be derived.

$$\frac{dp_{2,0,\nabla\rho}}{dx} = -\frac{|p_1|^2}{4} \frac{d}{dx} \left(\frac{1}{\rho_m c_o^2} \right) - \frac{|u_1|^2}{4} \frac{d\rho_m}{dx} \quad (2.27)$$

The first term in in Equation 2.27 is called the elastoclinic acoustic force and is zero for an ideal gas since $\rho_m c_o^2 = \gamma p_m$ is independent of temperature [19]. This means that the nonzero temperature gradient in the SCL or in the resonator would not contribute to Equation 2.27, if the working fluid is an ideal gas. However, it should be noted that if the fluid is a mixture of ideal gasses, the elastoclinic term cannot be ignored since $\gamma_\alpha \neq \gamma_\beta$ where α and β are different constituents of the mixture. The second term in Equation 2.27 is called the pycnoclinic acoustic force and is a function of mean density gradient which should be taken into account if such a gradient exists [18].

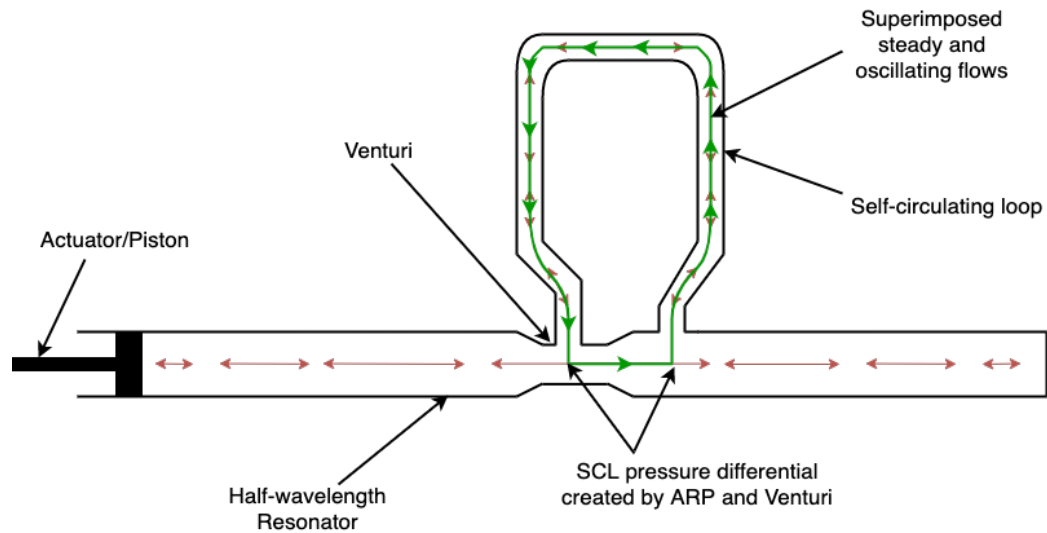


Figure 2.2: Time-averaged nonzero (green) and oscillating (red) flows in the SCL created by the pressure differential of $p_{2,0}$ and the Venturi.

Figure 2.2 shows how $p_{2,0}$ and a Venturi can be combined to create a nonzero steady flow in the SCL. If heat was given to the flow anywhere along the SCL, carried heat into the resonator would encourage oscillations, allowing extraction of work at the piston. The heat transfer in the SCL will cause a mean temperature gradient, changing the distribution of $p_{2,0}$ both in the SCL and in the resonator. The connection at the neck of the resonator will experience higher average temperature compared to the connection where the flow goes into the SCL, modifying the sinusoidal distribution of $p_{2,0}$, hence affecting the amount of steady flow in the SCL. The placement of a Venturi at the pressure node changes the kinetic energy density at this location, modifying the gradient of $p_{2,0}$ between the connection points of the SCL that drives the steady flow. The dimensions of the SCL will affect the time-averaged pressure differential between the connections, changing the amount of steady flow.

This chapter introduced the boundary layer approximation for an internal flow and defined the acoustic radiation pressure for a 1-D case. Then, the time-averaged second-order pressure, $p_{2,0}$, for an oscillating flow is introduced and how its gradient can be utilized to create a steady flow in the SCL is discussed. Finally, the effects of a mean temperature gradient on the $p_{2,0}$'s distribution for a heat carrying SCL-Venturi assembly is discussed. In the following chapter, various acoustic mass streaming methods will be presented. A lossless mathematical model for acoustic streaming with $p_{2,0}$ when combined with a Venturi will be presented and the effects of the Venturi diameter ratio on $p_{2,0}$ when placed at a pressure node will be investigated.

Chapter 3

Acoustic Mass Streaming with Acoustic Radiation Pressure and a Venturi

This chapter starts with introducing various methods of acoustic streaming and describes their working mechanisms. The chapter then presents how the spatially varying ARP can be used to initiate a nonzero mean flow in a closed path as an alternative to the asymmetrical gas diodes which are explained in Section 3.1. Finally, a lossless mathematical expression describing how ARP changes with a Venturi placed at the pressure node of a half-wavelength standing wave is presented. Simulation results verifying the expression will be presented in Chapter 5.

3.1 Acoustic Mass Streaming

Superimposing a DC flow on top of an AC (oscillating) flow is called *Acoustic Streaming* [14, pp. 197-199]. Figure 3.1 shows Reid's Standing Wave Refrigerator where an externally driven DC gas flow is superimposed onto an AC flow created by a pair of loudspeakers. The steady flow at ambient temperature is fed into the refrigerator at one pressure node and flowed out at another at a colder temperature. In this refrigerator, the flow would experience temperature oscillations at the pressure antinodes due to oscillating pressure, hence, experience the largest temperature differences with the ambient which is the reason why heat exchangers are located here. The loudspeakers operate at such a frequency that as the gas moves towards

the heat exchangers, the speakers expand and increase the available volume, further reducing the pressure at the pressure antinode. This causes more heat to be extracted from the ambient compared to what is dumped back in during the other half of the oscillation. It should be noted that Reid’s refrigerator requires an external pump to drive the flow from one pressure node to another, hence, no auto-pumping is present.

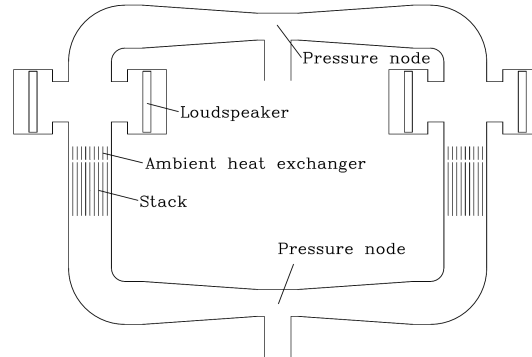


Figure 3.1: Reid’s Refrigerator - Steady flow injected at the upper pressure node at ambient temperature and flowed out at the lower pressure node at a colder temperature [20].

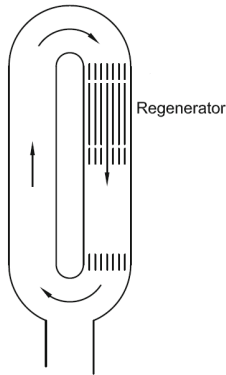


Figure 3.2: Gedeon Streaming caused by flow path asymmetries [14].

In certain Thermoacoustic Stirling machines, acoustic streaming is possible via deliberately placing geometrical obstacles that affect the flow differently in one flow direction compared to other. Given that a loop is present, this technique eliminates the need for an external DC flow driver, the pump [8]. The following examples of acoustic streaming consist of different expressions of this flow path asymmetry method.

A type of acoustic streaming, *Gedeon Streaming*, is a second-order, time-averaged mass flux that exist in Stirling systems with a closed-loop path which is caused by asymmetries in the loop [21].

The regenerator and the flow straightener in Figure 3.2 in the toroid create flow-path asymmetries. The acoustic flow coming from the resonator follows the least path of resistance. In other words, since the small flow channels in the flow straightener and the regenerator are more resistant to acoustic flow than the DC flow, the asymmetry in the path forces the flow to circulate in the toroid, creating a DC flow.

Figure 3.3 shows the use of the *jet pump* to counteract Gedeon Streaming in a Thermoacoustic Stirling Engine. A jet pump is a type of *acoustic gas-diode*. Prior to their use as gas-diodes in Thermoacoustic engines designed by Los Alamos National

Laboratory scientists, these components were called “vortex” diodes by Mitchell [22] and the “valvular conduit” by Tesla [23]. These were the very first types of gas-diodes invented where the backward and forward flow impedances were different.

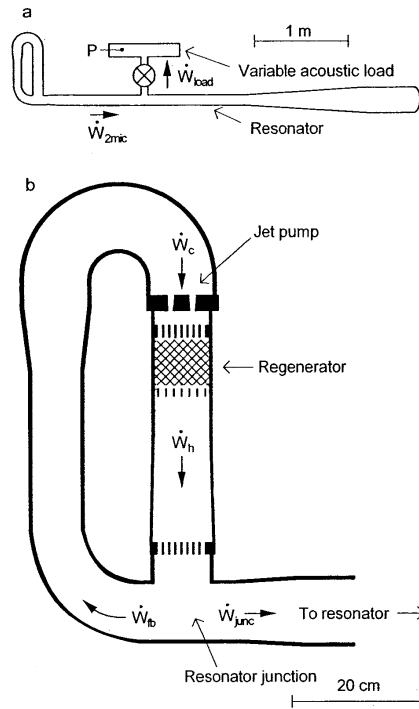


Figure 3.3: (a) Scale drawing of the Thermoacoustic engine. (b) Scale drawing of the torus section [8].

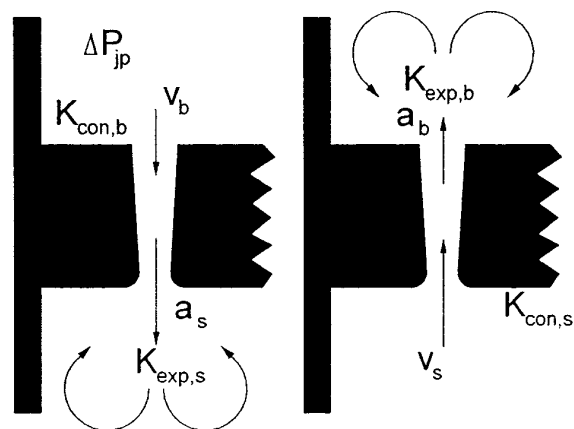


Figure 3.4: Diagram of the jet pump. The two flow patterns represent the first-order acoustic velocities during the two halves of the acoustic cycle. Subscripts s and b refer to the small and big openings respectively [8].

Placing a jet pump with a different minor loss coefficient over one half the cycle compared to the other creates a time-averaged pressure drop in one of the directions. This means that by controlling the minor loss coefficients in either direction, the magnitude of DC flow can be controlled. Figure 3.4 shows the working mechanism of a jet pump where sudden expansion and sudden contraction of the oscillating flow as it passes through the component creates the asymmetry needed. Here, the flow experiences less resistance as it converges through the jet pump compared to what it experiences as it diverges in the other half of the period. This asymmetry creates a preferred direction for the flow and causes a nonzero mean flow in the direction of flow velocity v_b .

The jet pump shown in Figures 3.3 and 3.4 are used to prevent acoustic streaming, balancing the pressure drop withing a closed-loop. Figure 3.5 on the other hand, shows the use of gas diodes for deliberate mass streaming which creates a self-pumped heat exchanger [24]. The location of these gas-diodes in the loop is crucial for maximizing the mean flow rate. The length of the loop being equal to exactly one wavelength, and the placement of the diodes at the velocity antinodes allow for maximum mean flow. Locating the mixing chamber at the velocity nodes results in minimal flow perturbation at the resonator, increasing the efficiency of the system overall.

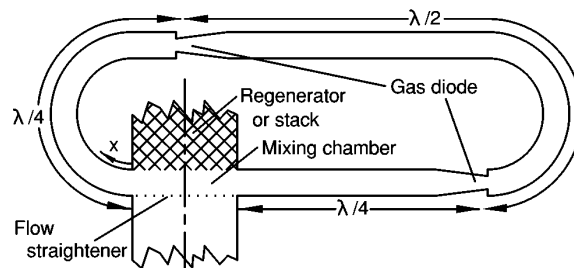


Figure 3.5: A portion of a Thermoacoustic machine where the heat exchanger is replaced by a pipe one wavelength long. Gas diodes at the velocity antinodes induce mean flow [24].

Another example of using a nonlinear gas diode to induce a non-zero mean flow to deliver heat from a hot heat exchanger to the heat engine is shown in Figure 3.6. Note that in this design, jet pumps in the torus counteract the mean flow while the gas diode in the loop with the heat exchanger encourages it.

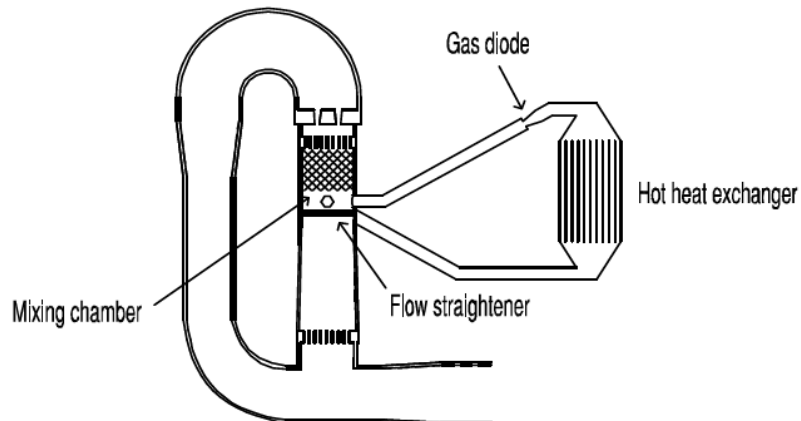


Figure 3.6: Use of a gas diode to create a self-circulating loop [19, pp.109].

3.2 Mass Streaming via Acoustic Radiation Pressure Differential

As briefly introduced at the end of Chapter 2, it is possible to induce a time-averaged mean flow by taking advantage of the spatial variation of ARP. Assuming no mean temperature gradients are present in the SCL or in the resonator, and that the working fluid is a monatomic ideal gas, it is possible to use Equation 2.23 for mass streaming calculations. In order to see how $p_{2,0}$ varies along an acoustic resonator, it is convenient to look at how velocity and pressure varies in space for a plane standing wave. Recalling Equation 2.5 for spatially varying pressure amplitude for a standing wave [25, pp.853]:

$$|p_1(x)| = P \cos(kx) \quad (2.5)$$

and,

$$|u_1(x)| = \frac{P}{\rho_m c_o} \sin(kx) \quad (3.1)$$

Substituting Equations 2.5 and 3.1 into Equation 2.23 yields:

$$p_{2,0}(x) = \frac{1}{4} \frac{P^2}{\rho_m c_o^2} \cos^2(kx) - \frac{1}{4} \rho_m \frac{P^2}{\rho_m^2 c_o^2} \sin^2(kx) + \text{constant} \quad (3.2)$$

Rearranging and using the trigonometric identity $\cos^2 x - \sin^2 x = 1 - 2\sin^2 x$ gives:

$$p_{2,0}(x) = \frac{1}{4} \frac{P^2}{\rho_m c_o^2} (1 - 2\sin^2(kx)) + \text{constant} \quad (3.3)$$

$$p_{2,0}(x) = -\frac{P^2}{2\rho_m c_o^2} \sin^2(kx) + \text{constant}' \quad (3.4)$$

For a standing wave, Equation 3.4 is equivalent to Equation 2.23. Note that the magnitude of this term is of second order, hence the increased difficulty in measuring its amplitude. Additionally, note that the *constant'* in Equation 3.4 differs from the *constant* in Equation 3.3 by $\frac{1}{4} \frac{P^2}{\rho_m c_o^2}$.

The sinusoidal spatial variation of $p_{2,0}$ on its own may be able to create a large enough pressure differential to drive a steady flow in a loop given that the 2 connecting points to the resonator are asymmetrical about the pressure node. The largest differential of $p_{2,0}$ can be created if one of the connections is attached to the pressure node since the \sin^2 function for a half-wave reaches a minimum here. The next section investigates how placing a Venturi to the pressure node of a half-wavelength resonator modifies this minimum value that $p_{2,0}$ attains.

3.3 Effects of a Venturi on the Acoustic Radiation Pressure

Utilizing a Venturi for increased SCL efficiency was first implemented by the engineers at Etalim Inc. on their Thermoacoustic waste-heat recovery system in attempts to eliminating the high pressure and high temperature pump [12]. However, there are no mathematical models provided by the inventors investigating the performance of the Venturi and its effects on mass streaming capabilities of the SCL. In this section, a lossless mathematical expression for $p_{2,0}$ incorporating the Venturi's dimensions is presented so that a quick time-averaged pressure differential to drive a steady flow can be obtained.

The difference between the amplitudes of p_1 and $p_{2,0}$ can be seen in Figure 3.7 (a) and (b) where the magnitude of p_1 is about 100 times higher than of $p_{2,0}$'s. According to Equation 3.4, $p_{2,0}$ varies sinusoidally in a resonator.

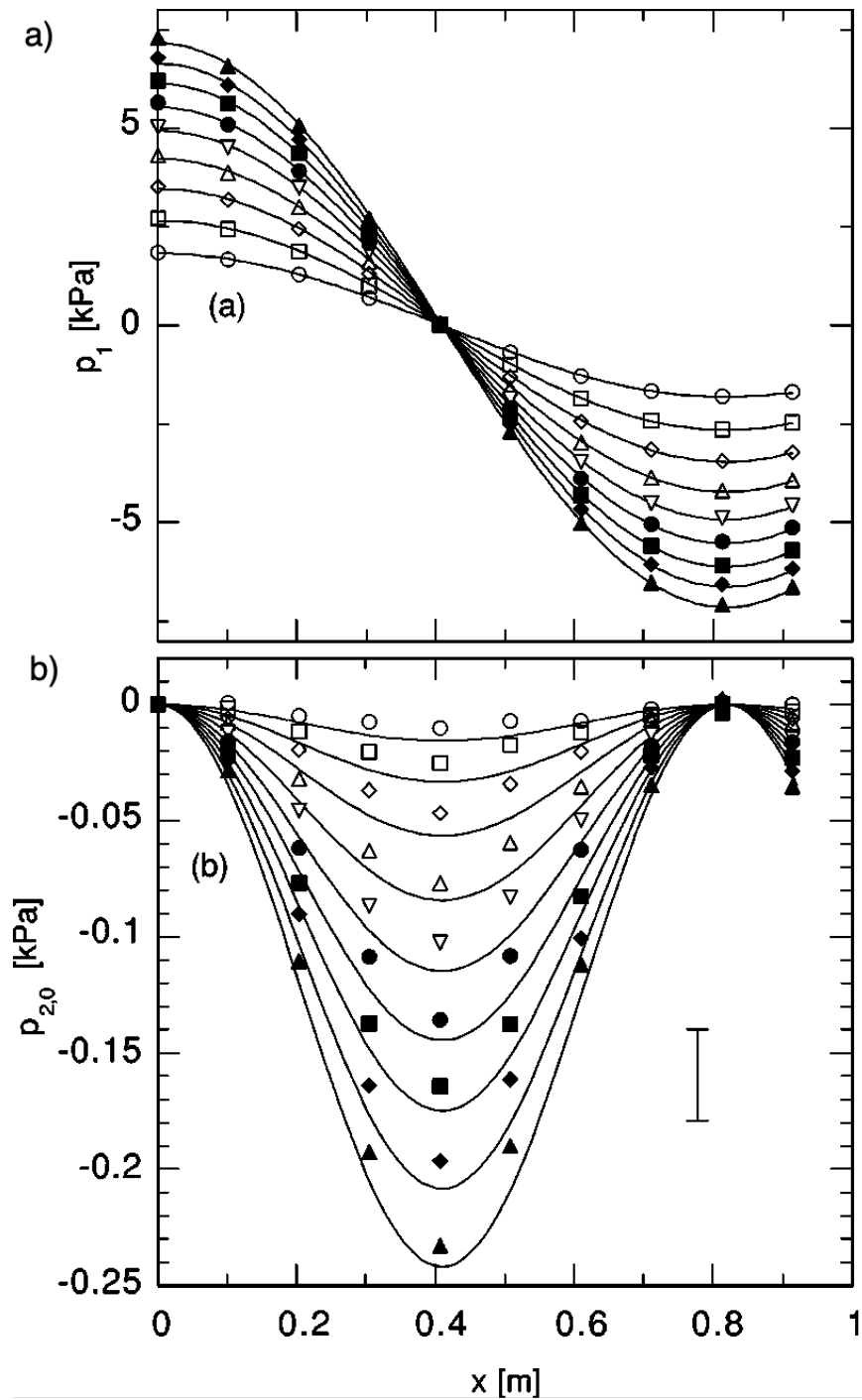


Figure 3.7: (a) Measured distribution of $p_1(x)$ for 9 different amplitudes in a resonator (slightly longer than a half-wavelength) shown as symbols, the lines are drawn using Equation 2.5 with a P adjusted to fit the data [15]. (b) Symbols represent measured $p_{2,0}$, lines are drawn using Equation 3.4 with P used in (a) with $constant'=0$ [15].

In order to understand how the geometry change with the placement of a Venturi affects the time-averaged pressure, it is convenient to consider how the kinetic and potential energy densities change with the addition of the Venturi. Equation 3.1 describes the velocity profile of a standing wave for a constant geometry resonator. Assuming that the volumetric flow rate stays constant at a cross section regardless of the cross-sectional area, velocity and pressure as a function of resonator diameter can be written as:

$$|u_1(x)| = \frac{P}{\rho_m c_o} \sin(kx) \frac{A_0}{A(x)} = \frac{P}{\rho_m c_o} \sin(kx) \left(\frac{D_0}{D(x)} \right)^2 \quad (3.5)$$

$$|p_1(x)| = P \cos(kx) \left(\frac{D_0}{D(x)} \right)^2 \quad (3.6)$$

where D_0 is the resonator diameter at the ends and $D(x)$ is the varying diameter. Using the descriptions for velocity and pressure profiles described in Equations 3.5 and 3.6 along with some simplifications, Equation 3.4 for $p_{2,0}$ takes the form:

$$p_{2,0}(x) = -\frac{P^2}{2\rho_m c_o^2} \left(\frac{D_0}{D(x)} \right)^4 \sin^2(kx) + \frac{P^2}{4\rho_m c_o^2} \left(\frac{D_0}{D(x)} \right)^4 + constant \quad (3.7)$$

The *constant* in Equation 3.7 is the same as the *constant* in Equation 3.3. The $\frac{1}{4} \frac{P_1^2}{\rho_m c_o^2}$ term that was added to this constant in Equation 3.4 is no longer a constant but a function of geometry as well which defines the second term in Equation 3.7. Since the second-order time-averaged pressure is the difference between the potential and kinetic energy densities, further amplifying $\Delta p_{2,0}$ is possible if a Venturi is placed along the resonator because it would increase the kinetic energy density of the flow while decreasing the potential energy density, expanding the gap between these two terms at the neck. Note that the potential energy density would remain unchanged if the Venturi is placed at the pressure node since p_1 would be zero. Figure 3.8 shows how a Venturi could amplify $\Delta p_{2,0}$ in the best case scenario where the presence of the Venturi does not affect the total energy stored in the resonator.

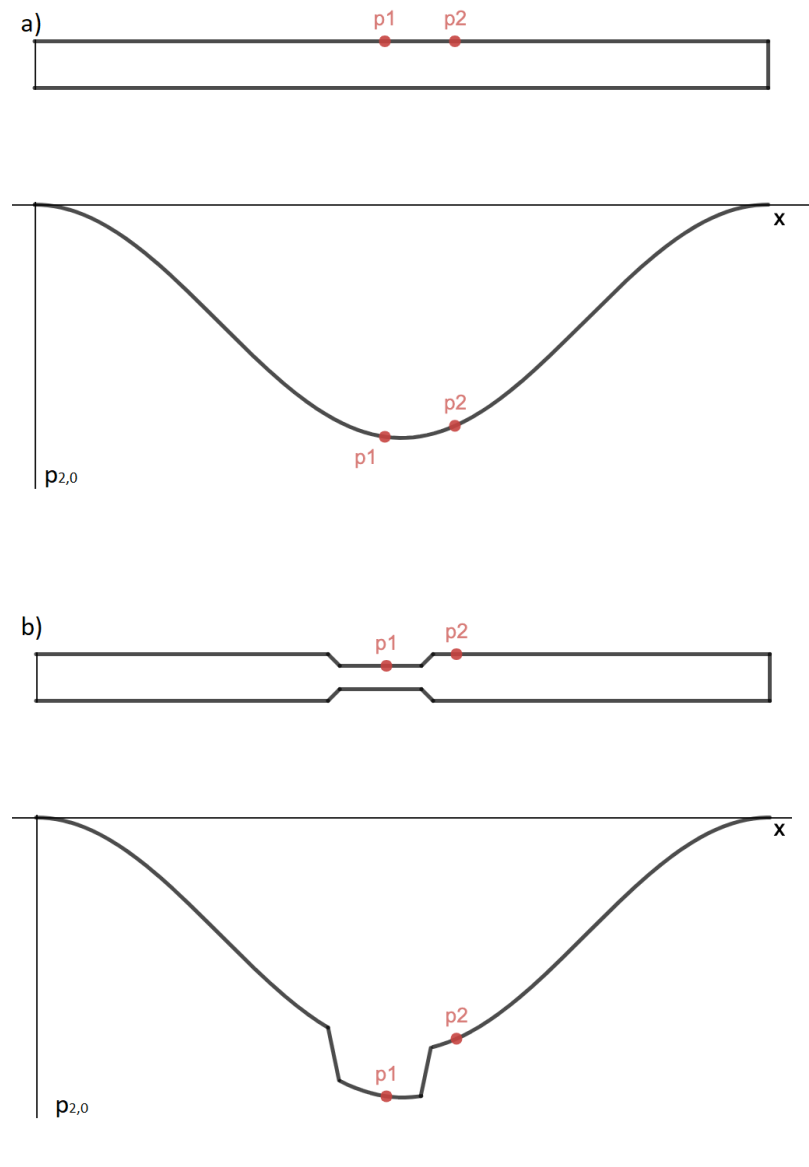


Figure 3.8: (a) Schematic of $\Delta p_{2,0}$ between two locations along the resonator. (b) Increased $\Delta p_{2,0}$ with a Venturi, in a lossless scenario.

The definition of how a Venturi affects $p_{2,0}$ concludes this portion of the discussion. This chapter laid out a brief description of acoustic mass streaming along with existing methods and provided a lossless mathematical expression for the time-averaged second-order pressure, $p_{2,0}$, for a resonator with varying geometry which can be used to obtain a time-averaged pressure differential.

Chapter 4

Minor Losses for a Venturi-SCL Assembly

The focus of this chapter is the minor losses in an oscillating flow, particularly the ones that are applicable to a Venturi-SCL configuration. The driving mechanism creating the steady flow in the SCL is the pressure differential that occurs between the two connecting points of the loop to the resonator. This pressure difference is reduced by irreversibilities such as viscous and minor losses. The thermoacoustic simulation software DeltaEC is capable of calculating and including the effects of viscous losses to its analytical results. However, it requires a constant to be introduced in order to take minor losses into account. These constants, called minor loss coefficients are widely available for steady flow conditions and mostly are functions of geometry only. However, the Venturi-SCL assembly contains two T-Junctions where the SCL connects to the resonator and the minor loss coefficients representing these T-Junctions are not only functions of geometry, but also flow rate. The flow rate in an oscillating flow varies constantly, so does the minor loss coefficient, therefore, special attention and methods are required to obtain a constant value capable of representing the cumulative effect of the constantly varying coefficient. This chapter starts with a detailed description of minor losses for both steady and oscillating flows. After that, mathematical expressions describing steady flow minor loss coefficients at T-Junctions are presented and the difficulties regarding the application of these empirical expressions are discussed.

4.1 Minor Losses in Oscillating Flows

Along with viscosity related pressure drops, internal steady flows exhibit additional pressure losses associated with the geometry changes in the flow path. These losses are called the *minor losses*.

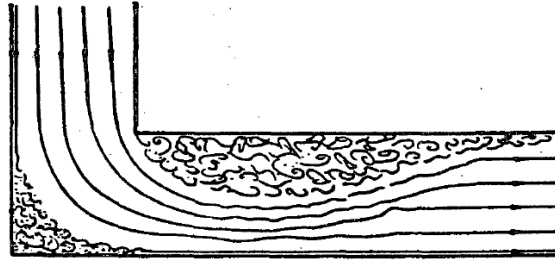


Figure 4.1: Vortices created in a 90°elbow, causing minor losses [26].

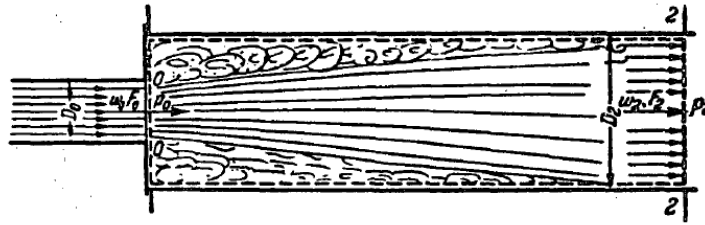


Figure 4.2: Vortices caused by sudden expansion in a flow path [26].

Figures 4.1 and 4.2 show the formation of turbulent vortices at a right angle elbow and during a sudden expansion for a steady flow. This irreversible characteristic of the turbulent flow pressure difference across any geometrical feature is expressed using the minor loss coefficient K [14, pp. 183-184].

$$\Delta p = K \frac{1}{2} \rho u^2 = K \frac{\rho U^2}{2A_c^2} \quad (4.1)$$

For steady flows, this coefficient is a constant given as a function of geometry and the Reynolds number. The majority of these coefficients are provided for specific ranges of Reynolds numbers, therefore, knowing the geometrical feature on its own allows for obtaining the coefficient for the given range. Note that for a steady flow, Equation 4.1 is an addition to the dissipationless Bernoulli pressure difference $\Delta p = \Delta(\rho u^2/2)$ and because it is conveniently known to describe a loss, the minus sign is dropped. For oscillating flows however, the sign of the flow direction requires more careful notation,

therefore for the rest of this work, U is taken to be positive in the positive \hat{x} direction and p is taken to be positive when it increases along the positive \hat{x} direction.

The amount of research regarding minor loss coefficients for oscillating flows is very limited. One solution to this problem is to use the steady flow coefficients given that the gas displacement amplitude is much larger than any of the dimensions in the vicinity. This condition ensures that the Iguchi's hypothesis is applicable which simply states that flow at each instant of time should be identical to that of fully developed steady flow with the same velocity. Details of this hypothesis can be found in Appendix B.3. This assumption also allows for the flow to be fully developed so that the losses associated with the entry effects are ignored. Sufficiently large displacement amplitudes mean that the flow is fully turbulent. The assumption that the flow is fully turbulent at all times becomes particularly important because the steady flow minor loss coefficients are constant values for high Reynolds number flows in most cases [26]. Therefore, assuming that the flow is always turbulent allows for the steady flow minor loss coefficient to be applicable in oscillating flow conditions.

If the minor loss coefficient is not a function of flow velocity, replacing U with $|U_1| \sin \omega t$ in Equation 4.1 and time averaging would provide a time averaged pressure drop across the geometric feature.

$$\Delta p(t) = -\frac{K}{2A_c^2} \rho(t) |U_1| U_1 \quad (4.2)$$

Note that for asymmetrical geometries, there are two K values which are applicable in 2 different halves of the period. For instance, an oscillating flow in Figure 4.2 would experience sudden expansion in the first half of the period and sudden contraction on the other half, each represented with a different K value. These two conditions are represented by K_+ , for a flow moving in the positive \hat{x} direction while expanding and K_- in the negative \hat{x} direction while contracting. Considering the sinusoidal velocity and time-averaging for an asymmetrical flow condition with K_+ and K_- gives:

$$\begin{aligned} \overline{\Delta p_{minor}} &= -\frac{\omega}{2\pi A_c^2} \left(\int_0^{\pi/\omega} K_+ \frac{1}{2} \rho_m |U_1|^2 \sin^2 \omega t - \int_{\pi/\omega}^{2\pi/\omega} K_- \frac{1}{2} \rho_m |U_1|^2 \sin^2 \omega t \right) \\ &= -\frac{1}{8A_c^2} \rho_m |U_1|^2 (K_+ - K_-) \end{aligned} \quad (4.3)$$

where A_c represents the smallest cross sectional area of the feature. It should be noted that along with the minor loss coefficient K , Equation 4.3 assumes the density ρ is also a constant. Equation 4.3 is only applicable to purely sinusoidal flows, hence, a modification is required to account for the superposed steady flow which would occur in the SCL.

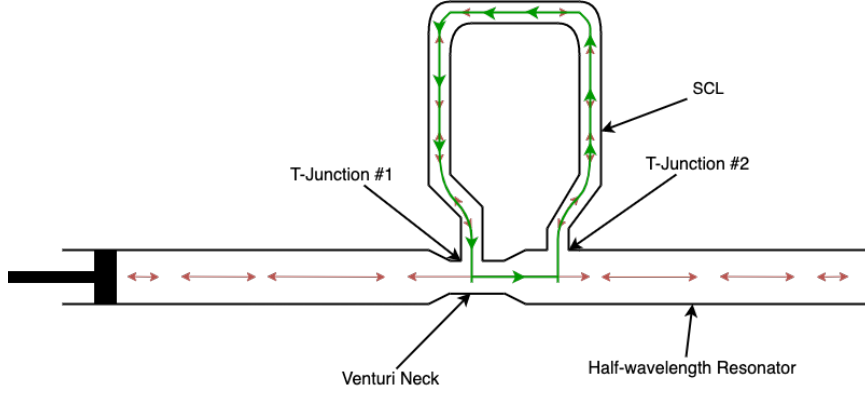


Figure 4.3: Oscillating and steady flows in the Venturi SCL represented with red and green arrows respectively. The SCL loop might include features such as compliance volumes or inertance tubes to adjust the phase of the acoustic flow in the SCL. This figure depicts a simplified loop.

Rewriting Equation 4.3 to include the steady flow yields.

$$\begin{aligned}
 \delta p &= -\frac{\omega}{2\pi} \oint_0^{2\pi/\omega} \delta p(t) dt \\
 &= -\frac{\omega}{2\pi A_c^2} \left[\int_0^{\pi/\omega} K_+ \frac{1}{2} \rho_m \left(|U_1| \sin \omega t + \frac{\dot{M}}{\rho_m} \right)^2 dt \right. \\
 &\quad \left. - \int_{\pi/\omega}^{2\pi/\omega} K_- \frac{1}{2} \rho_m \left(|U_1| \sin \omega t + \frac{\dot{M}}{\rho_m} \right)^2 dt \right] \quad (4.4)
 \end{aligned}$$

where \dot{M} denotes the magnitude of the steady volumetric flow rate.

Depending on the magnitude of these two flows in the SCL, flow direction may or may not change. If the magnitude of the steady flow is larger than the magnitude of the oscillating flow, the flow velocity never reaches zero, hence in that case, one of the minor loss coefficients is redundant because the flow is unidirectional. Defining a parameter, ψ , for the ratio of steady volumetric flow rate to oscillating volumetric flow rate gives three variations of Equation 4.4 when the integrals are performed.

$$\psi = \frac{\dot{M}/\rho_m}{|U_1|} \quad (4.5)$$

$$\delta p = -K_- \left(\frac{\dot{M}^2}{2\rho_m A_c^2} + \frac{\rho_m |U_1|^2}{4A_c^2} \right) \quad \text{for } \psi \leq -1 \quad (4.6)$$

$$\delta p = K_+ \left(\frac{\dot{M}^2}{2\rho_m A_c^2} + \frac{\rho_m |U_1|^2}{4A_c^2} \right) \quad \text{for } \psi \geq 1 \quad (4.7)$$

$$\begin{aligned} \delta p &= \frac{\rho_m |U_1|^2}{8A_c^2} (K_+ - K_-) \left\{ 1 + 2\psi^2 + \frac{K_+ - K_-}{K_+ - K_-} \frac{2}{\pi} \right. \\ &\times \left. \left[(1 + 2\psi^2) \sin^{-1} \psi + 3\psi \sqrt{1 - \psi^2} \right] \right\} \quad \text{for } |\psi| \leq 1 \end{aligned} \quad (4.8)$$

In Equations 4.4 to 4.8, the sign convention is chosen so that the positive δp discourages positive \dot{M} . A negative pressure gradient in \hat{x} direction encourages flow in positive \hat{x} direction. K_+ represents the minor loss coefficient for a flow in the positive \hat{x} direction.

4.2 Converging and Diverging T-Junction Flow Minor Losses

Idelchik's *Handbook of Hydraulic Resistance* provides steady flow minor loss coefficients for a large number of cases [26]. This commonly used source provides K values as a function of geometry for different ranges of Reynolds numbers. However, the K values provided for a T-Junction are functions of not only geometry, but also the branch to trunk flow ratio. Since the flow ratio constantly changes in oscillating flows, time-averaging K values is required to obtain effective coefficients to be used as constants.

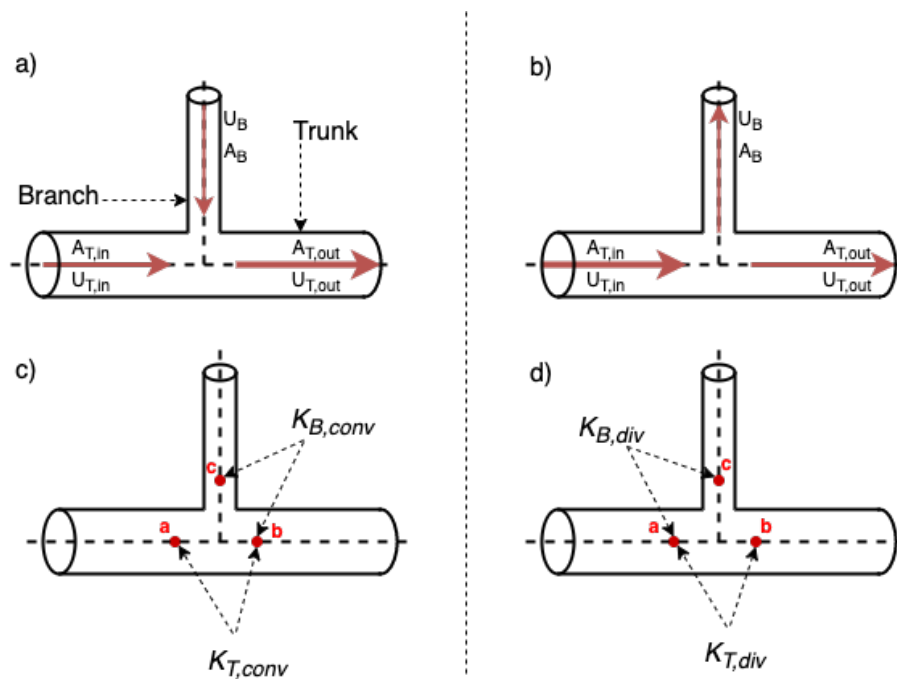


Figure 4.4: a) Flow in a converging T-Junction. b) Flow in a diverging T-Junction. c) and d) Locations of pressure readings for respective minor loss coefficients. The labeled K variables represent the pressure differential, Δp , between the points they indicate.

Figure 4.4 shows the converging and diverging flows in a T-Junction with subscripts B and T denoting branch and trunk respectively. There are two K values associated with a flow in a T-Junction: K_B and K_T , representing minor losses at the branch and the trunk respectively. In order to understand how these K values describe geometry related the pressure differential, it is convenient to consider Equation 4.1 with Figure 4.4. Consider the converging flow case shown in Figure 4.4(a) and (c). For a flow moving in the positive \hat{x} direction, pressure at point a is greater than pressure at point b , hence $\Delta p = p_b - p_a$ is a negative value. With a positive K value, Equation 4.1 provides a positive Δp which causes $p_b - p_a$ to be a less negative value, hindering the pressure difference between these two points that drives the flow.

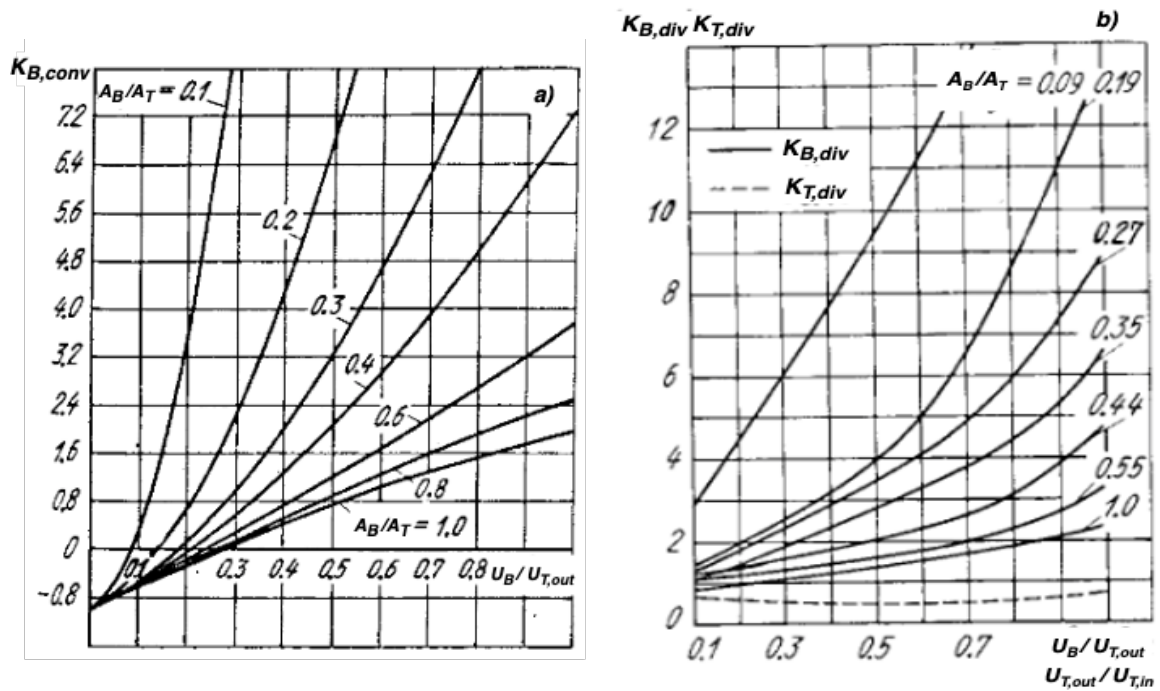


Figure 4.5: (a) K_B values for a converging T-Junction flow. Curves represent branch to trunk area ratios. The horizontal axis is the branch to trunk volumetric flow ratio. (b) Solid lines represent the K_B values for a diverging T-Junction flow with various area ratios. The dashed curve represents the trunk loss coefficient, K_T , for the diverging flow case. The horizontal axis for K_T is the ratio of trunk inlet to trunk outlet volumetric flow rates. Adapted from [26].

Figure 4.5(a) shows the branch minor loss coefficients at a T-Junction for a converging flow. Note that for all branch to trunk area ratios, the corresponding branch minor loss coefficient approaches -1 as the flow ratio approaches 0. Since the definition of a minor loss coefficient is $K = \frac{\Delta p}{\rho_m u^2/2}$, the -1.00 value for the coefficient corresponds exactly to the steady flow Bernoulli pressure. Hence, at lower ratio converging flows, the T-Junction creates a suction into the trunk. For the case of a diverging flow as shown in Figure 4.5(b), the K_B values are always positive. Compared to the converging flow diagram, the minor loss coefficient approaches +1 instead of -1 as the flow ratio approaches 0. This creates a discontinuity in the instantaneous K_B value experienced by the flow if the flow in the branch changes direction. This abrupt jump from -1 to +1 is physically not possible, hence how the branch minor loss coefficient actually behaves when the branch flow change direction requires further experimental studies.

Rennels et al. provides semi-empirical expressions for branch and trunk minor loss coefficients for both converging and diverging cases that agree with both Idelchik's

and a number of more recent studies investigating the minor loss coefficients at a T-Junction [27]. According to Rennels et al., the converging flow branch loss coefficient is given by:

$$K_{B,conv} = -0.92 + 2(2 - C_x - C_M) \frac{U_B}{U_{T,out}} + \left[(2C_y - 1) \left(\frac{A_B}{A_{T,out}} \right)^2 + 2(C_x - 1) \right] \left(\frac{U_B}{U_{T,out}} \right)^2 \quad (4.9)$$

where,

$$C_x = 0.08 + 0.56 \frac{r}{d_B} - 1.75 \left(\frac{r}{d_B} \right)^2 + 1.83 \left(\frac{r}{d_B} \right)^3 \quad (4.10)$$

$$C_y = 1 - 0.25 \left(\frac{d_B}{d_{T,out}} \right)^{1.3} - \left[0.11 \left(\frac{r}{d_B} \right) - 0.65 \left(\frac{r}{d_B} \right)^2 + 0.83 \left(\frac{r}{d_B} \right)^3 \right] \left(\frac{d_B}{d_{T,out}} \right)^2 \quad (4.11)$$

$$C_M = 0.23 + 1.46 \frac{r}{d_B} - 2.75 \left(\frac{r}{d_B} \right)^2 + 1.65 \left(\frac{r}{d_B} \right)^3 \quad (4.12)$$

where r is the radius at the connection of branch to the trunk, d_B and $d_{T,out}$ represent the branch and trunk diameters respectively. Note that for the purposes of this work, it is assumed that the connection of branch to trunk is a sharp corner with $r = 0$, which simplifies above constants to 0.08, 1 and 0.23 respectively. For the converging flow, the trunk minor loss coefficient is given by:

$$K_{T,conv} = 1 - 0.95 \left(\frac{U_{T,in}}{U_{T,out}} \right)^2 - 2C_x \left[\left(\frac{U_{T,in}}{U_{T,out}} \right) - \left(\frac{U_{T,in}}{U_{T,out}} \right)^2 \right] - 2C_M \left[1 - \left(\frac{U_{T,in}}{U_{T,out}} \right) \right] \quad (4.13)$$

The diverging flow branch minor loss coefficient is given by:

$$K_{B,div} = 1 - 1.13 \left(\frac{U_B}{U_{T,in}} \right) + \left[0.81 + \left(1.12 \frac{d_B}{d_{T,in}} - 1.08 \left(\frac{d_B}{d_{T,in}} \right)^3 + C_z \right) \frac{d_{T,in}}{d_B} \right] \left(\frac{U_B}{U_{T,in}} \right)^2 \quad (4.14)$$

where, C_z is:

$$C_z = 0.57 - 1.07 \left(\frac{r}{d_B} \right)^{0.5} - 2.13 \left(\frac{r}{d_B} \right) + 8.24 \left(\frac{r}{d_B} \right)^{3.2} - 8.48 \left(\frac{r}{d_B} \right)^2 + 2.90 \left(\frac{r}{d_B} \right)^{5/2} \quad (4.15)$$

The diverging flow trunk minor loss coefficient is given by:

$$K_{T,div} = 0.36 - 0.98 \left(\frac{U_{T,out}}{U_{T,in}} \right) + 0.62 \left(\frac{U_{T,out}}{U_{T,in}} \right)^2 + 0.03 \left(\frac{U_{T,out}}{U_{T,in}} \right)^8 \quad (4.16)$$

In order to include the effects of these minor loss coefficients for a time-averaged variable, the coefficients themselves also need to be time-averaged. A sample of this iterative process for one Venturi size using an acoustic simulation software is presented in Section 5.2. The time-averaged K values for different Venturi sizes are presented in Section 5.3. The time-averaged minor loss coefficients for the expansion and the contraction of the flow as it goes through the Venturi have recently been studied [28]. A summary of this work is provided in Appendix C. The curves and bends in the SCL is assumed to be very smooth hence minor losses for these features are omitted in the simulations.

Along with the minor loss coefficients, oscillating flows experience viscous resistance and thermal-relaxation losses as well. These irreversibilities are relatively simple to derive from fundamental equations when Rott's acoustic approximations are applicable. For turbulent acoustic flows, Iguchi's hypothesis provides relatively accurate approximations. These three types of losses with mathematical derivations are presented in detail in Appendix B. Combined with these three acoustic irreversibilities, the time-averaged minor loss coefficients account for almost all the losses in a thermoacoustic system. However, it should be noted that real world applications of thermoacoustics suffer from numerous types of other irreversibilities as well. The non-

zero temperature gradients along the direction of oscillations, the assumption that the wall temperature stays constant as the oscillations occur, the energy radiated to the ambient as either audible or non-audible pressure waves and the vibration losses delivered to the structure holding the assembly through its anchors are all contributors to the overall losses. The reasons for divergence between the numerical models, and the real world applications will be discussed in Chapter 6 in detail. The next chapter presents the DeltaEC results for a Venturi-SCL device along with a method for determining the time-averaged minor loss coefficients at a T-Junction.

Chapter 5

DeltaEC Simulations

This chapter investigates the effects of varying Venturi sizes on the magnitude of steady flow in the SCL. The studies presented are performed using the thermoacoustic simulation software DeltaEC. DeltaEC is a numerical integration tool that uses one-dimensional wave equations to allow users obtain solutions for a user-defined geometry in a user-selected working fluid. It can handle complex geometric configurations and acoustic elements such as resonators, duct networks, and complete thermoacoustic engines and electro-acoustically driven thermoacoustic refrigerators. This chapter starts with presenting the DeltaEC simulation results on the acoustic radiation pressure, $p_{2,0}$, when a Venturi with varying dimensions is placed at the velocity node of a half-wavelength resonator. Then, Section 5.2 describes the iterative process that is used to determine the time-averaged minor loss coefficients at a T-junction using the steady flow expressions provided in Chapter 4. The last second section builds onto the Venturi-resonator simulations with the addition of the SCL and the time-averaged minor loss coefficients.

Acoustic simulations in this chapter are completed using DeltaEC's currently available version 6.4b2.7 which was released in late 2017. Data collected for varying Venturi sizes were exported, manipulated and graphed using MATLAB R2018b and MS Excel 2020.

5.1 ARP in a Resonator with Varying Venturi Geometry

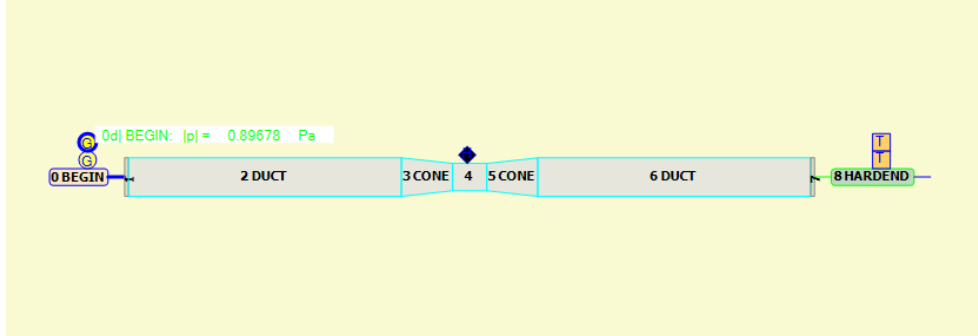


Figure 5.1: DeltaEC diagram of a half-wavelength resonator with a Venturi at the pressure node.

This section presents DeltaEC simulation results that investigates the effects of placing a Venturi at the pressure node of a half-wavelength resonator. Figure 5.1 shows the DeltaEC diagram used for the simulations in this section. The sample code used to create the simulations can be found in Appendix D.

Resonator length	1 m	Venturi Neck Length	5 cm
Taper Length	7.5 cm	Piston Disp.	5×10^{-4} m ³ /s
Temperature	298 °K	Pressure	120 KPa
Fluid	He	Flow Type	Laminar
Resonator A_c	2.5×10^{-3} m ²	Min. Venturi A_c	1.25×10^{-3}
Solver	Runge-Kutta	Node Size	100

Table 5.1: Assumed Parameters for properties of a half-wavelength resonator with a Venturi.

Table 5.1 summarizes the parameters used for the half-wavelength resonator simulations where the work is given to the system via a sealed piston with constant displacement regardless of the Venturi size. Note that in this set up, the work is given to run the SCL, however, for a heat carrying SCL, the work would be extracted at the piston with some portion of the heat carried by the SCL being used to drive the SCL. In both scenarios however, the factors driving the SCL would be nearly unchanged except for the effects of a mean temperature gradient which was introduced in Section 2.5.

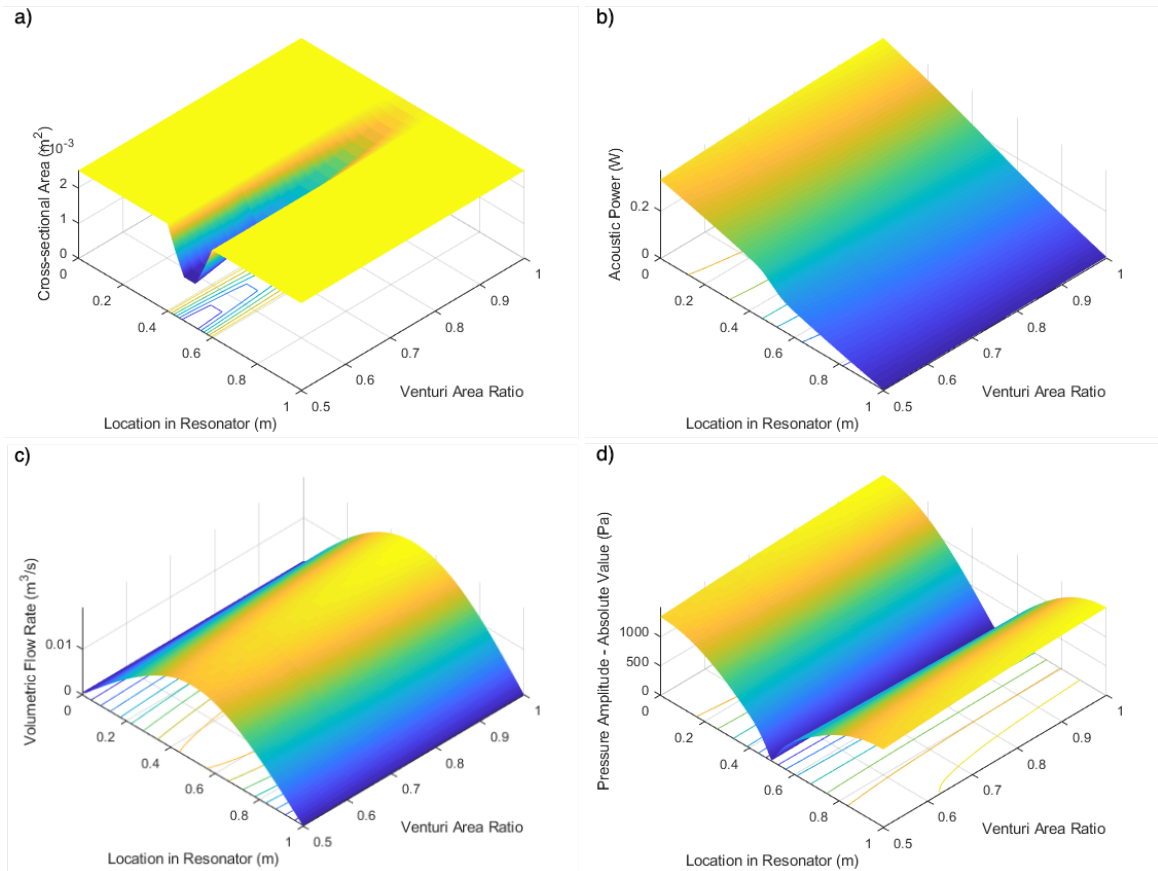


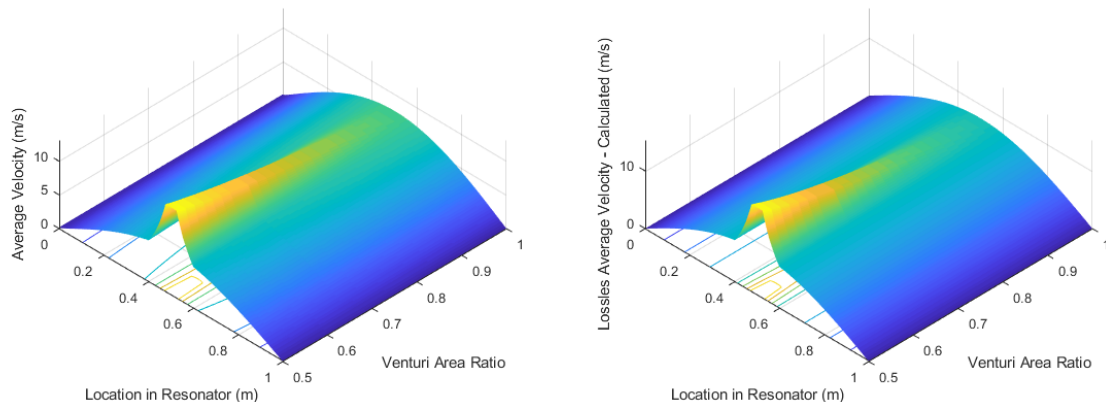
Figure 5.2: A_c , $\dot{E}_{2,0}$, $|U_1|$, $|p_1|$ values for a 1 meter-long half-wavelength resonator with varying Venturi sizes and constant piston displacement amplitude.

Figure 5.2 presents the simulation results for the resonator shown in Figure 5.1 with parameters listed in Table 5.1. For all variables, ratio of Venturi cross-sectional area to resonator cross-sectional area varied between 0.5 and 1. Figure 5.2 presents varying A_c , $\dot{E}_{2,0}$, $|U_1|$, $|p_1|$ values in the resonator as a function of location and cross-sectional area ratio of the Venturi. Figure 5.2(a) shows the change in cross-sectional area available to the gas inside the resonator. Figure 5.2(b) shows the acoustic power distribution, $\dot{E}_{2,0}$, in the \hat{x} direction. The power delivered by the piston at the 0^{th} meter (piston face) dissipates linearly for a straight resonator. As the Venturi neck diameter gets smaller, the rate at which the acoustic power is dissipated per unit length in the Venturi increases. This behaviour is expected due to the quadratic relationship between viscous dissipation and velocity. In other words, viscous losses increase with the square of fluid velocity, hence, the faster the fluid moves at the neck, the more energy is lost to friction. For one complete period of oscillation, the area under the curves of the $\dot{E}_{2,0}$ graph along the *Location in Resonator* direction would

give the total energy of the oscillating gas inside the resonator. Due to increased viscous losses, the area under these curves get smaller as the Venturi size decreases. In Figures 5.2(c) and (d), this total energy loss manifests itself as drops in both the volumetric flow rate (kinetic energy) and the pressure oscillation magnitudes (potential energy). Although the spatially averaged velocity increases as the Venturi size decreases, the magnitude of volumetric flow rate at the pressure node decreases due to the increased viscous losses. Figure 5.2(d) for p_1 shows a slight decrease at the resonator ends due to the drop in the total potential energy with decreasing Venturi sizes.

In Section 3.3, an expression for a lossless velocity profile in the resonator was provided with Equation 3.5.

$$u_1(x) = \frac{P}{\rho_m c_o} \sin(kx) \frac{A_0}{A(x)} = \frac{P}{\rho_m c_o} \sin(kx) \left(\frac{D_0}{D(x)} \right)^2 \quad (3.5)$$

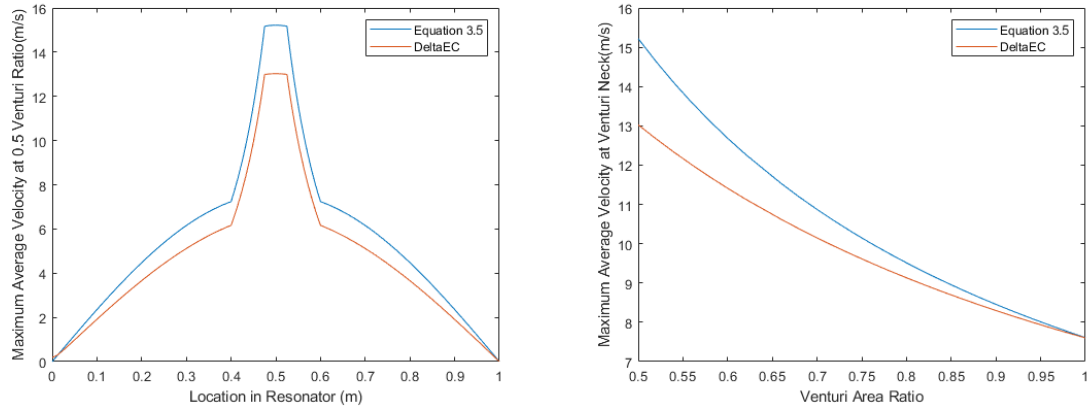


(a) Spatially averaged velocity, $|u_1|$, with varying Venturi sizes simulated in DeltaEC. (b) Spatially averaged velocity, $|u_1|$, with varying Venturi sizes generated using Equation 3.5.

Figure 5.3: Comparison of average flow velocity, $|u_1|$, profiles with varying Venturi sizes (DeltaEC simulated vs. Lossless Equation 3.5).

Figure 5.3 shows the lossless and simulated velocity magnitude profiles in the resonator with varying Venturi sizes. In order to examine how the Venturi ratio changes the velocity profile in the lossless case, a baseline profile without area change is required. To produce this profile, Equation 3.5 requires an input which is the maximum pressure amplitude, P . This constant denotes the maximum pressure amplitude experienced at the cylinder ends. This value is obtained from the DeltaEC's straight resonator simulation, hence, the velocity profile curves at Venturi Area Ratio equal

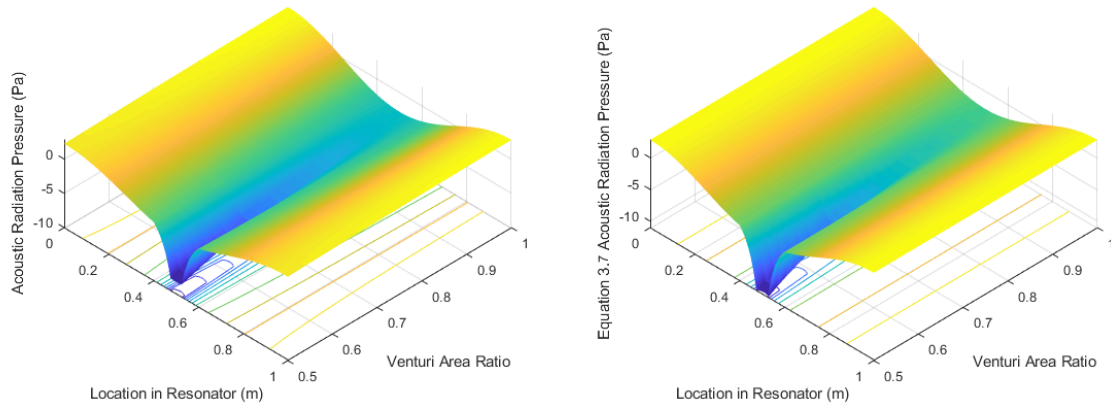
to 1 in Figure 5.3a and 5.3b are identical.



(a) Comparison of $|u_1|$ values. Simulated vs. calculated (b) Comparison of $|u_1|$ values at the pressure node (Venturi results (Equation 3.5 for a Venturi area ratio of 0.5. neck) for varying Venturi sizes.

Figure 5.4: $|u_1|$ comparison of DeltaEC simulations and Equation 3.5.

It is difficult to see the difference in velocity profiles in Figure 5.3 since the difference is small compared to the magnitudes. Figure 5.4a shows the velocity profiles for the Venturi area ratio of 0.5 whereas Figure 5.4b shows the velocity differences at the Venturi neck for varying sizes. Note that as the Venturi size decreases, the gap between the simulations and the profile created by lossless expression increases quadratically. The derivation of Equation 3.5 is based on the Bernoulli's equation as it is in the steady flow case. The assumption states that due to conservation of mass and incompressibility of the fluid, the volume flow rate going through an area change would stay constant regardless of the cross sectional area. The lossless equation assumes that regardless of the Venturi neck diameter, the amount of fluid flux through the neck would stay constant. However, the $|U_1|$ graph in Figure 5.2 showed that the volumetric flow rate does not stay constant, but is affected by the increased amount of viscous losses. This variation in $|U_1|$ is the reason behind the divergence of the velocity curves in Figure 5.4a and 5.4b.



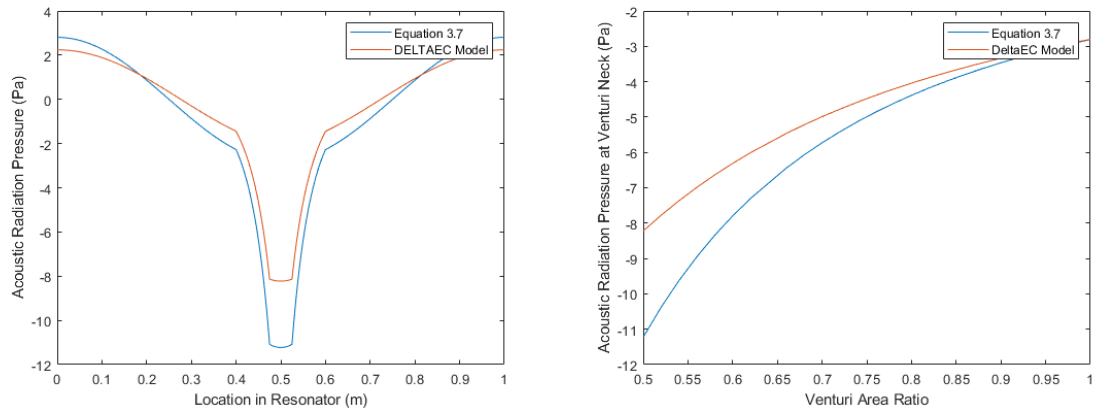
(a) DeltaEC values for $p_{2,0}$ with varying Venturi sizes. (b) $p_{2,0}$ values for varying Venturi sizes using Equation 3.7.

Figure 5.5: Comparison of $p_{2,0}$ values obtained from DeltaEC and Equation 3.7 for varying Venturi sizes.

Using the lossless velocity equation, an expression for $p_{2,0}$ was also presented in Section 3.3.

$$p_{2,0}(x) = -\frac{P^2}{2\rho_m c_o^2} \left(\frac{D_0}{D(x)} \right)^4 \sin^2(kx) + \frac{P^2}{4\rho_m c_o^2} \left(\frac{D_0}{D(x)} \right)^4 + \text{constant} \quad (3.7)$$

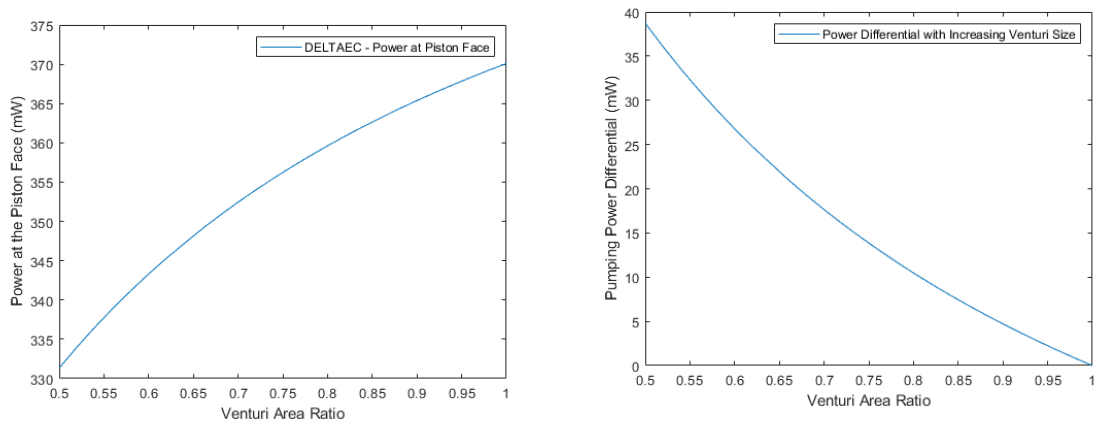
Figure 5.5 compares the $p_{2,0}$ values in a similar fashion to the case of $|u_1|$. Looking at the values at resonator ends, the DeltaEC results show a decrease at these locations due to the pressure amplitude drop. Since $p_{2,0}$ is defined as the difference between the potential and kinetic energy densities, and since the flow velocity is zero at these locations, $p_{2,0}$ at the ends is simply equal to the potential energy density. Note that in the lossless case, $p_{2,0}$ at the ends stays constant. At the Venturi neck, the potential energy density is zero, hence what the graphs show is the kinetic energy density multiplied by -1. Here, the simulated results show that $p_{2,0}$ at the neck is not as negative as the lossless case, due to slower flow as explained in the previous paragraph.



(a) Comparison of $p_{2,0}$ values. Simulated vs. calculated results (Equation 3.7 for a Venturi area ratio of 0.5. (b) Comparison of $p_{2,0}$ values at the pressure node (Venturi neck) for varying Venturi sizes.

Figure 5.6: $p_{2,0}$ comparison of DeltaEC simulations and Equation 3.7.

Figure 5.6a shows that for a Venturi cross-sectional area of 0.5, an imaginary SCL connected to 0.5 m and 0.6 m of the resonator would experience a pressure difference of 9.2 Pa in the lossless case whereas the DeltaEC model for the same case shows 6.9 Pa of pressure difference.



(a) Acoustic power at the piston with varying Venturi sizes. (b) Change in piston power as a function of the Venturi size.

Figure 5.7: Acoustic power loss experienced at the piston face with varying Venturi sizes.

The power required to create this pressure differential is shown in Figure 5.7. Figure 5.7a shows that for a straight resonator, the acoustic power experienced at the piston would be around 370 mW. This is the amount of power lost to create the acoustic radiation pressure in the resonator. For the lossless case, this amount would stay constant since the Venturi size is assumed to not have any effect on the power

loss. However, when the losses caused by the Venturi is taken into account, the power experienced at the piston face falls down to 332 mW. This is the cost of increased $\Delta p_{2,0}$ with the introduction of Venturi to the resonator. Figure 5.7b shows the power differential at the piston for different Venturi sizes.

The simulations in this section showed that the addition of Venturi to the resonator increases the time-averaged pressure differential between the Venturi neck and another location along the resonator. In the next section, the iterative process that is used to obtain time-averaged minor loss coefficients at a T-Junction are presented.

5.2 Time-Averaged Converging and Diverging T-Junction Flow Minor Losses

In order to obtain time-averaged values, instantaneous volumetric flow rates at the branch and the trunk are required to be known so that the instantaneous K values can be obtained. Using DeltaEC with some initial guesses for all 4 K values, $|U_T|$, $|U_B|$ and \dot{M} values at a T-Junction can be determined. Using these amplitudes, Equations 4.9, 4.13, 4.14 and 4.16 can be used to obtain instantaneous values which then can be time-averaged. This process can be repeated iteratively until all values cease to change significantly.

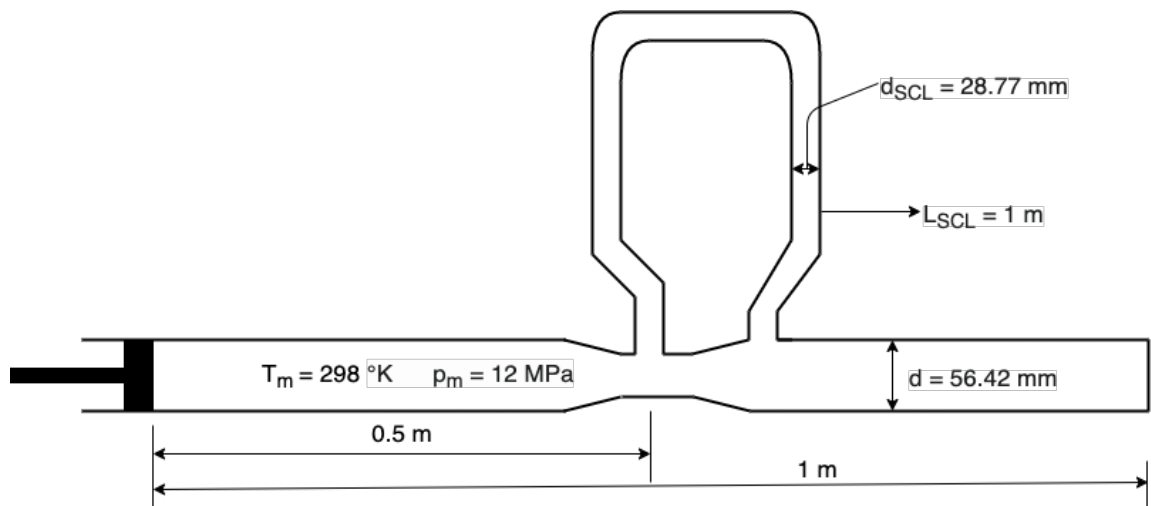


Figure 5.8: Schematic of Venturi-SCL simulation used for obtaining effective K values at a T-Junction.

Resonator length	1 m	SCL Length	1 m
Taper Length	7.5 cm	Venturi Area Ratio	0.7
Temperature	298 °K	Pressure	12 MPa
Piston Disp.	5×10^{-4} m ³ /s	Fluid	He
Resonator A_c	2.5×10^{-3} m ²	SCL A_c	0.65×10^{-3} m ²

Table 5.2: Assumed Parameters for Time-Averaged K Simulations.

Figure 5.8 shows the schematic of the simulation model that is used for obtaining time-averaged K values for a Venturi area ratio of 0.7. Table 5.2 summarizes parameters used in this simulation.

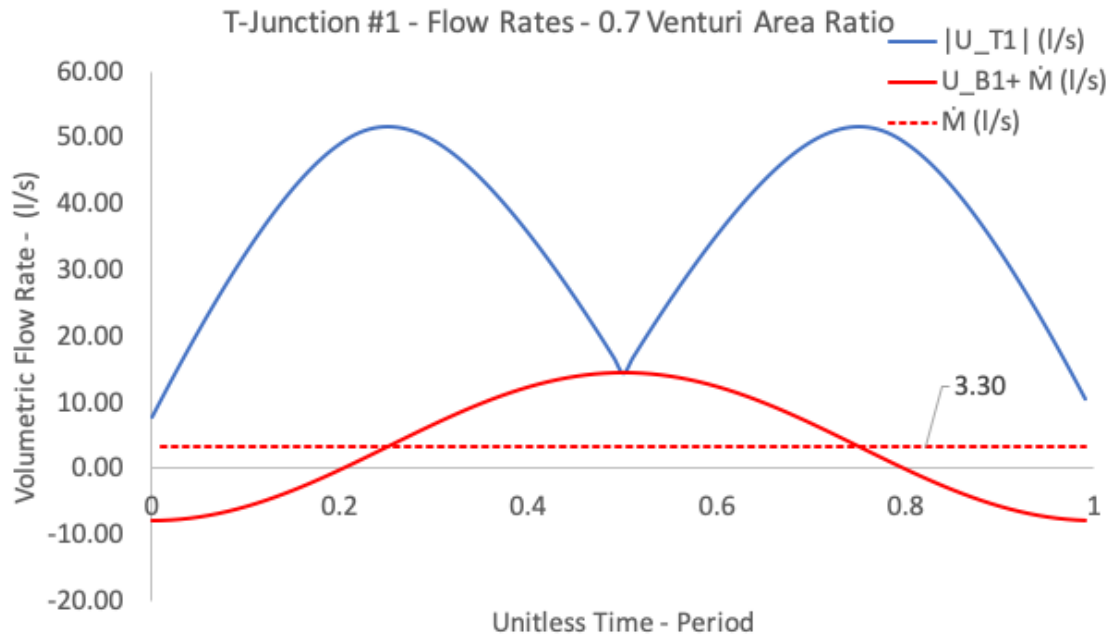


Figure 5.9: Simulated instantaneous branch and trunk flow rates at the T-Junction located at the pressure node with a Venturi area ratio of 0.7.

Figure 5.9 shows instantaneous volumetric flow rates for a period in the T-Junction located at the Venturi neck. Note that the T-Junction #2 is placed right after the converging nozzle towards the close end of the resonator. In order to keep the branch and trunk flows in phase, the length of the branch is set to be equal to the resonator length.

The solid blue line in Figure 5.9 represents the instantaneous trunk volumetric flow rate. The solid red line represents the oscillating branch flow plus the steady

flow rates. The positive \dot{M} line means that the flow is converging into the trunk from the branch. Hence, in Figure 5.9, the flow is only converging for 60% of the period since that is how long the red curve is above the zero line. The instantaneous flow rates from these 2 curves are used to calculate K_B and K_T values at the T-Junction and depending on the flow direction in the branch, converging or diverging sets of equations are used.

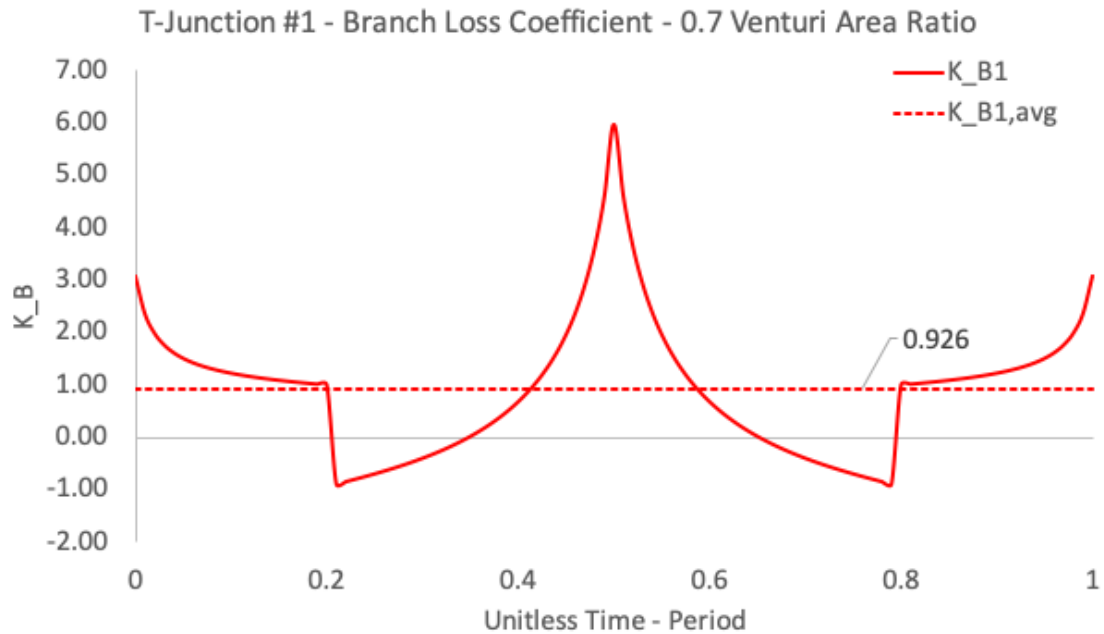


Figure 5.10: Instantaneous and time-averaged K_B at T-Junction #1 with 0.7 area ratio using the volumetric flow rates from Figure 5.9 and Equations 4.9 and 4.14 with respective branch flow direction.

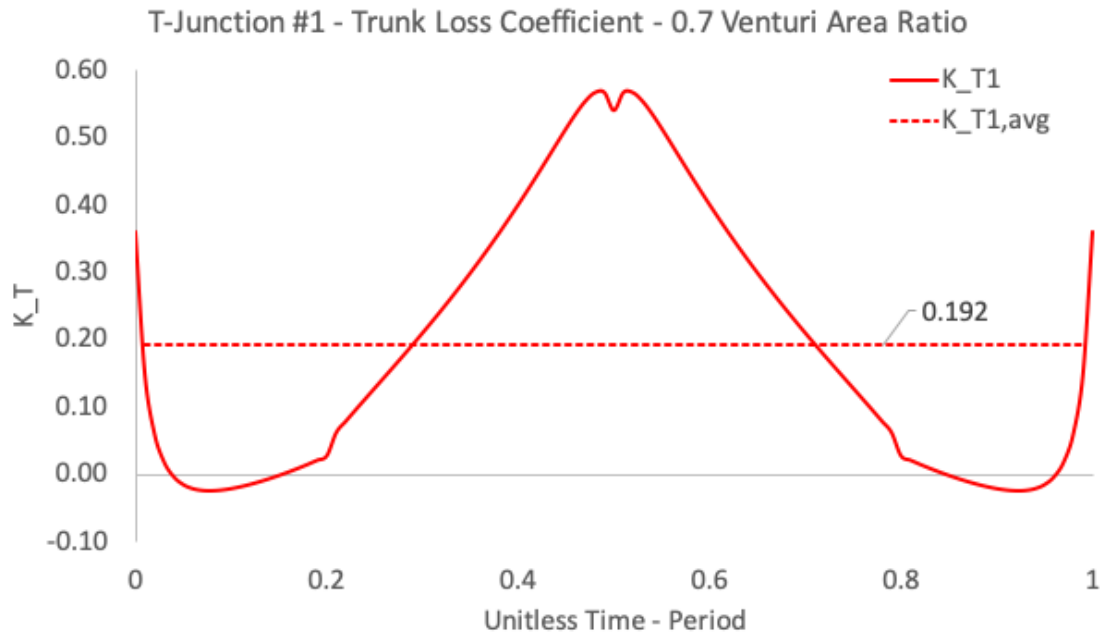


Figure 5.11: Instantaneous and time-averaged K_T at T-Junction #1 with 0.7 area ratio using the volumetric flow rates from Figure 5.9 and Equations 4.13 and 4.16 with respective branch flow direction.

The branch flow in Figure 5.9 changes direction 2 times during the period, at unitless times 0.2 and 0.8. Figure 5.10 shows that the instantaneous K_B values exhibit the discontinuity related to branch flow direction as mentioned earlier. Note that for approximately one third of the time as the flow is converging into the branch, K_B is negative, therefore the T-Junction encourages the mean flow in the SCL. The peak in the resistance is seen as the branch flow increases and as the trunk flow decreases, this self-limiting behaviour cannot be avoided since the oscillating portion of the trunk flow has to come to a full stop before changing direction. At this point, the only flow in the trunk is the flow that converges from the branch, making the branch to trunk flow ratio 1, pushing the K value to its maximum instantaneously. The other peak in the same graph is caused by the same mechanism but this time for a diverging branch flow. There may be a way to “tune” the SCL by adding compliances or inertances which could move the red curve horizontally in Figure 5.9 by causing a phase shift so that the instantaneous K_B could stay negative for longer. On the other hand, the trunk loss coefficients shown in Figure 5.11 do not show abrupt changes when the flow in the branch changes direction however, a similar maximum value behaviour is

observed as the flow ratio approaches 1.

5.3 SCL - Nonzero Mean Flow Simulations

For the SCL simulations, the mean pressure is set to 12 *MPa* which is the operating pressure for Etalim's TA generator which was mentioned in Section 1.2 [12]. For this set of simulations, the flow is set to be turbulent and mass streaming is enabled.

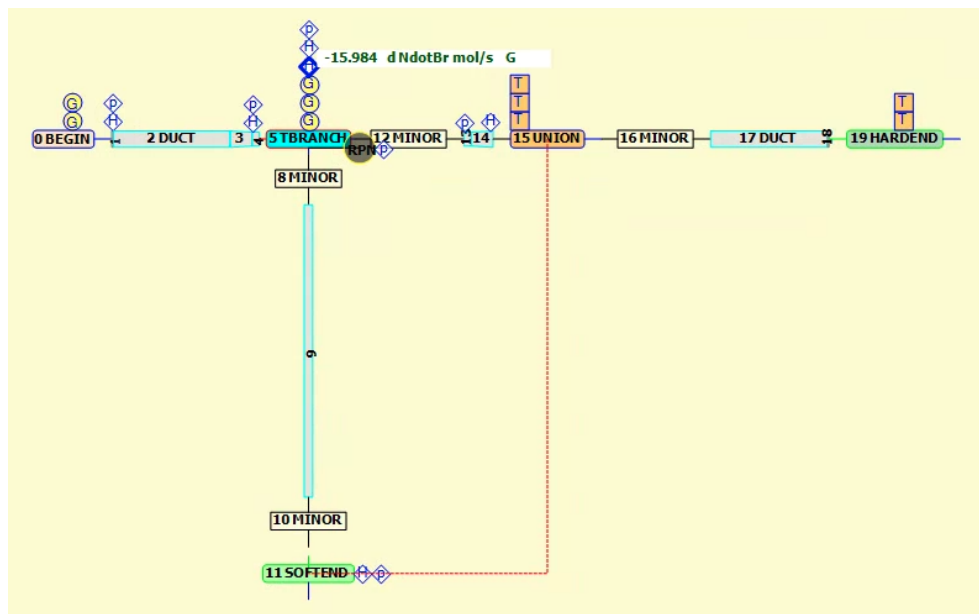


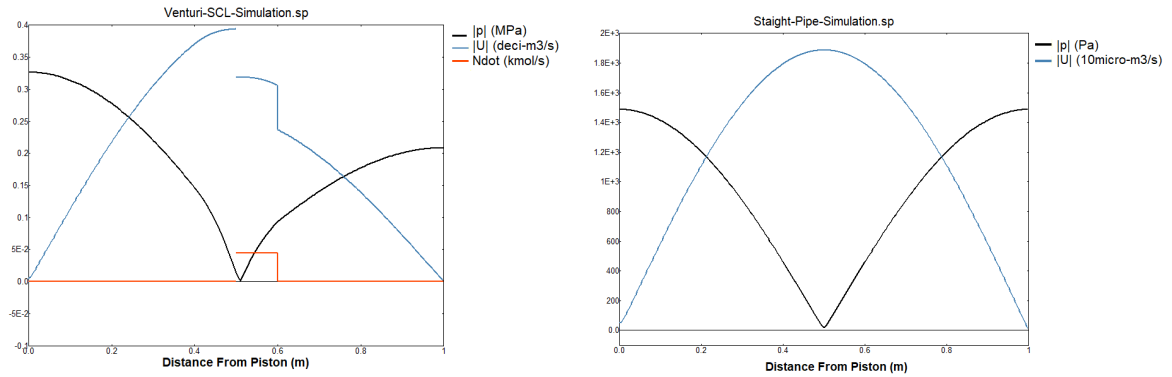
Figure 5.12: DeltaEC diagram of a half-wavelength Venturi-SCL resonator.

When turbulent flow is enabled along with mass streaming, DeltaEC offers an optional parameter that can be set to *Optimistic*, *Normal* or *Pessimistic*. These choices are related to the nonlinear interactions between oscillating and steady flows when they are superimposed, as in the SCL. For simulations presented in this section, the *Normal* option is selected which is the average of the other two options. The details of these choices can be found in Reference [24]. Some further discussion is also provided in Chapter 6.

Resonator length	1 m	SCL Length	1 m
Taper Length	7.5 cm	Venturi Area Ratio	0.5 - 1
Temperature	298 °K	Pressure	12 MPa
Piston Disp.	$5 \times 10^{-4} \text{ m}^3/\text{s}$	Flow Type	Turbulent
Resonator A_c	$2.5 \times 10^{-3} \text{ m}^2$	SCL A_c	$0.65 \times 10^{-3} \text{ m}^2$
Surface Roughness	$5 \mu\text{m}$	Flow Interaction Method	Normal

Table 5.3: Simulation Parameters for Venturi-SCL Simulations with varying Venturi sizes.

Figure 5.12 shows the DeltaEC diagram used for the simulations in this section. The sample code can be found in Appendix D. Table 5.3 summarizes the key parameters of the set of simulations.



(a) $|p_1|$, $|U_1|$ and \dot{N} values along the resonator with Venturi and SCL attached.

(b) $|p_1|$, $|U_1|$ values for a straight resonator.

Figure 5.13: Comparison of pressure and volumetric flow rate amplitudes distributions for Venturi-SCL and a straight resonator.

Figure 5.13 compares the pressure and volumetric flow rates distributions along the resonator when for a Venturi-SCL combination to a straight pipe resonator. The blue lines represent the volumetric flow rates while the black lines represent the volumetric flow rate. The red line in Figure 5.13(a) represent the time-averaged molar flow rate, \dot{N} . The positive \dot{N} values between the two T-Junctions indicate that there is a nonzero time-averaged mass flow between the two connections in the positive \hat{x} direction which justifies a steady CCW flow in the SCL.

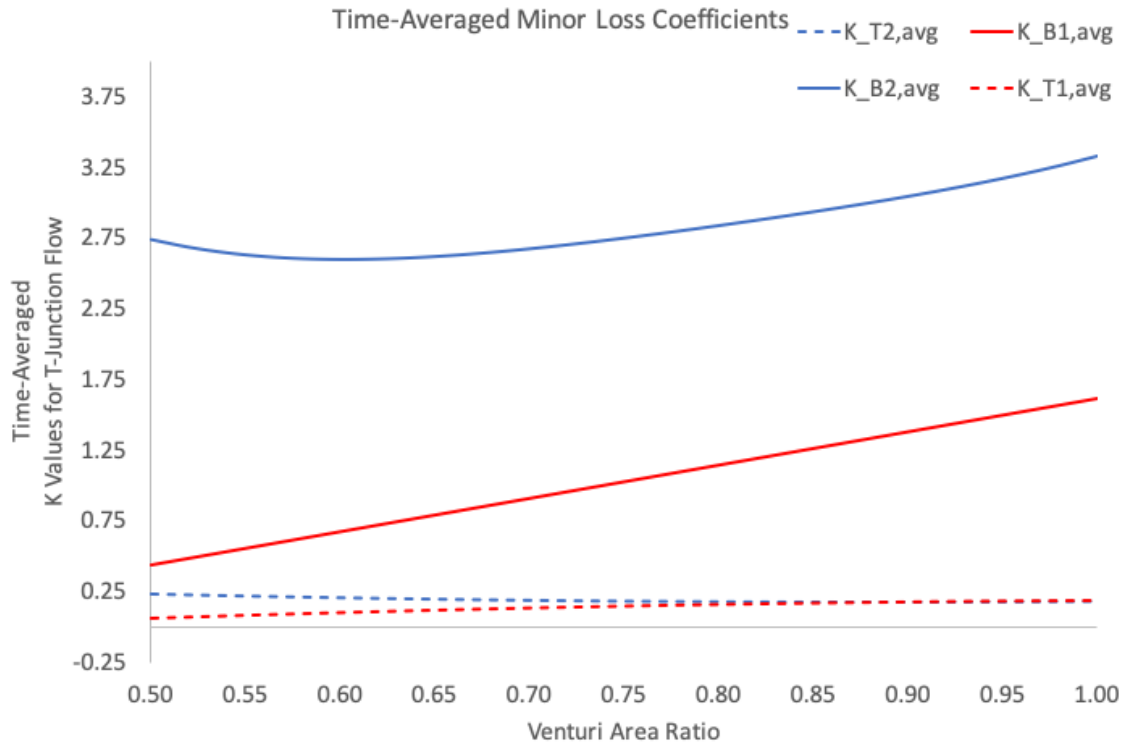


Figure 5.14: Time-averaged minor loss coefficients for 2 T-Junctions.

Figure 5.14 shows the time-averaged K_B and K_T values at both T-Junctions for varying Venturi sizes. These values are obtained using the procedure described in Section 5.2. The solid lines represent the time-averaged branch minor loss coefficients while the dashed line represent the trunk minor loss coefficients. It can be seen that the trunk minor loss coefficients at both junctions stay relatively constant as the Venturi sizes change. The branch minor loss coefficient at the T-Junction #1 decreases linearly while at T-Junction #2, a minimum is reached at around 0.60 area ratio after which an increase is observed. The decrease $K_{B1,avg}$ can be explained by the fact that the increase in the steady flow rate causes converging flow at the junction to take place for longer times, resulting in lower K_B values. As mentioned previously, it might even be possible to achieve a time-averaged negative $|K_B|$ if the SCL is tuned.

The nonlinear behaviour of $K_{B1,avg}$ can be attributed to the fact at the second junction, as the amount of steady flow increases with smaller Venturi sizes, the flow diverges into the branch at an increasing rate. This causes the expression for $K_{B,div}$ from Equation 4.14 to dominate. Figure 4.5 shows that at lower branch to trunk flow

ratios for a branch to trunk diameter ratio of around 0.5, the $K_{B,div}$ drops below +1 before converging to +1 at zero branch flow, creating a minimum. Approximately around 0.60 Venturi area ratio, the effective branch to trunk flow ratio causes $K_{B1,avg}$ to reach a minimum as well.

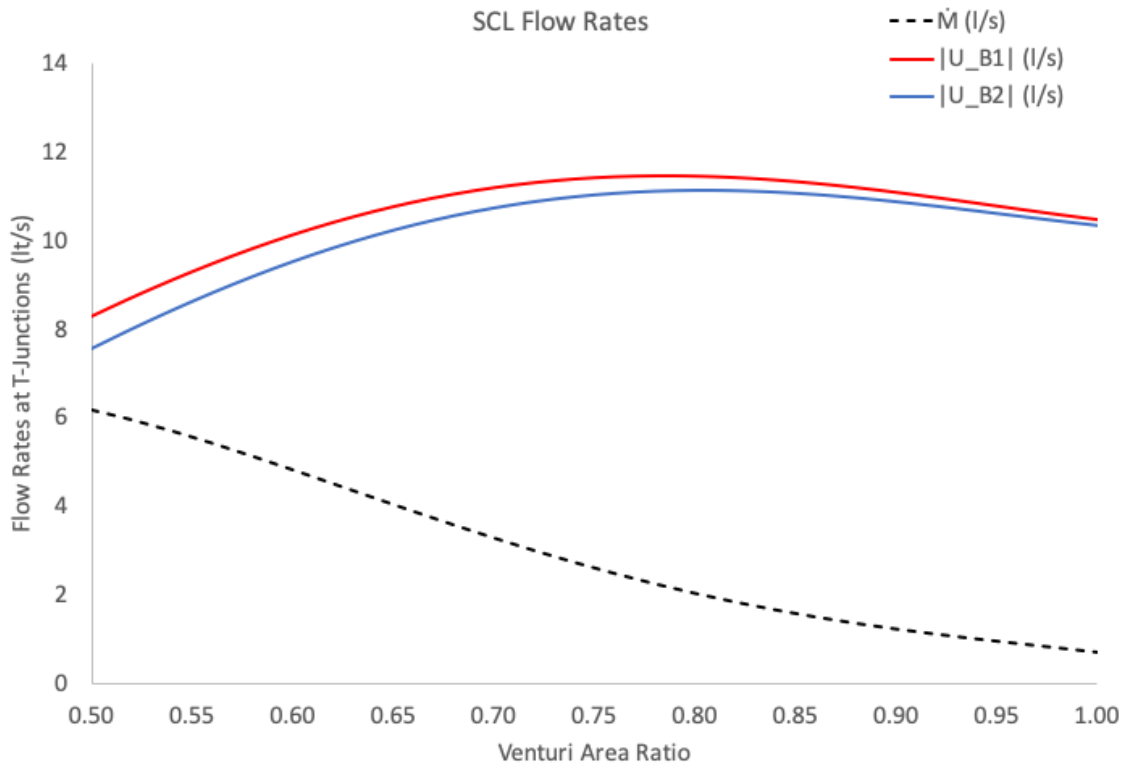


Figure 5.15: Steady and alternating flow rate amplitudes with varying Venturi sizes.

Figure 5.15 shows the amplitudes of alternating branch flow rates both at junctions as well as the steady flow rate, \dot{M} , in the SCL. The divergence between 2 alternating flow amplitudes shown with red and blue curves is caused by increased acoustic attenuation in the SCL as a result of increased steady flow rate. One important observation that is made is the fact that some nonzero steady flow in the SCL exists without the presence of any area change in the resonator. This steady flow with no Venturi in place is purely caused by the spatial variation of the acoustic radiation pressure.

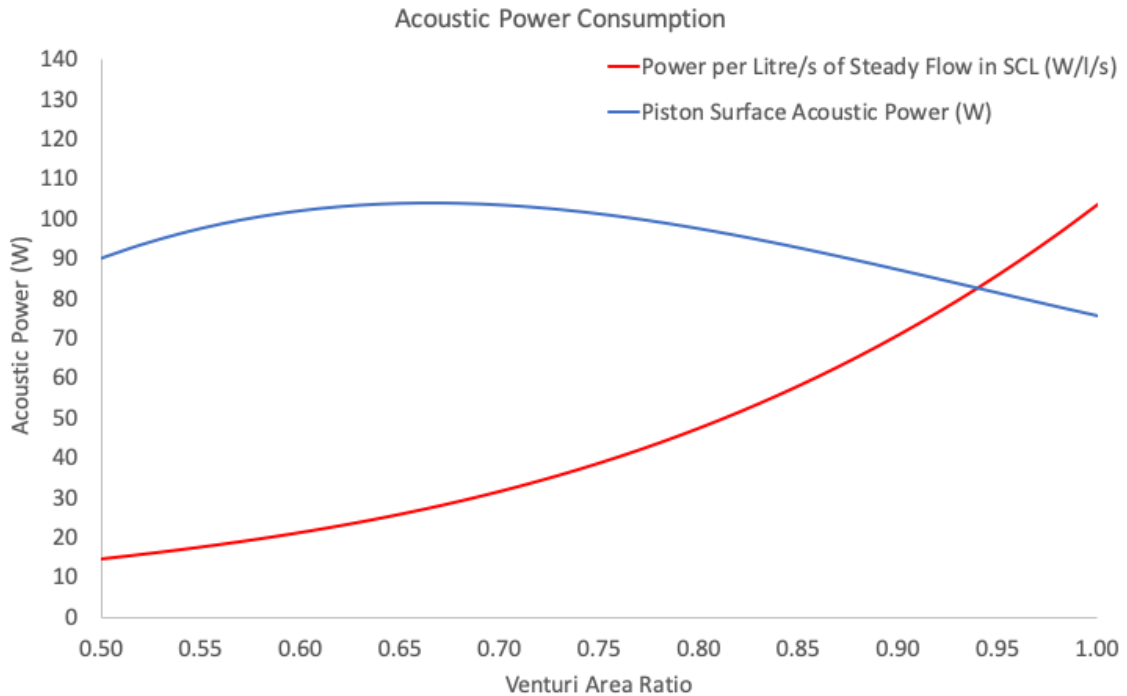


Figure 5.16: Acoustic power experienced at the piston face with varying Venturi sizes.

Figure 5.16 shows that the amount of acoustic power at the piston face keeps increasing up to a certain size of Venturi before starting to decrease around 0.65 area ratio. This behaviour is counter-intuitive since the increased viscous losses due to higher speeds at the neck should cause a drop in this value as explained in Section 5.1. This behaviour can be explained by the fact that the decrease in the $K_{B1,avg}$ and $K_{B2,avg}$ causing larger gains in the acoustic power than the increase caused by the larger losses viscous losses. Since viscous losses increase quadratically with decreasing Venturi size, around 0.65, the viscous losses start to dominate along when combined with the $K_{B2,avg}$ which starts to increase as well. This combination initiates the decreasing trend for the acoustic power curve in Figure 5.16. However, having a maximum for acoustic power does not mean that the system is the most efficient at this size. The red curve in Figure 5.16 shows that the cost of steady flow rate in the SCL decreases with decreasing Venturi size. It should be noted that a minimum for this cost may exist for some other combination of design parameters where the increase in viscous losses start dominating at larger sizes.

This chapter presented the DeltaEC simulation results in 2 sections. The first section investigated the effects of various sizes of Venturi on the acoustic properties

of a half-wavelength resonator. The distribution of the reversible expression for ARP with varying diameter is compared to the simulation results which incorporated irreversibilities. The second section of the chapter presented the simulation results for the time-averaged branch and trunk minor loss coefficients. Then, it was shown that the decreasing Venturi area ratio resulted in higher steady flow rates in the SCL. It was also shown that the placement of a Venturi between 2 T-Junctions could decrease the total losses in the system. Finally, the acoustic power experienced at the piston surface was presented which showed that the combined losses of the system reached a minimum around 0.65 Venturi area ratio. The next chapter discusses the uncertainties in simulation results and reasons for potential divergences when compared to a real life scenario. Additionally, certain characteristics seen in the simulation results are analyzed and explanations are provided for a higher level of understanding.

Chapter 6

Discussion

This chapter presents the discussion of uncertainties in simulation results as well as providing a review of the results provided in Chapter 5. The majority of the uncertainties are related to the assumptions made for calculating the terms used in the simulations such as the irreversibility terms, while the others are factors that are completely omitted in the simulations but might affect the results in a real-life scenario.

The behaviour of acoustic variables including $p_{2,0}$ with varying Venturi sizes in a half-wavelength resonator were presented in Section 5.1. A second set of simulation results with an SCL attached were presented in Section 5.3 and brief explanations for the behaviour of variables as the Venturi sizes varied were provided. Section 6.2 in this chapter expands onto these explanations.

6.1 Uncertainties in Simulation Results

This section discusses the uncertainties related to the assumptions made in calculating some of the terms used in calculations. The irreversibility terms calculated and used by DeltaEC are described in Appendix B in which assumptions made when deriving each term is discussed in detail.

One of these irreversibility terms is called the “Thermal-Relaxation Conductance” [14, pp. 90-94] which DeltaEC incorporates in its calculations. The mathematical derivations for thermal relaxation losses for laminar flows is provided in details in Appendix B.2. Note that, mathematical models are only available for laminar flow conditions due to the lack of research regarding the problem with turbulent

flow conditions. It is known that turbulence disturbs the boundary layer violently which should have effects on the heat transfer properties of the gas. Since the simulations in Chapter 5 allowed for the flow to turn turbulent, the lack of turbulence related factors for this type of irreversibility adds to the uncertainty in the simulation results.

Another source of uncertainty in the simulations finds its roots in the interaction between the turbulent steady flow and the turbulent oscillatory flow in the SCL. Appendix B.3 of this work contains the derivations for the steady turbulent flow pressure drop and the oscillating turbulent flow resistance with the Iguchi's hypothesis. Reference [24] investigates the case, which would take place in the SCL, and provides expressions in their Equation A9 and A10. The authors state that their expression might be an overestimate, hence DeltaEC allows users to chose from 3 options: *Optimistic*, *Normal* and *Pessimistic* as briefly mentioned in Section 5.3. The optimistic option assumes the oscillating and the mean flows are independent, simply superimposed, in this case, Equation B.28, the oscillating turbulent flow resistance, is simply added to the steady flow turbulent resistance. The pessimistic case uses the derivations A9 and A10 from Reference [24], which states that the existence of one type of resistance affects the other type negatively, further increasing the losses. The normal case is the average of the two, which is the recommended option for simulations.

```

|----- 3 -----
|----- 4 -----
|----- 5 -----
TBRANCH Flow splits here
2.3880E+5 a Re(Zb) Pa-s/m^3 G 1.9591E+4 A |p| Pa
1.7305E+6 b Im(Zb) Pa-s/m^3 G -9.9353 B Ph(p) deg
-15.984 d NdotBr mol/s G 1.1215E-2 C |U| m^3/s
-92.078 D Ph(U) deg
679.51 E HtotBr W
15.017 F EdotBr W
73.126 G EdotTr W

|----- 6 -----
|----- 7 -----
|----- 8 -----
|----- 9 -----
|----- 10 -----
|----- 11 -----
SOFTEND
0.0000 a Re(z) 9.6263E+4 A |p| Pa
0.0000 b Im(z) -177.78 B Ph(p) deg
0.0000 c Htot W 1.0778E-2 C |U| m^3/s
86.994 D Ph(U) deg
679.51 E Htot W
-47.216 F Edot W
-2.6835E-2 G Re(z)
0.29361 H Im(z)
298.00 I T K
-111.45 J p20DEC Pa

|----- 12 -----
|----- 13 -----
|----- 14 -----

```

Figure 6.1: Volumetric flow rate phase angles between T-Junction #1 and T-Junction #2.

Along with the uncertainties native to DeltaEC and thermoacoustics in general, there are assumptions made when calculating the time-averaged minor loss coefficients that could have considerable impact on the accuracy of simulation results. For instance, Figure 5.9 shows the branch and trunk flow rates at the first T-Junction and assumes that the branch flow is lagging the trunk flow by -90° . At the other end of the SCL, the flow is assumed to be exactly 180° apart which means if the flow is converging at T-junction #1, then it is diverging at T-Junction #2 simultaneously. Figure 6.1 shows the simulated flow phase angles at the beginning and the end of the loop, at the T-Junctions for a Venturi area ratio of 0.7. There are 2 segments from the simulation code in this figure. Segment 5 refers to the first junction at the Venturi neck where the flow phase should be -90° . Segment 11 shows that the simulated flow phase at this junction is about 87° , resulting in a difference of 179° instead of 180° . This phase difference between the trunk and branch flows would shift the branch flow curve in Figure 5.9 horizontally, modifying the flow rates and instantaneous K values as a result.

Perhaps the most prominent uncertainty in the simulation results come from the discontinuity experienced in the branch minor loss coefficient calculations as the flow in the branch changes direction. Figure 5.10 shows this discontinuity at 2 instants. This sudden change is physically not possible and experimental studies are required

to confirm the exact behaviour of the coefficient for oscillating flows. However, despite causing quantitative divergence, all Venturi sizes considered in this work did exhibit flow reversal in the branch, hence the effects the discontinuity are universal in the results provided. This makes it possible to conclude that the impact of the discontinuity on the variance of the time-averaged values presented in Figure 5.14 is qualitatively minimal. In other words, if the mathematical discontinuity eliminated from the equations, it is expected that the curve in Figure 5.14 would keep its shape but may be shifted up or down since all sized considered had flow reversal in the branch. However, the smooth trend of $K_{B,avg}$ curves would cease to exist, should the branch flow for one of the Venturi sizes did not change direction. This would eliminate the discontinuity's effect and make the instantaneous K values consist of solely either $K_{B,div}$ or $K_{B,conv}$, depending on the T-Junction. If the flow at a junction is always converging, it may even be possible to attain a negative K_B value which would encourage the amount of steady flow in the SCL. Moreover, it should be noted that the current understanding of how minor losses interact with each other when they are in close proximity is very incomplete. Minor losses do affect the flow resistance so they can be used in series with laminar or turbulent viscous resistance loses, however, it is currently unknown if any corrections are required to the compliance, inertance and thermal-relaxation resistance terms if a minor loss present in the vicinity.

For the factors that might cause divergence between the experimental and simulation results, it is possible to mention two types of losses that are omitted. The radiation losses which are lost to the surrounding air and the vibrations absorbed by the fixture through the anchors, two: the losses causes by the entrance effects of the flow.

One observation made while running simulations with different Venturi sizes is the fact that resonance frequency of the system is proportional to the Venturi size. In other words, as the Venturi neck diameter gets smaller, the resonance frequency of the system decreases. This phenomena is explained by the fact that at the velocity node, as the cross-sectional area gets smaller, the path-length that a random fluid particle travels increases. For the oscillations, this manifests itself as an increase in the wavelength which is inversely proportional to the frequency. Note that the frequency drop will affect the total amount of energy stored in the gas, hence negatively affecting the performance. Details regarding this behavior can be found in Reference [25, pp. 855-861].

6.2 Discussion of Results

The first set of simulations in Chapter 5 investigated the behaviour of acoustic variables in a half-wavelength resonator as the diameter of a Venturi placed at the pressure node varied. The results confirmed predictions where the increased average velocity at the Venturi neck with smaller sizes caused viscous losses to increase, reducing the overall energy stored in the resonator. This behaviour is visible in Figure 5.2 with decreasing amplitudes of p_1 and U_1 with smaller Venturi area ratios. However, the exact relationship between Venturi sizes and the energy dissipation is easier to notice in Figure 5.7. This figure shows that with linearly decreasing area ratio, the acoustic power at the piston surface decreases quadratically. The explanation to this behaviour is the fact that viscous losses is a function of squared velocity, hence, while the average velocity at the Venturi neck is linearly and inversely proportional to the area, the viscous losses quadratically and inversely proportional.

The second set of simulations required the calculation of time-averaged minor loss coefficients at T-Junctions so that the amount of steady flow in a loop attached to the resonator could be calculated. Figure 5.14 showed that the time-averaged trunk minor loss coefficients for both junctions stayed relatively invariant while the Venturi size varied. For the T-Junction #1, the branch minor loss coefficient linearly decreased as the Venturi size got smaller. At the T-Junction #2, where flow mostly diverges into the branch, the time-averaged minor loss coefficient also decreased with smaller Venturi sizes until it started increasing again after a threshold, exhibiting a minimum around 0.60 Venturi area ratio. This negative trend of time-averaged branch minor loss coefficients is counter-intuitive, however, it is possible to conclude that the increasing amount of steady flow amplitudes with smaller Venturi sizes cause the instantaneous branch to trunk flow ratios become smaller, which in return results in smaller time-averaged K values. Figure 4.5 shows that lower branch to trunk flow ratios produce lower K values for both converging and diverging cases. Figure 4.5(b) shows that for certain branch to trunk area ratios, the branch minor loss coefficient drops below +1 before converging to +1 at zero branch flow, creating a minimum, therefore presents an explanation to the nonlinear behaviour of the time-averaged branch minor loss coefficient at the T-Junction #2. At the T-Junction #1, the trend of $K_{B1,avg}$ indicate that it may be possible to attain time-averaged branch minor loss coefficient that could encourage the steady flow in the SCL by creating time-averaged suction into the trunk. This is possible because the K values in 4.5(a)

becomes negative for lower branch to trunk flow ratios. However, for Venturi sizes small enough to provide $K_{B1,avg}$ values, the steady flow amplitude, \dot{M} , might grow larger than the branch alternating volumetric flow rate amplitude, $|U_{B1}|$, creating a uni-directional flow in the SCL. In this case, the flow at T-Junction #1 would always converge, eliminating the discontinuity in the instantaneous K values which allowed for a smooth $K_{B1,avg}$ curve in Figure 5.14. The lack of alternating branch flow would result in a sudden drop of the $K_{B1,avg}$ curve which is physically not possible.

The acoustic power curve in Figure 5.16 showed the most unexpected behaviour in simulation results. It was seen that the acoustic power experienced at the piston face increased with the addition of Venturi. As mentioned above, for a resonator without the SCL the acoustic power at the piston surface decreases quadratically as the Venturi size decreases. This increase in the acoustic power as the Venturi size starts to decrease is caused by the drop in the time-averaged branch minor loss coefficients and this drop having a larger impact than the increasing viscous losses. This initial increase in acoustic power eventually stops at a certain Venturi size when the combined increase in viscous losses start dominating the drop in combined minor losses.

In this chapter, uncertainties in the simulation results and the reasons for potential divergence from the experiments were discussed. The results presented in Chapter 5 were examined in detail. The next chapter of the thesis will summarize the results and observations along with presenting recommendations and future work.

Chapter 7

Conclusion and Recommendations

This chapter summarizes the key findings of the study and provides recommendations for both experimental and theoretical studies to be conducted in future. The simulation results showed that the Venturi-SCL combination as an acoustic mass streaming method is a viable alternative to gas-diodes and can be utilized to eliminate hot heat exchangers and high pressure pumps in thermoacoustic devices. The amount of steady flow in the SCL can be controlled by changing the size of the Venturi neck diameter with smaller diameters producing larger magnitude steady flow rates as expected.

The set of simulations with a half-wavelength resonator and a Venturi placed at the pressure node showed that as the Venturi cross-sectional area gets smaller, the amount of viscous losses increase quadratically, which is an expected result since the viscous losses is a function of squared velocity. Due to this increased velocity, the second-order time-averaged pressure, $p_{2,0}$, is also increased. A lossless mathematical expression for $p_{2,0}$ for a resonator with varying geometry is provided and the simulation results showed that the for a Venturi cross-sectional area of 0.5, the time-averaged pressure differential between 0.5 and 0.6 m of the 1 meter-long resonator would diverge about 25% when compared to the lossless expression. The simulations with a Venturi only proved that $p_{2,0}$, also known as the acoustic radiation pressure, could be modified by changing the Venturi sizes.

The second set of simulations considered the addition of a loop (SCL) to the resonator with one end attached at the Venturi neck and the other at the location where the Venturi ended. In order to increase the accuracy in the models, time-averaged minor loss coefficients at the branch and the trunk of T-Junctions were calculated using empirical expressions through an iterative process. These empirical

expressions are originally intended for steady flow conditions which lead way to some uncertainties when applied to oscillating flows. The main uncertainty in the simulated minor loss coefficients were caused by the discontinuity observed at the steady flow data which would be only effective if the flow in the branch of a T-Junction changes direction. The time-averaged trunk minor loss coefficients relatively stayed constant at both junctions with varying Venturi sizes whereas the time-averaged branch minor loss coefficients decreased as the Venturi size decreased.

The Venturi-SCL simulations showed that the amount of the steady flow in the SCL increased as the Venturi diameter decreased. Unlike the case with no SCL, the acoustic power experienced at the piston face initially increased as the Venturi area ratio started to decrease starting from 1.0 to 0.5. This behaviour is explained by the fact that the amount of decrease related to the drop in the time-averaged branch minor loss coefficients being larger than the increase of the viscous resistance. It is also observed that the viscous losses started to dominate after a certain area ratio and that the acoustic power at the piston face started to decrease. Another observation made when the branch flow rates are examined in Figure 5.9 is that the steady flow magnitude and the alternating flow amplitude at the T-Junction #1 located at the Venturi's neck approach each other with smaller Venturi sizes. This indicates that at some area ratio, the magnitude of mean steady flow could be greater than the amplitude of the oscillating flow, preventing the direction reversal in the branch. How the time-averaged branch minor loss coefficients would behave in this case requires further analysis since smoothness in the averaged K curves would disappear without flow reversal.

The initial DeltaEC simulations with the Venturi-SCL combination did not produce reasonable results and this issue was later resolved by modifying how the time-averaged pressure at one of the junctions is calculated. In a personal interview with Greg Swift, who is one of the developers of DeltaEC, it was noted that the DeltaEC software treated all TBRANCH segments as if they were WYE-connections. In order to mimic the Bernoulli pressure at the branch of a T-Junction, an RPN segment is placed right after the TBRANCH where the flow splits which sets the second-order time-averaged pressure variable, p_{20DE} , to the calculated Bernoulli pressure which uses the acoustic variables at the branch. This modification is only applied to one of the junctions and DeltaEC calculated the time-averaged pressure at the other junction for convergence.

Another software related factor requiring close attention for future numerical

analyses is the inability of currently available version of DeltaEC's when calculating $p_{2,0}$ if a mean temperature gradient exists. Section 2.5 showed that if a mean temperature gradient exists, there should be an additional density gradient related term, $p_{2,0,\nabla\rho}$, added to the second-order time-averaged pressure term, $p_{2,0}$. The current version of DeltaEC does not incorporate this additional term in its calculations, therefore, heat carrying Venturi-SCL simulations would include an uncertainty in the results related to this inability [19].

7.1 Future Work and Improvements

The study presented in this work is a proof of concept for a Venturi-SCL combination to be used as an acoustic mass streaming method. Comparison simulations with a gas-diode-SCL combination would help identifying the more efficient streaming method. Depending on the operating conditions, such as the quality of the heat input and the specifications of the mechanical components where the energy is either delivered or extracted, varying amounts of steady mass flow might be desired for optimal performance. In this case, a parametric optimization study needs to be performed. In other words, a design that produces the largest amount of steady mass flow may not necessarily produce the most efficient assembly overall.

According to Rennels et al., one way of decreasing the losses at T-Junctions is the placement of a radius at the branch and trunk's joining edge [27]. Equations 4.10, 4.11, 4.12 and 4.15 in Section 4.2 show how the instantaneous minor loss coefficients are functions of the radius at the joining edge. Since the minor loss coefficients directly affect the steady flow rate in the SCL, this radius should be one of the design parameters if an optimization study is performed.

Another parameter that can be varied for controlling the steady mass flow rate is the location of the second T-Junction. In this study, the second connection was placed immediately after the Venturi, however, due to the distribution of $p_{2,0}$ along the resonator, larger pressure differentials can be obtained if the second junction is placed closed to the end. This modification would result in changes to the minor loss coefficients due to the reduced trunk flow rates as well as increasing the viscous losses due to the increased distance the steady flow travels in the resonator.

The thermoacoustic simulation presented by Steiner and Elferink matches the experimental results performed at Etalim Inc. qualitatively only [12]. It is stated that the simulation model used failed to capture the experimental reality perfectly

and the qualitative differences are currently unknown despite the considerable amount of effort put in. In a personal interview, Tom Steiner stated that the flow in the SCL did not initiate until a certain amount of gas displacement amplitude in the resonator was achieved. Measuring the exact gas displacement amplitude is impossible given the nature of the apparatus. In order to get around that, a displacement sensor attached to the generator module assembly provides a relative measurement by measuring the mechanical vibration amplitudes experienced by the hardware. The flow in the SCL is observed to be initiated at 70 microns of vibration amplitude at the generator module. The reason for this behaviour is currently unknown and further research is required for better understanding.

Lastly, experiments for determining the time averaged branch and trunk minor loss coefficients at a T-Junction need to be carried out to increase the accuracy of the simulations. These coefficients could be used whenever a branch is split from a resonator whether it is for an SCL or for other purposes.

Appendix A

Second-Order Time-Averaged Pressure

In order to understand how nonlinear terms cause a nonzero, positive pressure after a complete oscillation, it is convenient to consider a simple piston in a close-fitted cylinder that is treated as a “lumped element”.

The cylinder can be described as filled with an ideal gas at mean pressure, p_m , in equilibrium with the ambient and the piston area is A_p . Letting this equilibrium position for the piston to be $x = 0$ gives the equilibrium volume in the cylinder to be $V_o = A_p L$, where L is the length of the cylinder from the rigid end located at $x = L$ to the piston at equilibrium position as in Figure A.1.

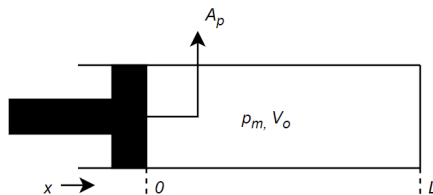


Figure A.1: Close-fitted Cylinder in Equilibrium

The first assumption is that the gas inside the piston obeys the adiabatic gas law, $pV^\gamma = \text{constant}$. Along with the cylinder being adiabatic, this assumption means that the pressure and volume changes are inversely proportional to each other with the constant of proportionality being the ratio of specific heats, γ . In other words, any amount of piston movement can be related to the change in pressure linearly.

Secondly, the lumped element assumption simply states that the pressure inside

the cylinder at any location will increase and decrease at the same time given that the conditions $\sqrt{A_p} \ll \frac{\lambda}{2\pi} = \frac{c}{\omega}$ and $L \ll \frac{c}{\omega}$ are true, which means that both the surface area of the piston and the length of the cylinder is much less than the wavelength of the gas at given operating conditions [25, pp. 844–846]. In other words, the piston moves so slowly and/or the cylinder is so short that the pressure change is experienced at all locations simultaneously. The adiabatic gas law and the lumped element assumption allow for the pressure at any location inside the cylinder to be independent of location but only a function of time. In the light of these assumptions, it is possible to conclude that the pressure inside the cylinder will be uniform at all times.

Assuming that the piston motion is purely sinusoidal, the piston position is given by $x(t) = x_1 \sin(\omega t)$. In this case, the pressure swing amplitude inside the cylinder is expressed as:

$$\begin{aligned}
 pV^\gamma = \text{const.} &\Rightarrow \frac{p_1(t)}{p_m} = -\gamma \frac{\delta V}{V_o} = -\gamma \frac{-A_p x_1 \sin(\omega t)}{A_p L} \\
 &\Rightarrow p_1(t) = -\gamma p_m \frac{x_1 \sin(\omega t)}{L} \\
 \text{let the constant } P &= \frac{-\gamma p_m x_1}{L} \text{ then,} \\
 p_1(t) &\equiv P \sin(\omega t)
 \end{aligned} \tag{A.1}$$

where γ is the ratio of heat capacities.

In this form, taking the time average of this linear pressure equation would result in zero as shown in Equation 2.6.

In order to mathematically show the nonlinearities, assumptions made while deriving Equation A.1 should be examined closely. Equation A.1 assumes that the amplitude of the piston's sinusoidal motion is much smaller than the cylinder's length, therefore the volume V_o is constant. In reality however, this is not the case and as the piston moves, the volume inside the cylinder changes by δV . Therefore the term V_o in Equation A.1 should be replaced by the variable volume $V_o(1 - \frac{\delta V}{V_o})$ to account for this change, resulting in a nonlinear expression.

If $\delta V/V_o < 0.1$, so that the lumped element assumption still holds, introducing this varying volume term to Equation A.1 results in a nonlinear expression for time dependent pressure inside the cylinder.

$$p_1(t) = -\gamma p_m \frac{\delta V}{V_o(1 - \frac{\delta V}{V_o})} \cong \gamma p_m \frac{\delta V}{V_o} \left(1 + \frac{\delta V}{V_o}\right) = -\gamma p_m \left[\frac{\delta V}{V_o} + \left(\frac{\delta V}{V_o}\right)^2 \right] \quad (\text{A.2})$$

Substituting $\delta V = A_p x_1 \sin(\omega t)$ and $V_o = A_p L$ gives:

$$p_1(t) = -\gamma p_m \left[\frac{x_1}{L} \sin(\omega t) + \left(\frac{x_1}{L}\right)^2 \sin^2(\omega t) \right] \quad (\text{A.3})$$

Using the trigonometric identity $\sin^2(\omega t) = \frac{1}{2}[1 - \sin(2\omega t)]$, Equation A.3 can be written as:

$$p_1(t) = -\gamma p_m \left[\frac{x_1}{L} \sin(\omega t) + \frac{1}{2} \left(\frac{x_1}{L}\right)^2 - \frac{1}{2} \left(\frac{x_1}{L}\right)^2 \sin(2\omega t) \right] \quad (\text{A.4})$$

Taking the integral of Equation A.3 over period T will eliminate the sinusoidal terms, however, the constant term will produce a nonzero result.

$$p_{2,0} = \frac{\gamma p_m}{2} \left(\frac{x_1}{L}\right)^2 \quad (\text{A.5})$$

With $x_1/L = p_1/\gamma p_m = p_1/\rho c^2$, Equation A.5 can be written as:

$$p_{2,0} = \frac{|p_1|^2}{2\rho_m c_o^2} \quad (\text{A.6})$$

with c_o being the speed of sound in the working fluid.

Unlike Equation A.1, taking the integral of this nonlinear expression of pressure resulted in a nonzero quantity. Equation A.6 clearly shows the quadratic relationship between the first order pressure amplitude, p_1 , and the nonzero time-averaged pressure in the cylinder, $p_{2,0}$. This positive quantity will tend to push the piston away from the closed end of the cylinder. This average force exerted on the cylinder which pushes it away from the closed end of the cylinder is called “piston walk” in Stirling cycle machines. This quantity is also equal to the potential energy density of the fluid at any given point along the cylinder. Multiplying this quantity by volume will produce the potential energy stored in that volume of gas.

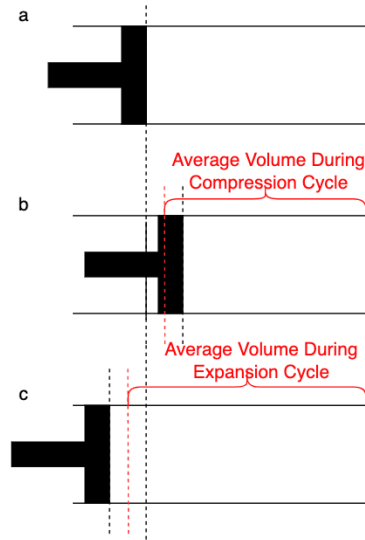


Figure A.2: Volumetric Asymmetry in a Close-Fitted Piston Assembly. a) Piston at rest at x_0 with p_m inside the cylinder is equal to the ambient pressure. b) Piston at bottom dead center at $t = \pi/4$. Red dotted line showing the average volume of the gas while the volume is less than V_o . c) Piston at top dead center, red dotted line showing the average volume experienced by the gas for times when the gas is expanded over V_o .

Figure A.2 shows the asymmetry produced in the cylinder where the average volume in the cylinder during the compression cycle being smaller than the average volume during the expansion cycle. The nonzero time-averaged pressure found in Equation A.6 is attributed to this asymmetry.

In the case of a standing wave, the lumped element assumption ceases to be valid because the cylinder length and the wavelength of the oscillation is comparable. The pressure inside the cylinder would be a function of both time and space, creating a pressure gradient. This pressure gradient will move particles with a sinusoidal velocity which is also a function of time and space.

The excess mean pressure, $p_{2,0}$, found in Equation A.6 should be added to the mean pressure, p_m , since both values do not change with time. For a standing wave, $p_{2,0}$, reaches a maximum at the pressure antinodes where the pressure swing is maximum. This increased mean pressure means an increase in density, and since the cylinder is sealed and the mass is constant, this increase in density must come in the expense of decrease in density at other locations. In the light of this, it can be concluded that at a first-order pressure node, the nonzero, second-order time-averaged pressure must be equal and opposite in sign to the value found in Equation A.6, so that the mass is conserved. At a pressure node, p_1 is zero and the amplitude of the

particle velocity at is given by $u_1 = p_1/\rho_m c_o$, thus, $p_{2,0}$ can be written as:

$$p_{2,0} = -\frac{|p_1|^2}{2\rho_m c_o^2} = -\frac{1}{2}\rho_m |u_1|^2 \quad (\text{A.7})$$

It should be noted that Equation A.7 is equal to the kinetic energy density of the gas at a pressure node whereas Equation A.6 is the potential energy density at a pressure antinode.

Appendix B

Irreversibilities in Acoustic Flows

B.1 Viscous Resistance Losses

Viscous resistance for any type of viscous fluid flow is caused by the fact that at the solid-fluid boundary, the fluid is practically stagnant. In literature, this phenomenon is called the no-slip boundary condition. For a viscous, laminar, steady internal flow of ideal gas in a constant geometry pipe, the fluid particles located at the same distance from the wall move at the same velocity. Assuming the flow is in the \hat{x} -direction, these constant velocity particles would create concentric cylinders of fluid layers with the fastest one being just a streamline of particles at the center of the circular pipe and the slowest one being stagnant at the fluid-solid boundary. The velocity difference between these concentric layers is caused by viscosity which is defined as the ability of a fluid to transfer momentum. The drag experienced by these layers become less and less significant as the distance from the wall increases and becomes negligible after a certain distance. The differential velocity between these layers of fluid with different velocities cause friction and friction generates heat which is a form of lost of energy.

In oscillation flows, the characteristic length measuring the perpendicular distance to the direction of motion which momentum can diffuse in half a period time is called the viscous penetration depth, δ_v :

$$\delta_v = \sqrt{\frac{2\mu}{\omega\rho}} = \sqrt{\frac{2\nu}{\omega}} \quad (\text{B.1})$$

where μ and ν are the fluid's dynamic and kinematic viscosities respectively.

To develop an understanding about how viscous forces affect an oscillating flow, the momentum equation, which is a manifestation of Newton's second law, $F = ma$ is used. Then, the \hat{y} and \hat{z} dependence of the \hat{x} component of an oscillating flow can be described via:

$$i\omega\rho_m u_1(x, y) = -\frac{dp_1}{dx} + \mu \left[\frac{\partial^2 u_1}{\partial y^2} + \frac{\partial^2 u_1}{\partial z^2} \right] \quad (\text{B.2})$$

Equation B.2 shows the balance of forces acting on a differential volume of oscillating fluid for laminar flow. The left side is simply mass times acceleration. The right side consists of the pressure force and the viscous force acting on the differential volume of fluid. Equation B.2 is an ordinary differential equation of u_1 which a solution is known for given the boundary conditions $u_1(y = z = 0) = 0$ (no-slip at the wall), and u_1 has a finite value at some distance away from the solid surface. The solution with these boundary conditions is:

$$u_1 = \frac{i}{\omega\rho_m} [1 - h_v(y, z)] \frac{dp_1}{dx} \quad (\text{B.3})$$

This equation defines a new complex variable h_v , which is a function of channel geometry. Since the local flow properties are not of interest, Equation B.3 is integrated over y and z and this turns the left hand-side of the equation to volumetric flow rate U_1 while providing a new complex variable f_v , the spatial average for h_v . Solving for dp_1 yields an expression for the pressure drop per unit length.

$$dp_1 = -\frac{i\omega\rho_m dx/A}{1 - f_v} U_1 \quad (\text{B.4})$$

For a wide open channel where the boundary layer approximation is valid, h_v and its spatial average f_v are described as:

$$h_v = e^{-(1+i)y/\delta_v} \quad (\text{B.5})$$

$$f_v = \frac{(1-i)\delta_v}{2r_h} \quad (\text{B.6})$$

where r_h is the hydraulic radius.

The complex function h_v , contains the viscosity term embedded in it, as well as a nonzero imaginary component. This imaginary component causes the velocity of the particles have a y dependent phase shift. Figure B.1(b) shows the magnitude of particle displacements with real and imaginary parts. The displacement of particles can be visualized as going from positive real part to negative imaginary part smoothly,

then to negative real part before going back to positive imaginary part in 4 equal divisions of a period. At locations far away from the wall, viscosity loses significance hence the imaginary part approaches zero. This portion of the flow is purely inertial which means the particles' acceleration is in phase with the force they experience which is caused by the pressure gradient $-\frac{dp_1}{dx}$. At distance δ_v from the wall, the phase shift is the most significant. In the light of these, it can be concluded that the existence of viscosity and the no-slip condition creates a resistive component counteracting the pressure gradient that is responsible for the motion in the first place, as well as modifying the magnitude of the inertial contribution. The viscous resistance in oscillating flows also creates a phase shift between the gas outside the boundary layer and the gas closer to the wall which further increases the losses.

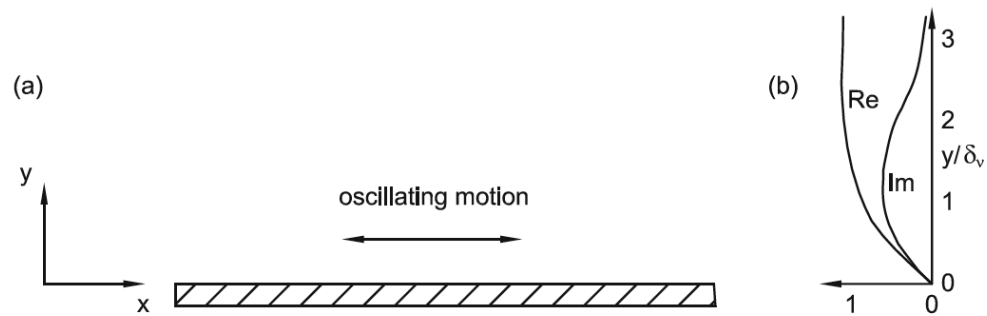


Figure B.1: (a) Depiction of the oscillating flow direction in a very large channel (b) The real and imaginary components of the particle displacements [14].

The spatial average function f is available for a number of geometries [29]. Figure B.2 shows values for $F = 1 - f_v$ which are very similar despite the significant differences in geometries. Note that the particle displacement profile shown in Figure B.1(b) qualitatively agrees with the the profiles in Figure B.2.

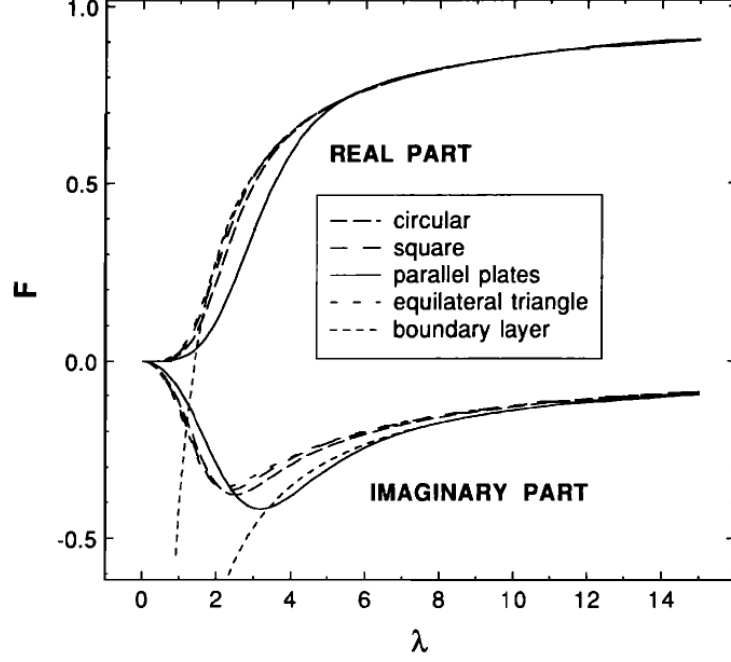


Figure B.2: $F = 1 - f_v$ values for various geometries. The x-axis λ is a dimensionless variable indicating the distance measured from the solid surface [29].

Defining the complex spatial average function f_v for viscous irreversibilities allows for Equation B.4 to be rewritten in following form.

$$dp_1 = -(i\omega l dx + r_v dx)U_1 \quad (\text{B.7})$$

where l and r_v are defined as inertance and viscous resistance per unit length of channel.

$$l = \frac{\rho_m}{A_c} \frac{1 - \text{Re}[f_v]}{|1 - f_v|^2} \quad (\text{B.8})$$

$$r_v = \frac{\omega \rho_m}{A_c} \frac{\text{Im}[-f_v]}{|1 - f_v|^2} \quad (\text{B.9})$$

Equation B.7 provides pressure drop per unit length in a laminar internal oscillating flow. Note that if $f_v = 0$ or some purely real value, r_v in Equation B.9 becomes zero, indicating that the motion is purely inertial. At the limit away from the wall, the imaginary part of f_v approaches zero as see in Figure B.2, causing viscous resistance to be less significant, therefore the flow becomes purely inertial as

mentioned previously.

B.2 Thermal Relaxation Losses

Thermal relaxation is another source of irreversibility in oscillating flows causing acoustic attenuation at the fluid-solid boundary. This attenuation is the product of temperature changes caused by the pressure oscillations in the gas. For an ideal gas, temperature and pressure is related through the ideal gas law. The oscillating temperature experienced by the gas creates a sinusoidal temperature difference with the solid wall assuming constant wall temperature due to much larger heat capacity. This creates a similar effect to “*no-slip*” condition for temperature at the wall since the gas temperature is “*anchored*” to the wall temperature. The heat transfer to and from the wall creates entropy, hence loss.

The mathematical expression for thermal relaxation losses is derived from the conservation of mass (continuity) and the general heat transfer equations. The first order approximation of the heat transfer equation for oscillating gas in a wide open channel is:

$$\rho_m c_p \left(i\omega T_1 + u_1 \frac{dT_m}{dx} \right) - i\omega p_1 = k_{th} \left(\frac{\partial^2 T_1}{\partial y^2} + \frac{\partial^2 T_1}{\partial z^2} \right) \quad (\text{B.10})$$

The left side of Equation B.10 is the difference between the stored thermal energy of the gas parcel and its potential energy caused by pressure. The right side of the equation shows that the difference is simply the conductive heat transfer to the parcel from the directions \hat{x} and \hat{y} .

Equation B.10 is an ordinary differential equation of the oscillating temperature T_1 . Considering the y and z dependencies for both u_1 and T_1 , a solution exists [30].

$$T_1 = \frac{1}{\rho_m c_p} (1 - h_\kappa) p_1 - \frac{1}{i\omega A_c} \frac{dT_m}{dx} \frac{(1 - h_\kappa) - Pr(1 - h_v)}{(1 - f_v)(1 - Pr)} U_1 \quad (\text{B.11})$$

where Pr is the Prandtl number, defined as the ratio of momentum diffusivity to heat diffusivity, $Pr = \frac{\mu}{c_p k_{th}}$. The variables h_κ and f_κ are thermal equivalents of h_v and f_v where δ_v is replaced with δ_κ .

$$\delta_\kappa = \sqrt{\frac{2 k_{th}}{\omega \rho_m c_p}} = \sqrt{\frac{2 \kappa}{\omega}} \quad (\text{B.12})$$

where κ and k_{th} are the thermal diffusivity and conductivity of the gas respectively.

$$h_\kappa = e^{-(1+i)y/\delta_\kappa} \quad (\text{B.13})$$

$$f_\kappa = \frac{(1-i)\delta_\kappa}{2r_h} \quad (\text{B.14})$$

Taking the spatial average of Equation B.11 converts h_v and h_κ to f_v and f_κ .

$$\overline{T}_1 = \frac{1}{\rho_m c_p} (1 - f_\kappa) p_1 - \frac{1}{i\omega A_c} \frac{dT_m}{dx} \frac{(1 - f_\kappa) - Pr(1 - f_v)}{(1 - f_v)(1 - Pr)} U_1 \quad (\text{B.15})$$

Using the ideal gas law, density of the gas can be related to temperature and pressure.

$$\overline{\rho}_1 = \frac{\rho_m}{T_m} \overline{T}_1 + \frac{\rho_m}{p_m} p_1 \quad (\text{B.16})$$

For a flow oscillating in \hat{x} direction, the continuity equation provides an expression for the mass balance.

$$i\omega \overline{\rho}_1 + \frac{d}{dx}(\rho_m \overline{u}_1) = 0 \quad (\text{B.17})$$

Spatially averaging Equation B.3 to obtain \overline{u}_1 and obtaining an expression for $\overline{\rho}_1$ by substituting Equation B.15 into Equation B.16 allows solving Equation B.17 for oscillating volume flow rate as a function of oscillating pressure and volumetric flow rate.

$$dU_1 = -\frac{i\omega A_c dx}{\gamma p_m} [1 + (\gamma - 1) f_\kappa] p_1 + \frac{f_\kappa - f_v}{(1 - f_v)(1 - Pr)} \frac{dT_m}{T_m} U_1 \quad (\text{B.18})$$

where γ is the ratio of isobaric and isochoric specific heats.

Equation B.18 can be seen as the thermoacoustic equivalent of the continuity equation. The left side of the equality is the change in the volumetric flow rate, dU_1 , which is defined as the difference between the pressure oscillations and the velocity oscillations (terms on the right hand-side). Considering the first term on the right, if the term $f_\kappa = 0$ then there is no contact between the gas and the solid surface, hence the temperature oscillations created by p_1 are purely adiabatic, there is no heat transfer creating entropy. Continuing with the same term, multiplying the pressure oscillations, p_1 , of an infinitesimal volume of gas, $A_c dx$, with the compliance of the gas, which is $\frac{1}{\gamma p_m}$, gives the velocity, or in this case, volumetric flow rate oscillations.

Multiplication of these three terms confirms the units.

The volumetric flow rate term on the right is a function of both f_κ and f_v along with the mean temperature gradient dT_m . In the inviscid case where $f_v = 0$, Pr would also be zero which indicates that the thermal relaxation of the gas near the solid boundary causes changes in the vertical gradient of velocity on its own, given that the mean temperature gradient is nonzero. If the flow is not inviscid, this effect on the gradient is modified since viscosity would change the profile of U_1 . If f_κ is zero, then there is no contact with the solid wall hence the infinitesimal gas parcel's temperature does not change as it oscillates along \hat{x} direction, this indicates that if f_κ is zero, then dT_m is zero which means there is no contribution from the second term.

Now that the terms are explained, it is possible to simplify Equation B.18 to the following form.

$$dU_1 = - \left(i \omega c dx + \frac{1}{r_\kappa} dx \right) p_1 + g dx U_1 \quad (\text{B.19})$$

where c is defined as compliance per unit length, r_κ as the thermal relaxation conductance and g as a complex gain/attenuation term which only exists when a temperature gradient is present. This intuitively makes sense since an increase in mean temperature would mean a decrease in mean density, less dense gas will move more easily, increasing the displacement amplitude, hence the velocity.

$$c = \frac{A_c}{\gamma p_m} (1 + [\gamma - 1] \text{Re}[f_\kappa]) \quad (\text{B.20})$$

$$\frac{1}{r_\kappa} = \frac{\gamma - 1}{\gamma} \frac{\omega A_c \text{Im}[-f_\kappa]}{p_m} \quad (\text{B.21})$$

$$g = \frac{f_\kappa - f_v}{(1 - f_v)(1 - Pr)} \frac{1}{T_m} \frac{dT_m}{dx} \quad (\text{B.22})$$

It should be noted that r_v is insignificant when zero, which is the inviscid case, however, r_κ is insignificant when approaching infinity. As the channel size increases, the effects of both of these irreversibilities become insignificant. The larger the channel cross-sectional area in the denominator of Equation B.9, the smaller the r_v value. Equation B.21 shows that as the cross-sectional area increases, r_κ goes to infinity, making the second term in brackets in Equation B.19 approach zero.

B.3 Turbulence and Iguchi's Quasi-Steady State Assumption

Viscous loss expression in Appendix B.1 is derived for laminar flow conditions since the assumptions were based on the Rott's acoustic approximations. But in real life, turbulent flows are much more common than laminar flows. For fluid dynamics, turbulence is a phenomenon that has been puzzling the scientific community for more than a century so the specifics of the phenomenon goes beyond the scope of this work, hence the underlying mechanisms causing the turbulent behaviour will not be discussed in detail. However, methods of approximating the effects for both steady and oscillating turbulent flows will be introduced. It should be noted that for oscillating flows, the uncertainties and the unknowns are even greater since an overwhelming majority of the available turbulent flow data are based on the steady, time-independent flow conditions.

For steady internal flows, the well-known Moody's diagram provides a friction factor, f_M , which takes two dimensionless variables as inputs, Re , the Reynolds number, and the relative roughness ratio, $\frac{\epsilon}{d}$, which is the ratio of surface roughness of the pipe's inner face to its diameter.

$$Re = \frac{\rho u d_h}{\mu} \quad (\text{B.23})$$

Equation B.23 defines the dimensionless Reynolds number for a steady, internal flow where d_h is the hydraulic diameter of the pipe.

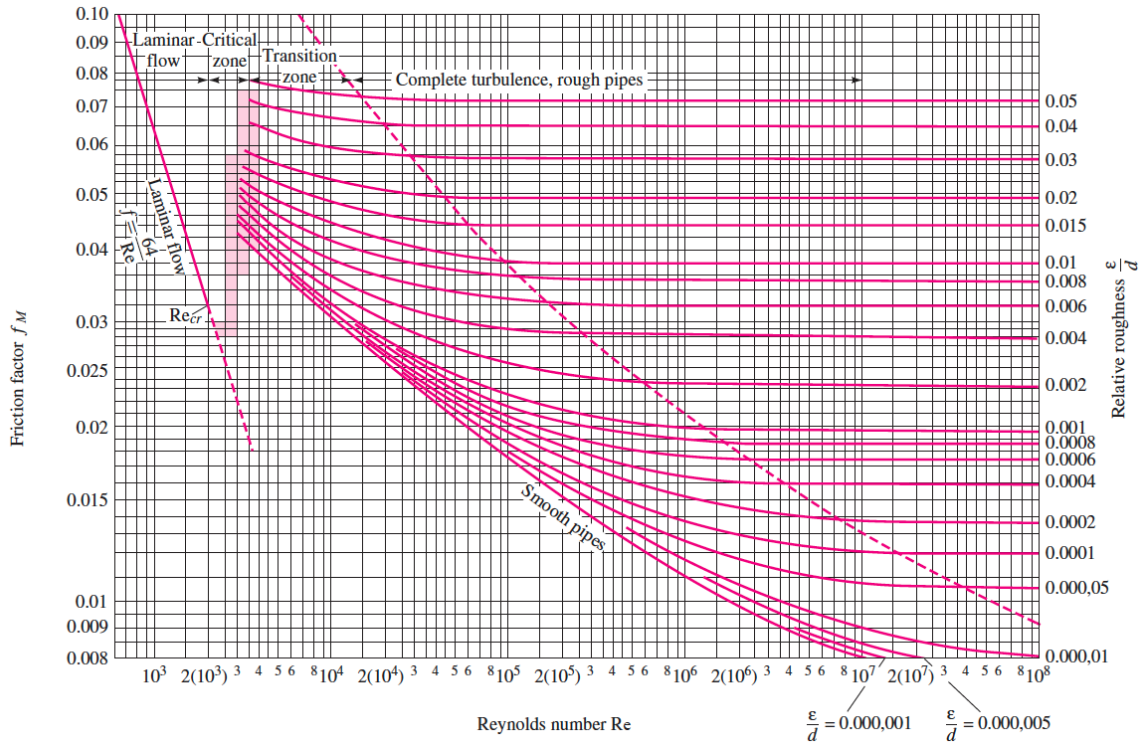


Figure B.3: Friction factor f_M as a function of Re and $\frac{\epsilon}{d}$. Adapted from [31].

Figure B.3 shows that there are two flow regimes. Laminar region for $Re \sim < 2000$ and the turbulent region at $Re \sim > 2000$. In the laminar region the friction factor f_M is given by:

$$f_M = \frac{64}{Re} \quad (\text{B.24})$$

The curves for the turbulent region are generated by an implicit function which requires iterative solutions to converge.

$$\frac{1}{\sqrt{f_M}} = -2 \log_{10} \left(\frac{\epsilon/d_h}{3.7} + \frac{2.51}{Re\sqrt{f_M}} \right) \quad (\text{B.25})$$

For a distance L between two points along the pipe, knowing the friction factor allows for calculating the pressure drop in a turbulent viscous flow.

$$\Delta p = f_M \frac{L}{d_h} \frac{1}{2} \rho \bar{u}^2 \quad (\text{B.26})$$

In the early days of thermoacoustic engines and refrigerators, Rott's laminar flow approximations provided scientists with reasonably accurate results since the power

output of the machines were not considerably high. As the power delivery capabilities of thermoacoustic machines increased, so did the amplitudes in the system, causing a divergent trend to emerge between the models and the experiments. Figure B.4 shows the divergence of simulations from experiments where a decrease in measured pressure amplitudes can be seen. This decrease is attributed to nonlinearities in the system such as turbulence [14, pp. 183].

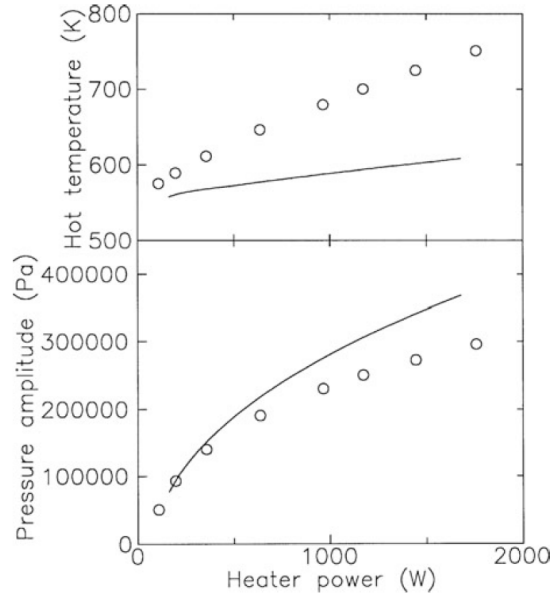


Figure B.4: Comparison of Rott's approximation for laminar flows and the experimental results for high power, thermoacoustic applications. The lines represent DELTAEC simulations for laminar flow. Circles represent experimental measurements [14].

Assumptions and methods that are used to calculate r_v in Section 4.1 require modifications due to turbulence to account for some portion of the divergence seen in Figure B.4, given that the flow experiences complete turbulence at some point during its period.

For oscillating flows, another dimensionless parameter is required show the complex behaviour of the flow. Although different dimensionless parameters are used for this purpose such as $d_h/\sqrt{2}\delta_v$ and $\overline{u_1} \frac{\delta_v \rho_m}{\mu}$, the dimensionless variable d_h/δ_v is the common choice within the scientific community. Figure B.5 shows a slice of the three-dimensional diagram for a smooth pipe, using the d_h/δ_v dimensionless parameter on the left vertical axis. There are 2 regions in the diagram there are not present in Figure B.3: the weakly turbulent and the conditionally turbulent regions. The weakly turbulent region has the same characteristics of the laminar flow inside the

boundary layer, turbulence related vortices are confined to the center of the pipe. However, at high Reynolds number flows, the turbulence disturbs the boundary layer destructively, making Rott's acoustic approximations invalid.

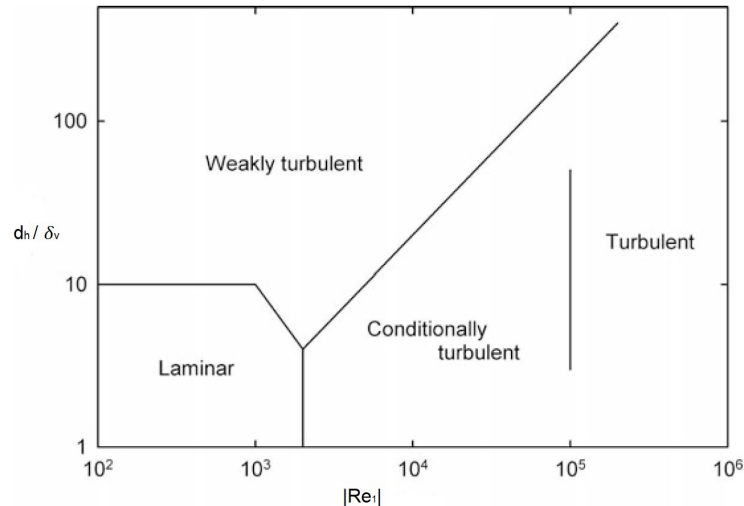


Figure B.5: Regimes of oscillating flow for pipe roughness ratio of $\epsilon = 0$ as a function of peak Reynolds number, $|Re_1|$. Adapted from [14].

Experiments investigating oscillating turbulent pipe flow showed that there exists transitional region between the weakly turbulent and fully turbulent regions [32]. In this conditionally turbulent region, the flow alternates between weakly turbulent and fully turbulent behavior. An interesting phenomenon observed here is that the flow behaves as if it has memory. If the peak Reynolds number of the flow falls into the turbulent region, the flow is observed to be turbulent throughout its period, resembling the turbulent behaviour of a steady flow. However, if the peak Reynolds number falls into the conditionally turbulent region, the flow alternates between weakly turbulent and fully turbulent behaviours, depending on its temporal location in the oscillatory period. To be more specific, the flow stays weakly turbulent until the maximum velocity (peak Reynolds number falling into the conditionally turbulent region) is reached, then it turns fully turbulent as it slows down, still moving in the same direction. The flow stays fully turbulent until the flow comes to a stop. As the zero velocity is crossed and the flow direction is reversed, the flow returns to weakly turbulent behaviour. In other words, if the flow is approaching its maximum velocity, it is weakly turbulent or laminar, depending on where it lies on the y -axis Figure B.5, and if the flow is approaching zero velocity, it is fully turbulent.

It is no doubt that turbulence should also affect the other impedance terms such as inertance l , compliance c , thermal relaxation r_κ and the source/sink term g . However, the experimental confirmation for such effects only exists for r_v , which is called the Iguchi's quasi-steady state assumption [33]. The effect of turbulence on other terms solely consists of assumptions and ideas without experimental studies to support their accuracy. Hence, this work only expands on the effects of turbulence on viscous losses.

In the weakly turbulent regime, the boundary layer is not deeply affected by the vortices so Rott's linear approximations are still valid allowing for r_v to be used in this case. In the fully turbulent regime however, Iguchi's hypothesis provides a turbulent viscous resistance term which should be used instead of r_v . The hypothesis states that if the gas displacement amplitude is much larger than both the diameter of the pipe and the viscous penetration depth, or if the oscillating frequency is relatively low, then the flow should have no memory of its past history, therefore, flow at any instant of time should be identical to that of fully developed steady flow. Integrating the instantaneous friction factor $f_M(t)$ from Equation B.25 over a period and taking the time average should provide a time-averaged friction factor for the flow which can be used to determine the turbulent viscous loss coefficient. The instantaneous friction factor for an oscillating flow is given by:

$$f_M(t) \approx f_M + \frac{df_M}{dRe_1} |Re_1| \left(\frac{|\operatorname{Re}[U_1 e^{i\omega t}]|}{|U_1|} - 1 \right) \quad (\text{B.27})$$

The terms f_M and $\frac{df_M}{dRe_1}$ in Equation B.27 are evaluated at the peak Reynolds number. Note that the italic Re denotes the Reynolds number while the $\operatorname{Re}[\]$ denotes the real part of a complex number as used in chapters 2,3 and 4. The only time varying component of this equation is the ratio of the instantaneous amplitude of the volumetric flow rate to its maximum value inside the brackets, which causes magnitude of the term inside the brackets sinusoidally oscillate between zero and one. Integrating and time averaging Equation B.27 gives the turbulent friction factor. A comparison between the amount of power loss in a turbulent case against the laminar case allows for a turbulent viscous resistance term to be derived as done in deriving Equation 7.24 in Reference [14].

$$r_{v,turb} = \frac{64\rho_m|U_1|}{3\pi^3 d_h^5} \left[f_M - \left(1 - \frac{9\pi}{32} \right) |Re_1| \frac{df_M}{dRe_1} \right] \quad (\text{B.28})$$

where f_M and $\frac{df_M}{dRe_1}$ are evaluated at the peak Reynolds number.

Substituting Equation B.28 into Equation B.7 instead of the laminar resistance term, r_v , would allow for calculating the pressure drop per length for oscillating turbulent flows.

Appendix C

Time-Averaged Minor Loss Coefficient for Converging-Diverging Pipe Flow

An oscillating flow going through any abrupt area change would experience sudden expansion during one half of the period and sudden contraction during the other half. A recent study regarding the time averaged minor loss coefficients for such abrupt area change found that there was no correlation between the oscillation frequency (flow velocity), and the time averaged minor loss coefficient [28].

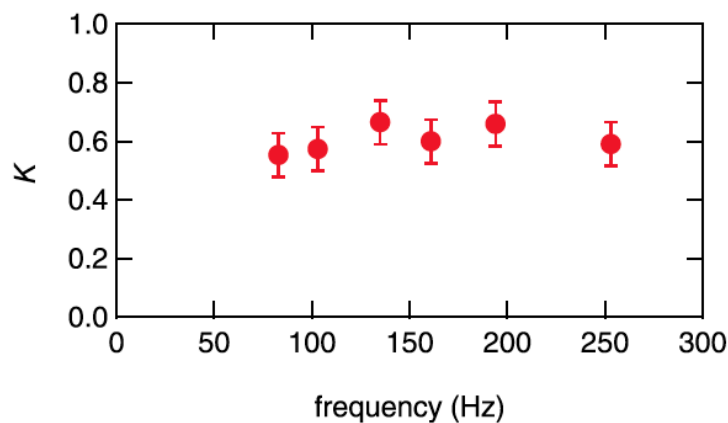


Figure C.1: Frequency dependence of the time averaged abrupt area change minor loss coefficient [28].

Placing tapers between the area changes are used to reduce losses associated

with such geometries. Figure C.2 shows the relationship between the taper angle and the time-averaged minor loss coefficient for a Venturi.

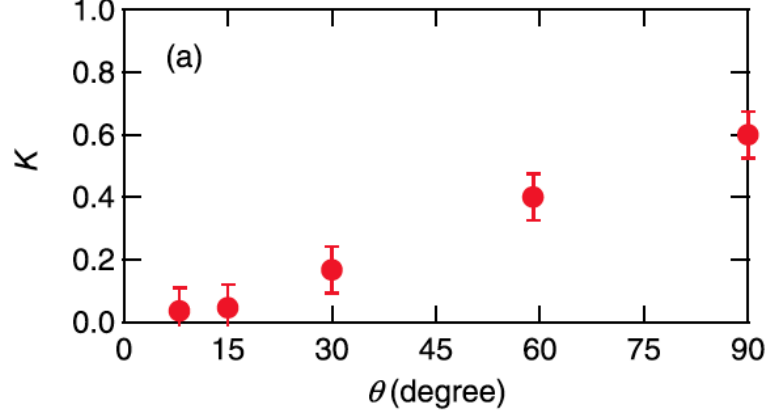


Figure C.2: Time-averaged minor loss coefficient for tapered area change in an oscillating pipe flow [28].

Equation C.1 from Reference [28] provides an expression for the time averaged minor loss coefficient for a tapered pipe flow as a function of the taper angle and the area ratio.

$$\overline{K_{Tp}} = [0.69(\theta - 0.09)] \left[\frac{1}{2} \left(1 - \frac{A_S}{A_L} \right)^2 + \frac{1}{4} \left(1 - \frac{A_S}{A_L} \right)^{0.75} \right] \quad (\text{C.1})$$

$$(A_S < A_L, \frac{\pi}{12} < \theta < \frac{\pi}{2})$$

where θ is in radians and A_S and A_L are the small and large cross-sectional areas respectively. Figure C.3 shows the definition of the taper angle θ . Reference [28] states that for taper angles less than 8° , the minor loss coefficient is insignificant and provides an empirical relationship between the taper angle and the time-averaged minor loss coefficient.

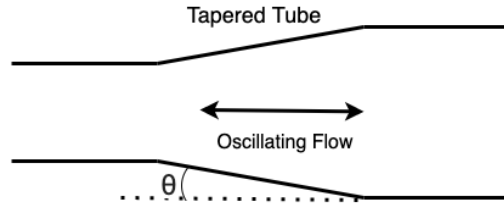


Figure C.3: Schematic for tapered area change and the definition of taper angle θ .

Appendix D

DELTAEC Codes

```

1 StraightPipeResonatorWithVenturi StraightPipeF20
2 This simulation is created to see the comparison of lossless Eq 3.6 to the
3 DELTAEC simulation with losses.
4 0 BEGIN Change Me
5 1.2000E+5 a Mean P Pa
6 Gues 245.27 b Freq Hz
7 298.00 c TReq K
8 Gues 0.89678 d |p| Pa
9 0.0000 e Ph(p) deg
10 5.0000E-4 f |U| m^3/s
11 0.0000 g Ph(U) deg
12 Optional Parameters
13 helium Gas type
14 1 SURFACE Change Me
15 Same 2a 2.5000E-3 a Area m^2 0.89678 A |p| Pa
16 0.0000 B Ph(p) deg
17 5.0000E-4 C |U| m^3/s
18 0.0000 D Ph(U) deg
19 2.2419E-4 E Htot W
20 2.2419E-4 F Edot W
21 ideal Solid type
22 2 DUCT Change Me
23 2.5000E-3 a Area m^2 Mstr 22.716 A |p| Pa
24 0.17724 b Perim m 2a -88.815 B Ph(p) deg
25 0.4000 c Length m 4.0866E-4 C |U| m^3/s
26 Master-Slave Links -0.6281 D Ph(U) deg
27 Optional Parameters 2.2419E-4 E Htot W
28 ideal Solid type 1.4690E-4 F Edot W
29 3 CONE Change Me
30 Same 2a 2.5000E-3 a AreaI m^2 Mstr 27.768 A |p| Pa
31 0.17724 b PerimI m 3a -89.317 B Ph(p) deg
32 7.5000E-2 c Length m 3.8209E-4 C |U| m^3/s
33 Same 4a 1.2500E-3 d AreaF m^2 Mstr -0.69125 D Ph(U) deg
34 0.12533 e PerimF m 3d 2.2419E-4 E Htot W
35 Master-Slave Links 1.2722E-4 F Edot W
36 Optional Parameters
37 ideal Solid type
38 DUCT Change Me
39 1.2500E-3 a Area m^2 Mstr 32.327 A |p| Pa
40 0.12533 b Perim m 3a -89.663 B Ph(p) deg
41 5.0000E-2 c Length m 3.6740E-4 C |U| m^3/s
42 -Slave Links -0.70537 D Ph(U) deg
43 al Parameters 2.2419E-4 E Htot W
44 Solid type 1.0808E-4 F Edot W
45 CONE Change Me
46 ne 4a 1.2500E-3 a AreaI m^2 Mstr 36.871 A |p| Pa
47 0.12533 b PerimI m 5a -89.904 B Ph(p) deg
48 ne 3c 7.5000E-2 c Length m 3.2958E-4 C |U| m^3/s
49 ne 2a 2.5000E-3 d AreaF m^2 Mstr -0.7281 D Ph(U) deg
50 0.17724 e PerimF m 5d 2.2419E-4 E Htot W
51 -Slave Links
52 al Parameters 8.7354E-5 F Edot W
53 Solid type
54 DUCT Change Me
55 ne 2a 2.5000E-3 a Area m^2 Mstr 45.108 A |p| Pa
56 0.17724 b Perim m 6a -90.204 B Ph(p) deg
57 ne 2c 0.4000 c Length m 1.2809E-7 C |U| m^3/s
58 -Slave Links -90.204 D Ph(U) deg
59 al Parameters 2.2419E-4 E Htot W
60 Solid type 2.8889E-6 F Edot W
61 SURFACE Change Me
62 ne 2a 2.5000E-3 a Area m^2 45.108 A |p| Pa
63 -90.204 B Ph(p) deg
64 5.6594E-16 C |U| m^3/s
65 82.466 D Ph(U) deg
66 2.2419E-4 E Htot W
67 Solid type -1.2660E-14 F Edot W
68 HARDEND Change Me
69 0.0000 a R(1/z) 45.108 A |p| Pa
70 0.0000 b I(1/z) -90.204 B Ph(p) deg
71 5.6594E-16 C |U| m^3/s
72 82.466 D Ph(U) deg
73 le targets 2.2419E-4 E Htot W
74 -1.2660E-14 F Edot W
75 -9.8007E-13 G R(1/z)
76 1.2607E-13 H I(1/z)

```

Figure D.1: DELTAEC code used for simulations in Section 5.1. Variable 4a (line 38) is varied for changing Venturi sizes.

```

4 Venturi-SCL-Simulation-125 FinalSIM
2 0 BEGIN Change Me
3 Turbulent flow with 1.2 bar Pm. Piston displacement creates SE-4 m3/s of
  flow.
5 1.2000E+7 a Mean P Pa
6 Gues 447.18 b Freq Hz
7 298.00 c TBeg K
8 Gues 3.6432E+5 d lpl Pa
9 0.0000 e Ph(p) deg
10 5.0000E-4 f |U| m^3/s
11 0.0000 g Ph(U) deg
12 0.0000 i Ndot mol/s
13 Optional Parameters
14 helium Gas type
15 1 SURFACE Piston face
16 This segment creates the resonator end with the piston.
17 Same 2a 2.5000E-3 a Area m^2 3.6432E+5 A |p| Pa
18 0.0000 B Ph(p) deg
19 4.9855E-4 C |U| m^3/s
20 -0.16717 D Ph(U) deg
21 91.079 E Htot W
22 Ideal Solid type F 90.814 F Edot W
23 2 DUCT Change Me
24 2.5000E-3 a Area m^2 Mstr 1.6288E+5 A |p| Pa
25 0.17724 b Perim m 2a -1.1229 B Ph(p) deg
26 0.4000 c Length m 4.1376E-2 C |U| m^3/s
27 5.0000E-4 d Srough -89.715 D Ph(U) deg
28 Master-Slave Links 91.079 E Htot W
29 Optional Parameters 82.789 F Edot W
30 Ideal Solid type
31 3 CONE Change Me
32 Same 2a 2.5000E-3 a AreaI m^2 Mstr 6.3446E+4 A |p| Pa
33 0.17724 b PerimI m 3a -3.0968 B Ph(p) deg
34 7.5000E-2 c Length m 4.3796E-2 C |U| m^3/s
35 Same 13a 1.2500E-3 d AreaF m^2 Mstr -89.818 D Ph(U) deg
36 0.12533 e PerimF m 3d 91.079 E Htot W
37 5.0000E-4 f Srough 79.469 F Edot W
38 Master-Slave Links
39 Optional Parameters
40 Ideal Solid type
41 Ideal Solid type
42 4 DUCT Venturi Neck
43 1.2500E-3 a Area m^2 Mstr 1.5898E+4 A |p| Pa
44 0.12533 b Perim m 3a -12.578 B Ph(p) deg
45 2.5000E-2 c Length m 4.3970E-2 C |U| m^3/s
46 5.0000E-4 d Srough -89.839 D Ph(U) deg
47 Master-Slave Links 91.079 E Htot W
48 Optional Parameters 77.073 F Edot W
49 Ideal Solid type
50 5 TBRANCH Flow splits here
51 Gues 3.9083E+5 a Ra(2b) Pa-s/m^3 1.5898E+4 A |p| Pa
52 Gues 1.8703E+6 b Im(2b) Pa-s/m^3 -12.578 B Ph(p) deg
53 Gues -29.868 d NdotBr mol/s P 8.3202E-3 C |U| m^3/s
54 Master-Slave Links -90.775 D Ph(U) deg
55 Optional Parameters 1259.4 E HtotBr W
56 13.528 F EdotBr W
57 63.546 G EdotTr W
58 6 RFN Bernoulli pressure at the TBRANCH
59 Bernoulli pressure is set here to be p2ODE since DELTAEC cannot distinguish
60 a WYE connection and a TEE connection. In the second branch, DELTAEC is
61 able to find the suitable pressure. No need to set it again.
62 0.0000 a G or T F -5996.6 A ChngMe
63 p2ODE 4C mag 4a / sqrt rho * 4 / - *p2ODE
64 7 RFN Convert molar mass in TBRANCH to Volume Flow Rate
65 Takes the NdotBr molar flow rate from TBRANCH as input. Multiplies it with
66 molar mass in kg/mol and divides by density.
67 0.0000 a G or T F 6.1869E-3 A m^3/s
68 5d .004002 * rho / abs
69 8 MINOR 1st Connection Branch Coefficient - Time Averaged
70 Same 9a 6.5000E-4 a Area m^2 1.5724E+4 A |p| Pa
71 0.4148 b K+ -9.0078 B Ph(p) deg
72 Same 8b 0.4148 c K- 8.3202E-3 C |U| m^3/s
73 -90.775 D Ph(U) deg
74 1259.4 E Htot W
75 9.3663 F Edot W
76 9 DUCT Self Circulating Loop
77 Diameter for this ducts is set to be 1 cm (7.854E-5 m^2) so that it resists
78 the acoustic flow more than it does the steady flow. This should help with
79 the assumption of unidirectional flow because the smaller area here in the
80 SCL will limit the high amplitudes of oscillation.
81 6.5000E-4 a Area m^2 Mstr 1.0459E+5 A |p| Pa

```

Figure D.2: DELTAEC code used for simulations in Section 5.3, 1/3.

```

80 6.5000E-4 a Area m^2 Mstr 1.0459E+5 A |p| Pa
81 9.0378E-2 b Perim m 3a 178.07 B Ph(p) deg
82 1.0000 c Length m 7.5854E-3 C |U| m^3/s
83 5.0000E-4 d Srough 87.626 D Ph(U) deg
84 Master-Slave Links 1259.4 E Htot W
85 Optional Parameters -3.0465 F Edot W
86 Ideal Solid type
87 10 MINOR 2nd Connection Branch Flow Coefficient
88 Same 9a 6.5000E-4 a Area m^2 1.0480E+5 A |p| Pa
89 2.7475 b K+ -178.67 B Ph(p) deg
90 Same 10b 2.7475 c K- 7.5854E-3 C |U| m^3/s
91 87.626 D Ph(U) deg
92 1259.4 E Htot W
93 -25.677 F Edot W
94 11 SOFTEND
95 1.0480E+5 A |p| Pa
96 -178.67 B Ph(p) deg
97 7.5854E-3 C |U| m^3/s
98 P 87.626 D Ph(U) deg
99 1259.4 E Htot W
100 -25.677 F Edot W
101 Possible targets
102 -2.9463E-2 G Re(z)
103 0.45514 H Im(z)
104 298.00 I T K
105 -449.85 J p2ODE Pa
106 12 MINOR First Connection Trunk Coefficient - Median
107 Same 4a 1.2500E-3 a Area m^2 1.5605E+4 A |p| Pa
108 0.2424 b K+ -6.5005 B Ph(p) deg
109 Same 12b 0.2424 c K- 3.5651E-2 C |U| m^3/s
110 -89.62 D Ph(U) deg
111 -1168.3 E Htot W
112 33.325 F Edot W
113 13 DUCT Venturi Neck Continues
114 Same 4a 1.2500E-3 a Area m^2 Mstr 2.3435E+4 A |p| Pa
115 0.12533 b Perim m 13a -175.23 B Ph(p) deg
116 2.5000E-2 c Length m 3.5634E-2 C |U| m^3/s
117 5.0000E-4 d Srough -89.614 D Ph(U) deg
118 Master-Slave Links -1168.3 E Htot W
119 Optional Parameters 31.897 F Edot W
120 Ideal Solid type
121 14 CONE Change Me
122 Same 13a 1.2500E-3 a AreaI m^2 Mstr 1.0480E+5 A |p| Pa
123 0.12533 b PerimI m 14a -178.67 B Ph(p) deg
124 Same 3c 7.5000E-2 c Length m 3.4207E-2 C |U| m^3/s
125 Same 2a 2.5000E-3 d AreaF m^2 Mstr -89.626 D Ph(U) deg
126 0.17724 e PerimF m 14d -1168.3 E Htot W
127 5.0000E-4 f Srough 29.875 F Edot W
128 Master-Slave Links
129 Optional Parameters
130 Ideal Solid type
131 15 UNION Diverging T-Junction
132 Segments in the TBRANCH connects back to the resonator here. at the 0.6 m
133 length from the piston.
134 Two targets are added here so that the pressure amplitude and the phase
135 here is the same as the SOFTEND at the end of the SCL. This was, the
136 impedances and the flow rate into the SCL can stay as targets.
137 11 a Segnum 1.0480E+5 A |p| Pa
138 TargetSame 11A 1.0480E+5 b |p|Sfr Pa -178.67 B Ph(p) deg
139 TargetSame 11B -178.67 c Ph(p)S deg 2.6633E-2 C |U| m^3/s
140 TargetSame 11J -449.85 d p2ODES Pa -88.843 D Ph(U) deg
141 Possible targets 91.079 E Htot W
142 4.1979 F Edot W
143 298.00 G T K
144 -449.85 H p2ODEC Pa
145 16 MINOR 2nd Connection Trunk Flow Coefficient - Median
146 Same 17a 2.5000E-3 a Area m^2 1.0480E+5 A |p| Pa
147 6.1400E-2 b K+ -178.7 B Ph(p) deg
148 Same 16b 6.1400E-2 c K- 2.6633E-2 C |U| m^3/s
149 -88.843 D Ph(U) deg
150 91.079 E Htot W
151 3.4344 F Edot W
152 17 DUCT Duct in the rest of the resonator.
153 Same 2a 2.5000E-3 a Area m^2 Mstr 2.3450E+5 A |p| Pa
154 0.17724 b Perim m 17a -178.82 B Ph(p) deg
155 0.4000 c Length m 1.3241E-6 C |U| m^3/s
156 5.0000E-4 d Srough -133.82 D Ph(U) deg
157 Master-Slave Links 91.079 E Htot W
158 Optional Parameters 0.10978 F Edot W
159 Ideal Solid type
160 18 SURFACE For acoustic attenuation
161 Same 2a 2.5000E-3 a Area m^2 2.3450E+5 A |p| Pa

```

Figure D.3: DELTAEC code used for simulations in Section 5.3, 2/3.

```

159 18 SURFACE For acoustic attenuation
160 Same 2a 2.5000E-3 a Area m^2 2.3450E+5 A |p| Pa
161 -178.82 B Ph(p) deg
162 1.0956E-17 C |U| m^3/s
163 -132.58 D Ph(U) deg
164 91.079 E Htot W
165 ideal Solid type 8.8842E-13 F Edot W
166 19 HARDEND Change Me
167 Targ 0.0000 a R(1/z) 2.3450E+5 A |p| Pa
168 Targ 0.0000 b I(1/z) -178.82 B Ph(p) deg
169 1.0956E-17 C |U| m^3/s
170 -132.58 D Ph(U) deg
171 91.079 E Htot W
172 Possible targets 8.8842E-13 F Edot W
173 2.5449E-16 G R(1/z)
174 2.6576E-16 H I(1/z)
175 0.0000 I Ndot mol/s
176

```

Figure D.4: DELTAEC code used for simulations in Section 5.3, 3/3.

Bibliography

- [1] B. Higgins, “On the sound produced by a current of hydrogen gas passing through a tube,” *Journal of natural philosophy, chemistry and the arts*, vol. 1, no. 129-131, p. 2, 1802.
- [2] Y. Ueda, “Kibitsuno Rohre Entkama - Instrument used in historical Japanese shrine ritual,” 2nd International Workshop on Thermoacoustics, May 2014, Sendai, Japan.
- [3] C. Sondhauss, “Ueber die schallschwingungen der luft in erhitzten glasröhren und in gedeckten pfeifen von ungleicher weite,” *Annalen der Physik und Chemie*, vol. 155, no. 1, pp. 1–34, 1850. [Online]. Available: <https://doi.org/10.1002/andp.18501550102>
- [4] S. L. Garrett and S. Backhaus, “The power of sound,” *American Scientist*, vol. 88, no. 6, p. 516, 2000. [Online]. Available: <https://doi.org/10.1511/2000.6.516>
- [5] P. L. Rijke, “LXXI. notice of a new method of causing a vibration of the air contained in a tube open at both ends,” *The London, Edinburgh, and Dublin Philosophical Magazine and Journal of Science*, vol. 17, no. 116, pp. 419–422, Jun. 1859. [Online]. Available: <https://doi.org/10.1080/14786445908642701>
- [6] J. L. Rayleigh, “The explanation of certain acoustical phenomena,” *Nature*, vol. 18, no. 455, pp. 319–321, Jul. 1878. [Online]. Available: <https://doi.org/10.1038/018319a0>
- [7] S. L. Garrett, J. Adef, and T. Hoffer, “Thermoacoustic refrigeration for space applications,” in *Space Programs and Technologies Conference*. American Institute of Aeronautics and Astronautics, Mar. 1992. [Online]. Available: <https://doi.org/10.2514/6.1992-1712>

- [8] S. Backhaus and G. W. Swift, “A thermoacoustic-stirling heat engine: Detailed study,” *The Journal of the Acoustical Society of America*, vol. 107, no. 6, pp. 3148–3166, Jun. 2000. [Online]. Available: <https://doi.org/10.1121/1.429343>
- [9] C. J. Lawn and G. Penelet, “Common features in the thermoacoustics of flames and engines,” *International Journal of Spray and Combustion Dynamics*, vol. 10, no. 1, pp. 3–37, Dec. 2017. [Online]. Available: <https://doi.org/10.1177/1756827717743911>
- [10] N. Rott, “Damped and thermally driven acoustic oscillations in wide and narrow tubes,” *Zeitschrift für angewandte Mathematik und Physik ZAMP*, vol. 20, no. 2, pp. 230–243, Mar. 1969. [Online]. Available: <https://doi.org/10.1007/bf01595562>
- [11] J. P. Clark, W. C. Ward, and G. W. Swift, “Design environment for low-amplitude thermoacoustic energy conversion (DeltaEC),” *The Journal of the Acoustical Society of America*, vol. 122, no. 5, p. 3014, 2007. [Online]. Available: <https://doi.org/10.1121/1.2942768>
- [12] T. W. Steiner and M. Elferink, “Thermoacoustic waste heat recovery engine. comparison of simulation and experiment,” *The Journal of the Acoustical Society of America*, vol. 144, no. 3, pp. 1712–1712, Sep. 2018. [Online]. Available: <https://doi.org/10.1121/1.5067594>
- [13] L. Rayleigh, “XXXIV. On the pressure of vibrations,” *The London, Edinburgh, and Dublin Philosophical Magazine and Journal of Science*, vol. 3, no. 15, pp. 338–346, Mar. 1902. [Online]. Available: <https://doi.org/10.1080/14786440209462769>
- [14] G. W. Swift, *Thermoacoustics - A Unifying Perspective for Some Engines and Refrigerators*, 2nd ed. Springer International Publishing, 2017. [Online]. Available: <https://doi.org/10.1007/978-3-319-66933-5>
- [15] B. L. Smith and G. W. Swift, “Measuring second-order time-average pressure,” *The Journal of the Acoustical Society of America*, vol. 110, no. 2, pp. 717–723, Aug. 2001. [Online]. Available: <https://doi.org/10.1121/1.1382615>
- [16] H. Struchtrup, *Thermodynamics and Energy Conversion*. Springer Berlin Heidelberg, 2014, ch. 14, pp. 327–329. [Online]. Available: <https://doi.org/10.1007/978-3-662-43715-5>

- [17] J. T. Karlsen, P. Augustsson, and H. Bruus, “Acoustic force density acting on inhomogeneous fluids in acoustic fields,” *Physical Review Letters*, vol. 117, no. 11, Sep. 2016. [Online]. Available: <https://doi.org/10.1103/physrevlett.117.114504>
- [18] J. P. Koulakis, S. Pree, A. L. F. Thornton, A. S. Nguyen, and S. Putterman, “Pycnoclinic acoustic force,” in *21st International Symposium on Nonlinear Acoustics*. Acoustical Society of America, 2018. [Online]. Available: <https://doi.org/10.1121/2.0000848>
- [19] B. Ward, J. Clark, and G. Swift, *DeltaEC Users Guide*, version 6.4b2.9 ed. Los Alamos National Laboratory, Apr. 2020, ch. 14, pp. 266–268, second-order time-averaged pressure.
- [20] R. S. Reid, W. C. Ward, and G. W. Swift, “Cyclic thermodynamics with open flow,” *Physical Review Letters*, vol. 80, no. 21, pp. 4617–4620, May 1998. [Online]. Available: <https://doi.org/10.1103/physrevlett.80.4617>
- [21] D. Gedeon, “DC gas flows in stirling and pulse tube cryocoolers,” in *Cryocoolers 9*. Springer US, 1997, pp. 385–392. [Online]. Available: https://doi.org/10.1007/978-1-4615-5869-9_45
- [22] M. P. Mitchell, “Pulse tube refrigerator,” American Patent 5,966,942, October 19, 1999, continuation in part 6,109,041, August 29, 2000.
- [23] N. Tesla, “Valvular conduit,” American Patent 1,329,559, February 3, 1920.
- [24] G. W. Swift and S. Backhaus, “A resonant, self-pumped, circulating thermoacoustic heat exchanger,” *The Journal of the Acoustical Society of America*, vol. 116, no. 5, pp. 2923–2938, Nov. 2004. [Online]. Available: <https://doi.org/10.1121/1.1804634>
- [25] S. L. Garrett, *Understanding Acoustics*, 2nd ed. Springer International Publishing, 2017. [Online]. Available: <https://doi.org/10.1007/978-3-319-49978-9>
- [26] I. E. Idelchik, *Handbook of Hydraulic Resistance*, 4th ed. Begell House Publishers Inc., U.S., Jul 2007, ISBN 978-1-56700-251-5.
- [27] D. C. Rennels and H. M. Hudson, *Pipe Flow*. John Wiley & Sons, Inc., May 2012, pp. 177–199. [Online]. Available: <https://doi.org/10.1002/9781118275276>

- [28] Y. Ueda, S. Yonemitsu, K. Ohashi, and T. Okamoto, “Measurement and empirical evaluation of acoustic loss in tube with abrupt area change,” *The Journal of the Acoustical Society of America*, vol. 147, no. 1, pp. 364–370, Jan. 2020. [Online]. Available: <https://doi.org/10.1121/10.0000597>
- [29] W. P. Arnott, H. E. Bass, and R. Raspet, “General formulation of thermoacoustics for stacks having arbitrarily shaped pore cross sections,” *The Journal of the Acoustical Society of America*, vol. 90, no. 6, pp. 3228–3237, Dec. 1991. [Online]. Available: <https://doi.org/10.1121/1.401432>
- [30] J. P. Stark, “Fundamentals of classical thermodynamics (van wylen, gordon j.; sonntag, richard e.),” *Journal of Chemical Education*, vol. 43, no. 5, p. A472, May 1966. [Online]. Available: <https://doi.org/10.1021/ed043pa472.1>
- [31] F. M. White, *Fluid Mechanics*, 7th ed. New York, NY: McGraw-Hill, 2009, ch. 6, p. 370, ISBN: 978-0-07-352934-9.
- [32] M. Hino, M. Sawamoto, and S. Takasu, “Experiments on transition to turbulence in an oscillatory pipe flow,” *Journal of Fluid Mechanics*, vol. 75, no. 2, pp. 193–207, May 1976. [Online]. Available: <https://doi.org/10.1017/s0022112076000177>
- [33] M. IGUCHI, M. OHMI, and K. MAEGAWA, “Analysis of free oscillating flow in a u-shaped tube,” *Bulletin of JSME*, vol. 25, no. 207, pp. 1398–1405, 1982. [Online]. Available: <https://doi.org/10.1299/jsme1958.25.1398>